Self-Assembled Nanotube/Nanoparticle Biosensors

A DISSERTATION

SUBMITTED TO THE FACULTY OF THE GRADUATE SCHOOL

OF THE UNIVERSITY OF MINNESOTA

BY

Dongjin Lee

IN PARTIAL FULFILLMENT OF THE REQUIREMENTS

FOR THE DEGREE OF

DOCTOR OF PHILOSOPHY

Tianhong Cui, Advisor

Mrinal Bhattacharya, Co-advisor

May 2010

Acknowledgements

I would like to express my sincere gratitude to my advisor, Professor Tianhong Cui for his guidance and support during my Ph.D. study. The completion of my Ph.D. could not been achieved without his continuous encouragement and advice. I also thank my co-advisor, Professor Mrinal Bhattacharya for his continued guidance and support throughout my study.

I thank the Professors of the committee, Professor Arthur G. Erdman, Professor Steven J. Koester, and Professor Steven A. Campbell for their guidance and discussions. Their sincere interest and constructive questions are truly acknowledged. I could not finish my thesis without expressing my gratitude to my collaborators, Professor Sagar M. Goyal, Professor David Lilja, Professor Andy Taten, Dr. Yogesh Chander, Dr. Chia-Lang Chen, Mr. Min-Woo Jang, Mr. Walter Partlo, and Ms. Shruti Patil.

I also would like to thank all my colleagues of the Technology Integration and Advanced Nano/micro Systems Laboratory for the assistance and all the moment we shared. Dr. Wei Xue and Dr. Miao Lu are truely acknowledged for the wonderful discussions and collaborative work. I also thank the undergraduate students I mentored, Ms. Chelsea Stinson, Ms. Janet Ondrake, and Mr. Brendan Pankratz.

This work partially supporeted by the DARPA M/NEMS Science and Technology Fundamental Research through the Micro/Nano Fluidic Fundamental Focus (MF3) Center. I also would like to thank the staff at the Nanofabrication Center and IT Characterization Facility for a great deal of helpful discussions on experimental schemes and data analysis.

Many thanks go to countless people who have helped and supported myself but remain nameless due to my inability to remember at this moment.

Finally, my deepest appreciation goes to my parents and brothers. It would be all a castle in the air without their support and endless love.

Abstract

The self-assembled carbon nanotube (CNT) and indium oxide nanoparticle (INP) multilayers are presented for the applications to electrochemical pH and biological sensing. The excellent electrochemical properties of the nanomaterial thin film made of layer-by-layer self assembly is exploited to design and fabricate sensors targeted for a facile and low-cost application.

The pH-sensitive conductance of the self-assembled CNT/INP chemoresistor and ion-sensitive field-effect transistor (ISFET) is studied, and its shift mechanisms are elucidated. There are two primary factors influencing the conductance of the semiconducting nanomaterial thin film: the direct protonation/deprotonation and the proximal ion effect. The CNT chemoresistor experiences the conductance change due to the molecular protonation/deprotonation of carboxylic groups. The effect of proximal ions demonstrates conventional semiconductor theory, where the pH increase corresponds to negative shift in gate voltage resulting in a higher conductance in p-type CNTs. The additional silica nanoparticle (SNP) layer adjusts the pH-sensitive conductance behavior, particularly from nonlinear to linear response, which is beneficial to the implementation of pH sensors. Indeed, the electrochemical properties of nanomaterial thin film are tunable by exploiting a different type of the nanomaterial, surface chemistry, and structure.

Glucose biosensors and immunosensors are designed and implemented based on the conductance shift mechanisms explored. The sensitivity of CNT chemoresistor and ISFET glucose sensors is 10.8 and 18-45 μA/mM, respectively, on a linear range of 0-10 mM with a response time of a few minutes. An INP chemoresistor sensor array is designed to address variant electrical properties of the nanomaterial films, allowing the statistical analysis of data with one-shot of sample delivery. The INP immunoglobulin G (IgG) ISFET sensor exhibits a resolution of 40 pg/ml, and the CNT conductometric

H1N1 swine influenza virus (SIV) sensor demonstrates a detection limit of 180 viruses $TCID_{50}$/ml with a specificity to non-SIVs.

The nanomaterial thin film electrochemical transducers are proven to be a potent candidate for the next-generation of the chemical and biological sensors possessing a high sensitivity and resolution. Due to a facile implementation and operation, nanomaterial biosensors could be used for domestic and clinical diagnosis, point-of-care detection, and a sensing component in lab-on-a-chip systems.

Table of Contents

List of Tables

List of Figures

1. Introduction

1.1. Background

Nobel Laureate Richard Feynmann suggested his distinguished technological vision entitled as “There’s plenty of room at the bottom” at the annual meeting of the American Physical Society in 1959. He described the nanoscale fabrication process by which the individual atoms or molecules are independently manipulated, controlled, and assembled together. Feynmann’s talk has been a corner stone in nanoscience and nanotechnology. Nanotechnology is referred to as any technology that is performed on a nanoscale (10^{-9} of a meter) and has applications in the real world. It includes the synthesis and application of chemical, physical and biological systems on a scale ranging from individual atom or molecules to sub-micrometer. It also covers the integration of nanostructures into larger scale, where nanostructures function effectively and provide hosting materials and structures with remarkable performance enhancements. The discovery of novel materials and phenomena at the atomic scale as well as processes to assemble them together provide great opportunities for the development of innovative micro/nanosystems, which have various applications. These powerful and potential applications of nanotechnology promise breakthrough in such areas as materials and manufacturing, micro/nanoelectronics, medicine and healthcare, energy, biotechnology, information technology, and security.

The biosensor technology evolves synergistically with the advent of nanomaterials possessing novel properties such as mechanical stiffness and strength [1], electrical [2] and thermal conductivity [3], photoemission [4], electromechanical [5] and electrochemical transduction [6], and catalytic activity [7]. Nanomaterial based biosensors have garnered much attention since they can be miniaturized in conjunction with microfabrication techniques to attain low cost, low power consumption, possible implantation, and distributed sensing system. Leaving such general advantages from the miniaturization aside, first of all, nanomaterials have the size similarity to bioentities such

as proteins and DNA molecules, which facilitates the charge transfer between transducing nanomaterials and bioreceptors resulting in a high sensitivity and resolution. The ability of nanotechnology to tailor the size, structure, composition and surface chemistry yields the engineered nanomaterials sensing platform with a high performance [6]. Furthermore, they demonstrated a wide range of sensing mechanisms such as nanomechanical resonator [8], fluorescence [9], electrochemical [10-13], optical [14] and magnetic detection [15]. Finally, they could provide a variety of bioassay platforms to determine the analyte present in a sample. For these reasons, nanomaterials are one of promising candidates to develop novel biosensors.

Most biological processes are based on the electrostatic interactions and charge transfers such as the citric acid cycle due to enzymatic reactions [16]. Consequently, the charges can be readily intercepted by or transferred to the nanoscale materials due to the enhanced interaction, which is detected by the external electric circuitry. Therefore, electrochemical sensors are advantageous for biosensing applications by means of nanomaterials. Furthermore, the study of electrochemical properties of nanomaterials is actively ongoing [11, 17, 18]. In addition, nanomaterials provide electrochemical sensors with a delicate path to design new structures of novel material with engineered compositions and to interface biological recognition events with electronic signal transduction through nanomaterials [6].

1.2. Carbon nanotube

As one of most prominent discoveries in 21st century, the carbon nanotube (CNT) has been extensively studied and used as a technological breakthrough for novel applications in near future. Since the first discovery of multi-walled CNT (MWCNT) by Iijima in 1991 [19] followed by single-walled CNT (SWCNT) in 1993 [20], CNTs have been being spotlighted for the last two decades in research and industrial sectors due to the excellent mechanical [21-28], unique electrical [2, 29] and thermal [3, 30], and extraordinary optical properties [31]. The combination of these endowed properties with

the low density triggered research on CNT-polymer composites toward structural reinforcement, electrical [32] and thermal conductivity enhancement [33, 34], and optical property adjustment [35]. Even though there has been an experimental variety particularly in the characterization method, both theoretical predictions [36, 37] and experimental observations revealed that the CNT is one of stiffest and strongest materials known with a modulus of more than 1 TPa and tensile strength of up to 150 GPa. Consequently, much research effort has been made to explore CNTs as a next-generation composite material. CNT-reinforced materials ultimately provide a new class of revolutionary strong and lightweight properties suitable for applications in aerospace, defense, nanoelectronics, energy, and photonics.

In order to manufacture CNT-polymer composites, solvent casting, melt blending, and in-situ polymerization have been widely used, depending on the incorporation method of CNTs into host polymer matrix. In solvent casting, CNTs are dispersed into water or organic solvents in which polymers are dissolved. The composite film is obtained after evaporation of solvents by casting or spin-coating. Polyvinyl alcohol [38, 39], polystyrene [40], and epoxy [41-44] composites were fabricated using this method. It is easy to prepare homogeneous thin films, but most solvents used were organic liquids of high toxicity. Furthermore, the stable dispersion of CNTs into such solvents should be addressed. In melt blending, polymers are heated to provide the pristine polymer with viscosity, and CNTs are mixed with substantial shear force, followed by extrusion or injection molding of the mixture. Polystyrene [45, 46], polymethylmethacrylate (PMMA) [47-49], polycarbonate [50], and polyurethane [51] composites were prepared using this method. It is advantageous that this method enables a high loading of CNTs, and high intrinsic viscosity makes increasing shear to aggregates and minimizes reaggregation. However, it is offset by the need of bench-top equipment to make composites at the elevated temperature and the limitation to thermoplastic polymers. Another method is to use a monomer as a starting material and carry out *in-situ* polymerization. Since Cochet *et al*. [52] used this method to prepare a MWCNT-polyaniline composite, a number of

CNT-polymer composites have been prepared including MWCNT-polystyrene [53], SWCNT-polyimide [28], and MWCNT-polypyrrole [54]. However, a main hurdle of this method is poor dispersion of CNTs into the polymer matrix. Furthermore, load transfer from the polymer matrix to the CNT filler does not take place effectively.

As an alternative, a highly organized and easily tunable CNT-polymer composite can be prepared by molecular layer-by-layer (LbL) assembly. This process has been used to manufacture functional thin film [55-57] with controlled internal structures without any segregation. A multilayer of SWCNT-polyethyleneimine was reported to have an elastic modulus of 35 GPa and tensile strength of up to 325 MPa [55] using tensile test. LbL assembly of CNTs becomes more advantageous, because CNTs are considered off-the-shelf low cost building blocks due to today's large-scale production of CNTs.

CNTs have a great potential application to nanoelectronics due to their unique dimensions as well as unusual current conduction mechanism. Due to the dual electronic properties, semiconducting or metallic relying on its chirality and diameter [58], CNTs are specifically applicable to nanoelectronic devices, where semiconducting and metallic CNTs play roles of channel material and conductive interconnect, respectively [59]. As an advantage of using CNT as a semiconducting material in field effect transistors (FET), CNT revealed higher charge carrier mobility than silicon based devices [2]. For this reason, CNTs have become candidatefor next-generation materials in nanoelectronics.

Martel *et al.* [60] showed the possibilities of application of CNTs to the FETs. The intrinsic mobility of an individual semiconducting SWCNT is more than 100,000 cm^2/Vs, which is much higher than any other semiconductor materials [61]. Compared to conventional FETs based on silicon with an electron mobility of 400-1000 cm^2/Vs, the individual CNT-FETs have higher mobility of around 3,000 cm^2/Vs [29, 62]. CNT thin film transistors (TFTs) were built in the aligned fashion *in-situ* vertical growth on the oxide layer [63] and randomly distributed [64]. CNT-TFTs have higher manufacturability than individual CNT-FETs, though mobility is lower. Furthermore, the reliability of CNT TFT is relatively high due to interconnections of CNTs. Spinning [65] and spray [66]

were used to coat the SWCNT on the substrate and the reported mobility range was 1-150 cm^2/Vs. Recently, Xue *et al.* reported LbL assembled multilayer of (PDDA/SWCNT) FETs, whose mobility was as high as 333 cm^2/Vs [56].

Ultimately, in order to exploit these endowed properties, CNTs need to be integrated into existing devices or matrix materials to be utilized as active components. However, the handling and manipulation of individual CNTs are extremely difficult due to their tiny size, which makes it very challenging to attain mass production. Nonetheless, much effort have been made to incorporate of CNTs into electronic devices [60] and electromechanical systems [1] as a basic building block. Layer-by-layer (LbL) assembly has been used to manufacture ultra-thin film functional materials with the controlled internal structure of CNTs [67, 68], nanoparticles [69], and even biomolecules [70]. Since the pioneering research on LbL assembly of CNTs [67], much effort has been made to exploit the versatility of the LbL assembled CNTs multilayers, particularly as sensors [11, 68, 71, 72] and actuators [73]. Moreover, LbL assembly of CNTs has been coming into the spotlight as an alternative method to integrate CNT into devices or versatile functional materials without any segregation [74]. In conjunction with the mechanical property, CNTs have been used as building blocks in the nanoelectromechanical switch and detector for nanoscale motion [75].

Compared to mechanical and electrical properties of CNTs, electrochemical properties have not been studied well. However, CNTs are known to have a high elecrocatalytic effect and a fast electron-transfer rate [76]. Rather than an excellent enzymatic immobilization site, CNTs are used for various electrochemical applications due to the excellent electrical and electrochemical properties. For this reason, CNTs have become one of the promising functional materials for applications to chemical [77] and biological sensors [78] for the enhancement in selectivity and sensitivity. The studies of the electrochemical properties of CNTs substantially make them very useful for bio-sensing applications [79]. The reported CNT based biosensors detected protein [80], DNA [81], immunoglobulin [82], neurotransmitters [83] and other molecules [84] for the purpose of

diagnostics in the presence or absence of bio-receptors, reacting specifically with target biomolecules.

1.3. Nanoparticles

Nanoparticles (NPs) possess unique physical and chemical properties that are much different from bulk materials presumably due to quantum confinement effect [85]. NPs are used to develop novel sensing devices particularly electrochemical biosensors. Currently, a variety of size and material composition are available in order to design novel devices. For example, metal NPs have high conductivity and catalytic properties suitable for conductive wire, whereas semiconducting nanoparticles are used for labels or tracers for electrochemical analysis. Dielectric silica nanoparticles are often used as biomolecular immobilization sites due to the biocompatibility. Although, the role of nanoparitcles in developed electrochemical sensors are different, but they can be categorized into [85]: (a) biomolecule immobilization sites, (b) catalyst for electrochemical reactions, (c) electron transfer enhancement like molecular wires, (d) biomolecules labeling, or (e) reactant.

1.4. Enzyme kinetics

Enzymes are specialized proteins that catalyze biochemical reactions. Enzymes bind to certain molecules called substrates, reduce activation energy, and facilitate the convertion of substrate into products. Enzymes are extremely selective in the sense that they recognize exact three dimensional structures of substrates and only catalyze specific reactions. There are several factors affecting enzyme activity. Enzyme activity is highly dependent on temperature and pH, which cause changes in the protein structure. Some molecules such as inhibitors or activators may interact with enzymes to decrease or increase their activities, respectively. Enzyme activity is also affected by the substrate concentration. Although Michaelis-Menten kinetics only works when the concentration of enzyme is less than that of substrates, it is a useful model to understand enzymes behaviors.

$$E + S \underset{k_{-1}}{\overset{k_1}{\rightleftarrows}} ES \xrightarrow{k_2} E + P$$

where E is the enzyme, S is the substrate, P is the product, and ES is enzyme-substrate complex. By use of the steady-state approximation on the [ES], the concentration of the intermediates is assumed to equilibrate much faster than those of the product and substrate:

$$[ES] = \frac{k_1[E][S]}{k_{-1} + k_2}$$

The Michaelis-Menten constant is defined as follows:

$$K_M = \frac{k_{-1} + k_2}{k_1}$$

The rate of products is

$$\frac{d[P]}{dt} = k_2[E_0]\frac{[S]}{K_M + [S]} = V_{\max}\frac{[S]}{K_M + [S]}.$$

V_{max} is the maximum velocity at which the reaction becomes saturated and K_M is the substrate concentration when the reaction reaches at half of V_{max}. Since the plot of V versus [S] is nonlinear, Lineweaver-Burke plot or double reciprocal plot between the rate of product and the concentration of the substrate is commonly used instead.

Biosensors are highly dependent on enzyme activity. Especially, since immobilized enzymes show a different activity from free ones, enzyme kinetics can be considered as an important factor for evaluating enzymatic biosensors. Electrochemical version of Michaelis-Menten kinetics is used for evaluating enzymatic biosensors in this study as follows:

$$\frac{1}{i_{ss}} = \frac{K_M^{app}}{i_{\max}}\frac{1}{[S]} + \frac{1}{i_{\max}}$$

where i_{ss} is the steady-state current at the specific substrate concentration, K_M^{app} is the apparent Michaelis-Menten constant, and i_{max} is the maximum current that corresponds to the reaction rate.

1.5. Thesis overview

The nanomaterial device technology used in this study is introduced in Chapter 2 as a combination method of top-down microfabrication and bottom-up self-assembly. The material preparation, characterization, and fabrication of nanomaterial devices will be discussed extensively. Chapter 3 is intended to provide the fundamental mechanisms of pH sensing in SWCNT and INP devices. The hypothetical model to explain the sensing mechanism of (PDDA/SWCNT) multilayer will be substantiated by employing PMMA as an ion passivation layer and weak polyelectrolytes as a paring species instead of PDDA in layer-by-layer assembly. Furthermore, the role of the SNP layer on top of the SWCNT and INP devices will be discussed. Based on the pH sensing mechanisms found in Chapter 3, the variety of glucose sensors and immunosensors with a different nanomaterial and structure are presented in Chapter 4 and 5, respectively. In Chapter 4, the conductometric SWCNTs glucose sensors on the silicon substrate will be presented. The SWCNT ISFET sensors have been constructed on a flexible and transparent PET substrate pH/glucoses sensing. In addition, INP/SNP sensor arrays are demonstrated as a glucose sensor to address the variant electrical properties of nanomaterial devices. The glucose sensor performance in terms of the sensitivity and apparent Michaelis-Menton constant are summarized and discussed. Immunoglobulin G (IgG) sensors are demonstrated, in Chapter 5, using an INP/SNP dual structure to demonstrate the applicability of an all-nanoaparticle film as a bioassay platform possessing a facile electronic detection scheme using excellent electrochemical properties. In addition, H1N1 swine influenza virus sensors will be introducted using SWCNTs to shed light on the pathogen detection with label-free scheme. Finally, in Chapter 6, the conclusions are extracted from the series of nanomaterial pH, glucose, and immunosensors developed.

Future works will be suggested for the further development of nanomaterial-based biosensors.

2. Fabrication of nanomaterial devices

This chapter explores nanomaterial device technology commonly used throughout the study in terms of methods and materials. It covers the detailed experimental results as well as the general aspects of the bottom-up layer-by-layer (LbL) self-assembly for the formation of nanomaterial thin films and top-down microfabrication for the patterning of such films and fabrication of platform on which nanomaterials are placed. The method is based on the combinative method of top-down microfabrication and bottom-up self-assembly. The materials are assembled onto the substrate to fully take advantage of their excellent properties over the large area targeted for low-cost manufacturing.

The major challenge of using nanotmaterials for the device applications is the manufacturability with reasonable throughput. Even though it is well-known that individual nanotubes and nanoparticles have the excellent properties, the manipulation and handling of individual nanomaterials are extremely difficult. Furthermore, the *in-situ* growth of nanomaterial onto the existing matrix structure is offset by harsh environments and a long process time. Instead of using individual nanomaterials, the nanomaterial thin is fabricated using LbL assembly. Aside from the general advantages of LbL assembly, the excellent properties of nanomaterials are retained [56].

The materials used are single-walled carbon nanotubes (SWCNTs), indium oxide (In_2O_3) nanoparticles (INPs), silica (SiO_2) nanoparticles (SNPs) and polyelectrolytes (PEs) to constitue sensing elements and structures for biosensors. The other materials used less frequently are discussed in the corresponding chapter or sections. Using CNTs and NPs commercially available as the off-the-shelf raw materials, nanomaterial devices are fabricated using the solution-based LbL self-assembly to study electrochemical properties of nanomaterial multilayers.

2.1. Fabrication methods

The fabrication techniques used in this study include top-down microfabrication and bottom-up LbL nano self-assembly, which has been well developed so far for the fabrication of the nanomaterial devices [86, 87]. In the top-down approach, platforms such as metal electrodes and protective layers are fabricated by removing the unwanted part from the bulk material. In the bottom-up approach, on the other hand, nanomaterials such as CNTs and NPs are assembled onto the substrate to construct mutilayered thin films and to be patterned in the end as a functional structure.

The bottom-up approach to produce thin films of a variety of materials includes: Lanmuir-Blodgett (LB) films, self-assembled monolayer (SAMs), and layer-by-layer (LbL) assembly. The LB film is one or more layers of organic materials that can be prepared by dipping a flat solid substrate into a solution containing an amphiphilic species. The SAM is a monolayer of alkane with a specific functional group on the surface. The monomer is oriented at a specific angle with surface normal. The LbL assembly is the alternative deposition of monomer solution, which fabricates the multilayer using electrostatic, van der waals force, and hydrophobic interactions. The LbL assembly has attracted great attention since Decher and co-worker showed the oppositely charged polyelectrolyte multilayer film that was made with molecular-level thickness controllability [88-90]. Furthermore, the film prepared by LbL is thermodynamically stable, versatile, simple, low-cost, and defect-free [91]. Since then, the LbL assembly has extended to many other materials: biomolecules such as proteins and deoxyribonucleic acids (DNAs) [92], nanoparticles [93], and carbon nanotubes [94].

LbL assembly is based on alternative dipping into oppositely charged ionic solutions with intermediate washing and drying, as shown in Figure 2-1. Polyions are adsorbed onto the substrate to make the surface oppositely charged for the subsequent adsorption of polyions. The multilayer film can be fabricated by sequential and repetitive dipping into polycationic and polyanionic solutions, as shown in Figure 2-1 (a). The negatively charged substrate, in general, is immersed into a polycationic solution, followed by the

rinsing with deioninzed water (DIH_2O) and drying with nitrogen (N_2) stream. The surface becomes positively charged and attracts anionic ions in next step, so that the anionic species is assembled onto the polycation-covered surface. This process is repeated to build up the multilayers. The side view of substrate and the detailed film hierarchy of polyions, biomolecules, and nanomaterials are illustrated in Figure 2-1 (b).

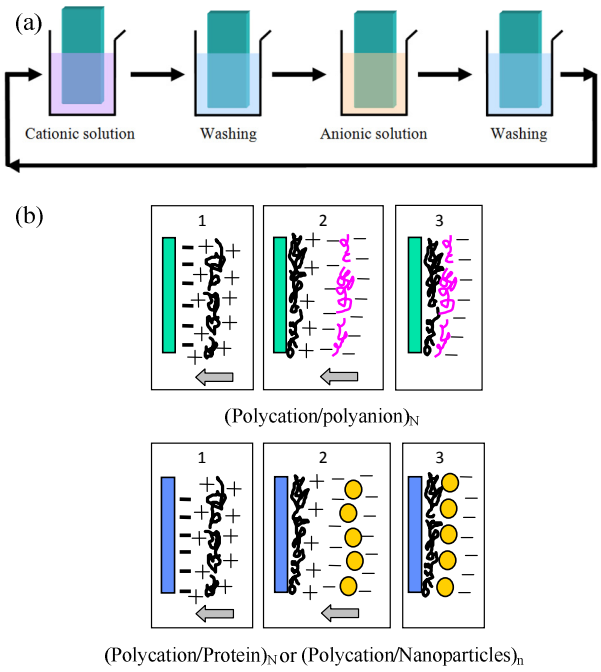

Figure 2-1 The scheme of layer-by-layer self-assembly: (a) alternative dipping into oppositely charged solution with the intermediate washing and drying, (b) adsorption of macromolecules by layer-by-layer self-assembly of polyelectrolytes, protein, and nanomaterials

The LbL assembly can introduce novel nanomaterials such as nanotubes, nanoparticles, nanowires, and nanotemplates onto the existing materials or devices that have been using in the conventional microfabrication technique. The novel properties of nanomaterials can be exploited with the aid of microfabricated platforms. In general, the LbL self-assembly has many advantages as follows:

- Tunable material properties
- Organized nanocomposite materials targeted for new mechanical, electrical, optical, and catalytic properties

- Lager surface-to-volume ratio suitable for high-performance sensors
- Biocompatibility and incorporation of biomacromolecules
- Unlimited coating cycles and molecular scale thickness controllability
- Unlimited substrates (silicon wafers, plastics, glass, etc)
- Mild fabrication conditions: atmospheric process and room temperature
- Contamination-free due to solution-based process
- Simplicity and versatility
- Low cost

Most microfabrication techniques descended from the conventional solid-state integrated circuit (IC) fabrication, which are well developed and take advantage of the existing facilities. Typical top-down microfabrication processes are schematized in Figure 2-2, where the repetitive work of deposition of the desired material, pattern transfer, and removal of unwanted materials are conducted to construct the desired structures.

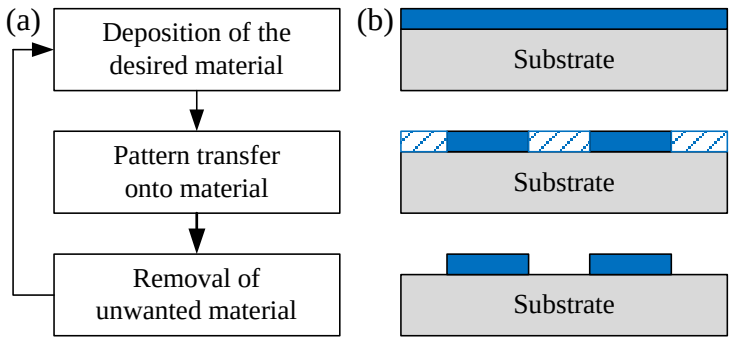

Figure 2-2 Top-down microfabrication scheme: (a) flowchart for microfabrication and (b) a cross sectional view of device

A core of microfabrication process is the pattern transfer. The most widely used photolithographic techniques are schematized in Figure 2-3. A photoresist (PR), which is a photo-sensitive polymer, is applied onto the well cleaned silicon wafer substrate on which desired material is deposited. The photomask is transferred to PR using UV lithography. The exposed region experiences structural changes, fragmentation of

polymer chains in case of positive PR and crosslink in case of negative PR. During develop, the exposed positive PR is removed, whereas crosslinked negative PR is left. Using PR pattern, unwanted materials are removed. Finally, the PR is removed using its own strippers or organic solvents for the patterning of the next materials. If a negative PR is used, the exact opposite image is obtained. Repetitive and sequential deposition, exposure, and etching produce most IC and MEMS devices. The removal of unwanted materials, in general, is accomplished by two different techniques, etching and lift-off, depending on the order of photoresist (PR) application and the desired material. In etching, as shown in Figure 2-3 (a), the desired material is deposited first, followed by the application of PR for the patterning by photolithography. With the aid of patterned PR as a masking layer, the pattern is finally transferred by etching unwanted material. In lift-off, on the contrary, PR is applied first and the pattern is transferred onto PR layer as shown in in Figure 2-3 (b). Then, the desired material is deposited and the patterned PR is finally removed along with the materials on top of it.

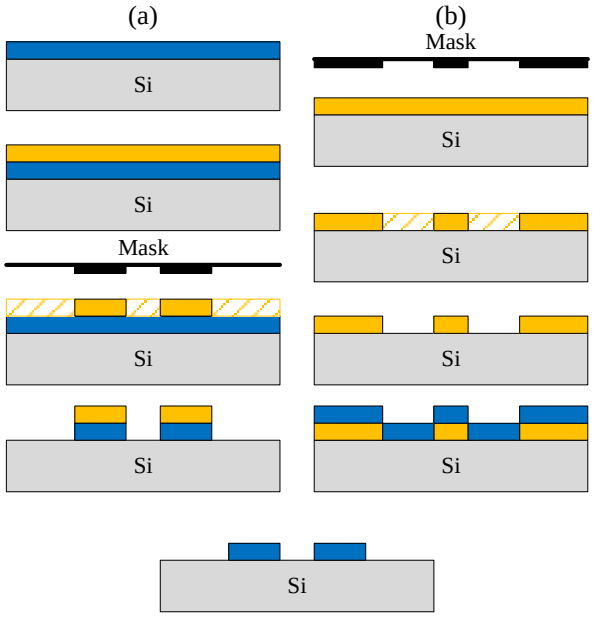

Figure 2-3 Schematic of pattern transfer techniques: (a) etching and (b) lift-off

The deposition of the desired material, which is usually achieved by evaporation, sputtering, or chemical vapor deposition in convential microfabrication, is substituted by the aforementioned LbL nano self-assembly of nanomaterials in this study. Then, either etching or lift-off technologies is used to pattern the nanomaterial multilayer. The conventional metal deposition was conducted on the LbL assembled thin film [86]. The aluminum layer was deposited using evaporation on top of the LbL assembled nanoparticle thin film. After patterning the aluminum layer, the exposed LbL nanoparticle thin film was etched out using oxygen (O_2) plasma. For lift-off, a sacrificial layer of photoresist is applied onto the silicon wafer, followed by the pattern transfer using lithography. The LbL assembly is conducted on the patterned PR, followed by lift-off. The micropatterned SWCNT LbL film was reported using lithography and lift-off process [87]. The lateral dimension is controlled by the lithographic technique, while the vertical dimension of the CNT film was determined by the LbL technique as described.

Both ‘lift-off’ and ‘metal-mask-etching’ techniques are proven to be effective for the selective deposition of nanomaterials on the substrate. These combinative processes are simple, versatile, and highly reproducible. Based on these techniques, a number of devices were fabricated including metal-oxide-semiconductor (MOS) capacitors [95], field-effect transistors (FETs) [96], thin film cantilevers [54, 87], and biosensors [12, 13, 68, 97]. A broad range of materials was used for functional devices including polyelectrolyte, biomolecules such as enzyme and antibody, nanoparticles, nanotube, and clay platelets. These results showed the combinatory fabrication of devices and technological breakthrough by which the novel properties of nanomaterials can be fully exploited. The choice of nano building blocks for LbL assembly along with their functionalization for the charge enhancement may create an innovative device in many areas.

2.2. Materials

2.2.1. Single-walled carbon nanotube

SWCNTs used in this study were from Chengdu Organic Chemicals Co Ltd (purity: > 90 %, diameter: 1-2 nm, length: ~50 μm, SSA: > 407 m^2/g) and Nanostructured and Amorphous Materials, Inc (purity: 90% of SWCNTs and 95% of CNTs, diameter: 1-2 nm, length: 5-30 μm, SSA: 300-380 m^2/g) commonly possessing the diameter of 1-2 nm, length of tens of μm, and purity of 90 %. However, pristine CNTs (p-CNTs) are generally inappropriate for solution-based self-assembly process due to the poor solubility to water caused by the hydrophobic nature of the carbon surface. Hence, the functionalization of SWCNTs was performed as follows. 0.5 g of SWCNTs were chemically functionalized in 3:1 mixture of concentrated sulfuric (150 mL, H_2SO_4) and nitric acid (50 mL, HNO_3) at 110 °C for an hour, followed by 5-fold dilution into water and the vacuum filtering with the pore size of 0.22 μm to remove soot, metallic particles, and shorter SWCNTs. After the rinsing with deionized water (DIH_2O) several times until pH approached 5, the functionalized SWCNTs (f-SWCNTs) were harvested and dispersed into 500 mL of fresh DIH_2O with the aid of ultra-sonication for an hour. Subsequently, the SWCNT solution was centrifugated at a speed of 5000 rpm (4500 g, Eppendorf centrifuge 5804) for 20 minutes to eliminate longer SWCNTs, big aggregates and bundles. In the end, the supernatant was carefully decanted and the precipitates were discarded. As a result, f-SWCNTs were well dispersed in water and had great stability due to the induced hydrophilic functional groups on the surface of SWCNTs. In order to determine the final concentration, 500 μL of SWCNT solution was drop-cast onto a glass slide, and weight change was measured using an analytical balance (Satorius AG) after evaporation. The final concentration of SWCNT solution was about 0.6 mg/ml (0.06 wt%).

Reflective Fourier transform infrared spectroscopy (FTIR, Nicolet Magna IR 750) was used to characterize the functional groups after the acidic functionalization. First, a

piece of silicon (Si) wafer with a 2 μm thick thermally grown silicon dioxide (SiO_2) layer was cleaned in a piranha solution (3:1 H_2SO_4:H_2O_2) at 120 ºC for 15 minutes, and rinsed with a copious amount of DIH_2O. The f-SWCNTs aqueous solution was drop-cast onto the cleaned Si/SiO_2 surface. With the background of Si/SiO_2 surface, the spectra were obtained as the absorbance in the mid-infrared (MIR) region, 4000-400 cm^{-1} by averaging 1000 scans with a spectral resolution of 2 cm^{-1}.

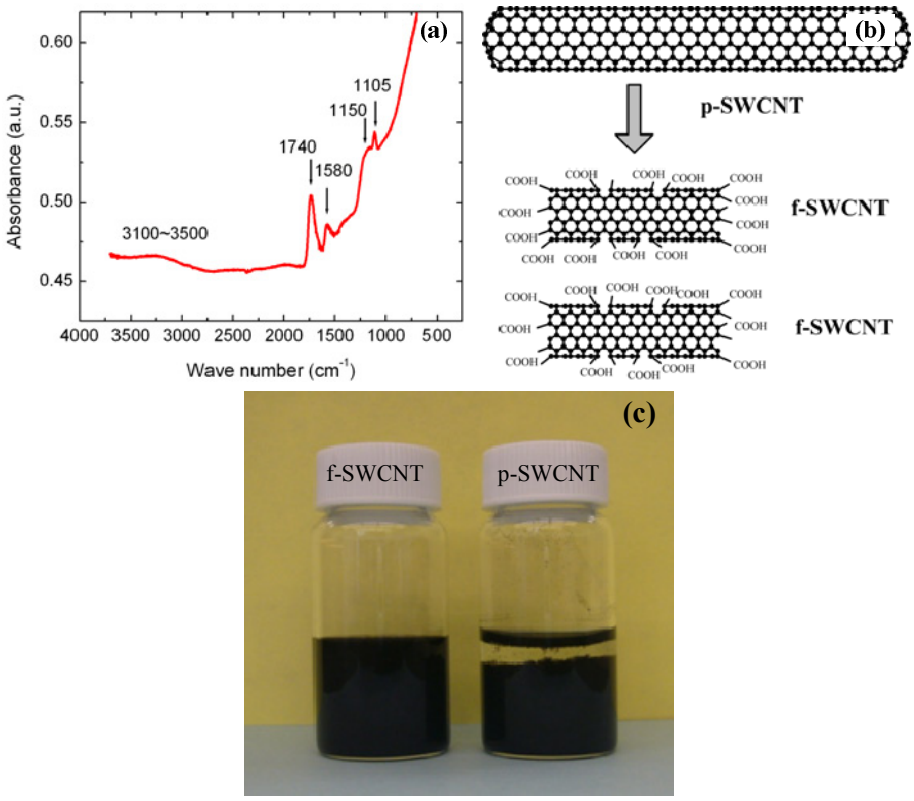

Figure 2-4 Chemical functionalization of p-SWCNTs for layer-by-layer (LbL) self-assembly by concentrated acid treatment: (a) a reflective FTIR spectrum of the f-SWCNTs, (b) schematic process of acid functionalization, and (c) water dispersion of f-SWCNTs 6 months and p-SWCNTs an hour after ultra-sonication

The reflective Fourier transform infrared (FTIR) spectrum of the f-SWCNT film is shown in Figure 2-4 (a). The characteristic absorption peaks are observed at the wave number of 1740, 1580, 1150, 1105 and the broad band of 3100-3500 cm^{-1}. The sharp peaks at 1740 and 1150 cm^{-1} are associated with the stretching vibration of C=O and C-

O, respectively, which are considered as the obvious indication of the functionalization of SWCNTs with carboxylic groups [98]. Furthermore, the broad band on the range of 3100~3500 cm^{-1} originates from the stretching of –OH in the carboxylic acids [99]. The peak at 1580 cm^{-1} is ascribed to the C=C stretching vibration of intrinsic SWCNTs [98]. The sharp peak found at 1105 cm^{-1} is attributed to Si-O-Si vibration of the Si/SiO_2 substrate used [99]. The gradual increase in absorbance observed under the wave number of 1500 cm^{-1} is also caused by the Si wafer as a substrate. Therefore, it is obvious that carboxylic groups are attached as a result of the chemical treatment. In addition to that, it is hypothesized that the p-SWCNTs are fragmented on the site of defects on the side wall and uncapped at both ends, where pentagon rings exist as shown in Figure 2-4 (b). The carboxylic functional group was equipped on both ends as well as the side wall [100]. The chemical functionalization promoted the solubility and stability of SWCNTs in water as shown in Figure 2-4 (c), where the dispersion was stable 6 months after sonication. On the other hand, the water dispersion of p-SWCNTs 1 hour after sonication was precipitated.

2.2.2. Indium oxide and silica nanoparticle

Indium oxide (In_2O_3) nanopowder (INP) was purchased from Sigma-Aldrich, and colloidal silica nanoparticles (SNOWTEX®-XL, 40 wt%) came from Nissan Chemical America Corp. INPs were dispersed into 12 mM of HCl (pH 3.9), due to their neutral isoelectric point of 8.7 [101], with a concentration of 50 mg/ml. 4 g of as-received colloidal silica was diluted to 100 mL of DIH_2O resulting in a concentration of 16 mg/ml with a neutral pH (~ pH 7.0). A Zeta potential and particle size analyzer (ZetaPlus, Brookhaven Instruments Co.) was used to perform dynamic light scattering (DLS) for particle sizing and measure the zeta potential using phase analysis light scattering (PALS). For DLS, 10 mM of aqueous KNO_3 was used as a dispersant to make the concentrations of 0.5 and 0.16 mg/ml for INPs and SNPs, respectively, and the signal was collected five times and averaged. Dispersions of INPs and SNPs described previoulsy were diluted 100 times to DIH_2O for PALS measurement while the pH of dilutions was

kept constant. Ten runs of signal acquisition were done and the electrophoretic mobilities were averaged. All measurement was done at room temperature.

In order to determine the zeta potential (ς) of nanoparticles used, the Smoluchowski equation was used based on electrophoresis, which requires the knowledge of the dielectric constant and the viscosity of the surrounding medium as follows:

$$\mu_{ep} = \frac{\varepsilon_r \varepsilon_0 \varsigma}{\eta}$$

where, μ_{ep} is the electrophoretic mobility of particles, ε_r the dielectric constant of the dispersing medium, ε_0 the permittivity of the free space, ς the zeta potential, and η the dynamic viscosity of the medium. The mobility and zeta potential of INPs and SNPs determined in PALS measurements are summarized in Table 2-1. The mobility of INPs and SNPs was found as 1.8 ± 0.1 and -3.9 ± 0.2 ($\times 10^{-11}$ $m^2V^{-1}s^{-1}$), respectively, from which zeta potentials were extracted as 22.53 ± 0.8 and -48.1 ± 1.2 mV.

Table 2-1 Zeta potential measurement of nanoparticles used in this study

Nanoparticle	In_2O_3	SiO_2
Mobility, μ_{ep} (10^{-11} $m^2V^{-1}s^{-1}$)	1.8 ± 0.1	- 3.9 ± 0.2
Zeta potential, ς (mV)	22.53 ± 0.8	- 48.1 ± 1.2

The DLS data are fitted to a lognormal particle size distribution, which has the probability density function as follows [102]:

$$f(d) = \frac{1}{\sqrt{2\pi} d \ln\sigma} \exp\left[-\frac{(\ln d - \ln d_m)}{2\ln^2\sigma}\right]$$

where d_m is the mean diameter and σ is the standard deviation of the distribution. The lognormal distributions of SNPs and INPs are shown in Figure 2-5. SNPs are monodisdersed with the mean diameter of 50.2 nm and the polydispersity of 0.005 as shown in the inset, while INPs showed two broad peaks at 81.7 nm and 255.1 nm. INPs

are polydispersed due to the possible agglomerations. However, it is noticeable that each peak in INP was well fitted to lognormal distribution. The reason for agglomeration can be attributed to the relatively low zeta potential of INPs.

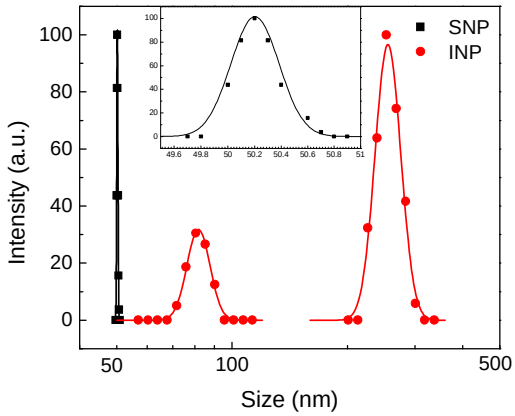

Figure 2-5 Particle size distribution using dynamic light scattering (DLS): INP has two broad peaks at 81.7 nm and 255.1 nm, while SNP distribution reveals one sharp peak at 50.2 nm with polydispersity of 0.005

2.2.3. Polyelectrolytes and other solutions

Polyelectrolytes used for LbL assembly as a polycation and polyanion were poly(diallyldimethyammonium chloride, PDDA, M_w=200~350k, Sigma-Aldrich) and poly(stylenesulfonate, PSS, M_w=70k, Sigma-Aldrich), respectively. The concentration of PDDA and PSS used was 1.4 wt% and 0.3 wt%, respectively, with 0.5 M sodium chloride (NaCl) for a better surface coverage. PDDA and PSS were used to build up the precursor layer for nanomaterial multilayer in order to enhance the surface charge at the initial stage of LbL assembly. They were also used as a pairing species for charged nanomaterials and biomolecules. For example, PDDA was used as a pairing ion for negatively charged CNTs, SNPs, biomolecues such as enzymes and antiboies, while PSS was used as a counter ion for INPs.

The standard pH buffer solutions used for studying the pH sensing mechanisms that are described in Chapter 3 were formulated using sodium phosphates. Phosphate monobasic monohydrate ($NaH_2PO_4 \cdot H_2O$, Mallinckrodt Baker, Inc.) and phosphate

dibasic heptahydrate ($Na_2HPO_4 \cdot 7H_2O$, Mallinckrodt Baker, Inc.) corresponding to the amounts described in Table 2-2 were dissolved into 1 L of deionized water to produce pH buffers on the physiological range (pH 5 to 9) with a buffering power of 80 mM.

Table 2-2 Phosphate buffer chart with buffer strength of 80 mM

pH	5.0	6.0	7.0	8.0	9.0
$NaH_2PO_4 \cdot H_2O$ (wt%)	1.0892	0.9715	0.4669	0.0754	0.008
$Na_2HPO_4 \cdot 7H_2O$ (wt%)	0.0288	0.2574	1.2373	1.9976	2.1284

For glucose biosensors, standard β-D-glucose solutions were prepared by dissolving glucose powder (Sigma-Aldrich) into 1× phosphate buffered saline (PBS, GIBCO, pH7.2, GIBCO, KCl: 2.67 mM, KH_2PO_4: 1.47 mM, NaCl: 137.93 mM, $Na_2HPO_4 \cdot 7H_2O$: 8.06 mM). The concentration of 100 mM glucose was prepared as a stock solution and diluted to produce 2, 4, 6, 8, 10, 20, 50 mM testing solution. Glucose oxidase (GOx, Type VII, lyophilized powder, 50 kU/g, from Aspergillus niger, Sigma-Aldrich) used as the bioreceptor in the glucose sensors. It was also dissolved into 1× PBS to yield stable negative charges with a concentration of 1 mg/mL.

2.3. Sensor fabrication

This section describes the combination of top-down microfabrication and bottom-up nano self-assembly used to fabricate nanomaterial chemoresistors for the application of pH as biological sensors. The general fabrication method of nanomaterial devices for the application of biosensors is discussed as a standard for the case of silicon-based devices and lift-off for the patterning of nanomaterial thin films. It includes the microfabrication of source and drain metal electrodes and LbL nano self-assembly of nanomaterials. The

other methods used for flexible substrates and etching for the patterning of nanomaterials will be described in the corresponding chapters.

First, a standard 4 inch silicon (Si) wafer with silicon dioxide (SiO_2) 2 μm thick was cleaned in a piranha solution (3:1 H_2SO_4:H_2O_2) at 120ºC for 15 minutes, rinsed thoroughly with a copious amount of DIH_2O, and dried with a nitrogen (N_2) stream. Chromium (Cr) and gold (Au) were electron-beam evaporated onto the Si/SiO_2 substrate as electrodes materials, and patterned for source-drain electrodes using photolithography. Another lithographic technique was used to fabricate a photoresist window area through which the LbL nanomaterial film was assembled onto the substrate and to protect the measuring pad from the adsorption of SWCNTs. It also eliminates a possible direct electrochemical reaction between the sample solution and Cr/Au electrode covered with self-assembled nanomateril multilayer in area other than the chemoresistor channel. After developing the photoresist, oxygen (O_2) plasma was used at a power of 100 W for 1 minute with O_2 flow rate of 100 sccm to remove the residual photoresist completely in the opening window as well as to make the surface hydrophilic, which is beneficial to the subsequent LbL assembly.

Next, a few bi-layers of (PDDA/PSS) were self-assembled as a precursor layer on the patterned substrate for the charge enhancement, followed by the assembly of the nanomaterial multilayer, $(PDDA/SWCNT)_n$ or $(INP/PSS)_m$, as an electrochemical transducing material. Following nanomaterial multilayer, depending the application, a dielectric layer of $(PDDA/SNP)_6$ is assembled in order to tune electrochemical properties or to immobilize bioreceptors such as enzymes and antibody-antigen complex structures. The nanomaterial multilayer without bioreceptors was used as pH sensors using the sensing mechanism that will be discussed in following chapters.

2.4. Conclusion

The general background information on LbL assembly and the application of microfabrication techniques for the patterning of nanomaterial thin film has been discussed in this chapter. The preparation of materials such as SWCNTs, INPs, SNPs, polyelectrolytes, and other solutions was discussed in detail and the prepared materials were characterized for the LbL assembly to manufacture a functional thin film as sensors.

3. Nanomaterials pH sensing

The nanomaterial device with a variety of materials and structures is characterized electrochemically in pH buffers aiming at novel pH sensors and further biosensing applications. The appropriate sensing mechanisms are elucidated from the perspective of materials and conventional semiconductor theory in this chapter. The devices fabricated as described in the previous chapter were tested electrochemically using either a the transistor or resistor scheme that is depicted in Figure 3-1. The resistor-type of device, which is called a chemoresistor [103], can be characterized without the external Ag/AgCl reference electrode or applying the gate voltage.

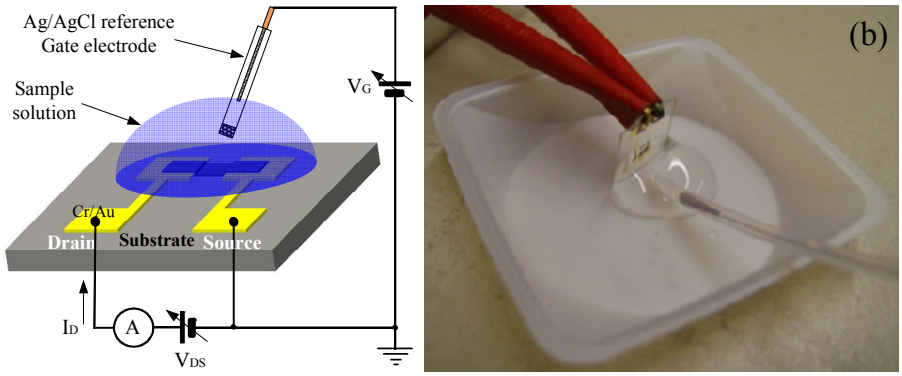

Figure 3-1 The schematic (a) and photograph (b) of pH electrochemical testing using ISFET characterization method: without external Ag/AgCl reference electrode, devices play a role of chemoresitors that use two terminals

In chemoresistors, a bias voltage is applied to the drain electrode with the source electrode grounded, and the current (I) flowing through the nanomaterial multilayer film was measured. At the same bias voltage, different current levels are found depending on the sample solution primarily due to the mutation in the electrical property. The conductance shift due to the sample solutions can be considered as a kind of gate voltage from the conventional semiconductor point of view, although determining on/off state and charge carrier mobility is not straightforward. On the other hand, chemoresistors can

be characterized with an ISFET characterization scheme with the aid of the external Ag/AgCl standard reference electrode. The external gate voltage is applied to boost the effect of the sample solutions on the conductance change of the nanomaterial multilayer. It has been demonstrated that the use of an external gate electrode increases sensitivity, but decreases the sensor resolution with reference to chemoresistors [68]. The miniaturized Ag/AgCl reference electrode (Cypress Systems, EE008) with an internal filling solution of 3 M KCl was immersed into sample solutions as a gate, as shown in in Figure 3-1 (b), to provide the sample solution with the stable electrical potential. After three terminals (source, drain, and gate) were connected to the semiconductor parameter analyzer, the drain-to-source voltage (V_{DS}) and gate voltage (V_G) were scanned to obtain the drain current (I_D) at different samples solutions. During the characterization, the Ag/AgCl reference gate electrode and the readout wires from source and drain electrode were fixed to the external frame to prevent the relative motion. At this time the distance between sensor surface and the tip of reference electrode was about 5 mm. A pipette was used to add 300 μL of sample solution on the sensor surface with reference electrode immersed. The sensors were incubated in each pH buffer solution for 1 minute. A longer incubation time, 3 minutes was used for glucose sensing on the consideration of glucose enzyme retention time and ionic diffusion of reactants and products.

In this chapter, firstly, the pH-dependent conductance behavior of SWCNT multilayer chemoresistors is studied. Current-voltage (I-V) characteristics show that the conductance of the SWCNT multilayer decreases with increase in pH. On the other hand, the SWCNTs chemoresistors with poly(methylmethacrylate, PMMA) as an ionic passivation layer demonstrate an increasing conductance with pH, which is opposite to the case of the absence of PMMA layer. The conductance change in the absence of PMMA attributes to doping/undoping of holes as charge carriers by molecular protonation/deprotonation of carboxylated SWCNTs. With PMMA layer, the concentration gradient of hydrogen ions on the dielectric forms an additional gate bias voltage, which modulates the conductance

of the underlying semiconducting SWCNT layer. Each pH-dependent behavior has versatile applications for chemical and biological detection.

Secondly, the weak polyelctrolyte (wPE) was used as a counter species for SWCNTs instead of using PDDA for LbL self-assembly to control the proximal ions, primarily hydgrogen ions or hydroxyl ions. The wPEs employed here had amino groups possessing different acid dissociation constants (K_a). The LbL self-assembly process was monitored by Quartz crystal microbalance (QCM), which resulted in a linear growth of the multilayer. Different electrical and structural characteristics are shown in comparison with (PDDA/SWCNT) resistors as a standard. The pH sensitivity on the physiological range demonstrates the effect of proximal ions on the conductance of the SWCNT layer due to the electronic nature of SWCNTs and the ability of capturing hydrogen ions in wPEs. This work sheds light on the applicability of nanostructured and/or functionalized SWCNTs with various functional groups as pH sensors and biological sensors.

Lastly, the role of the dielectric silica nanoparticle (SNP) in nanomaterial chemoresistors and ISFETs is studied and discussed through a systematic study. The nanomaterial ISFET sensors that have been developed employed SNPs on top of electrochemical transducing nanomaterials [12, 13, 68, 104]. The authors argued that SNPs acted as a gate dielectric layer in the conventional FET structures. However, SWCNTs without any dielectric layer, e.g. SNPs, showed the pH sensing electrochemical properties and field-effects along with pH sensibility [105]. The SNP layer on top of the semiconducting electrochemical transducing layer plays the role of the charge collecter, influencing the conductance of the semiconducting layer through carrier accumulation. In conjunction with electrochemical properties of nanomaterial itself, the SNP could be used for a variety of electrochemical sensors.

3.1. pH sensing mechanism of SWCNT multilayer*

3.1.1. Introduction

One mainstream of CNT applications is chemical and biological sensors to take advantage of the sensitive electrochemical reaction in surface atoms or functional blocks along with chemical stability. The study of the electrochemical properties [106] leads to significant bio-sensing applications, capable of detecting or monitoring specific biomolecules for diagnostic as well as therapeutic purposes. CNT-based biosensors have detected protein [80], DNA [81], immunoglobulin [82], neurotransmitters [83], and other important biomolecules [84] from the physiological interactions with or without bio-receptors. Among the extensive list of chemical and biological applications reported, pH sensing is of great importance in scientific research and clinics since it plays a key role in biochemical systems, where the solubility, charge of biomolecules, and equilibrium of the biochemical reactions are immensely affected by pH. As a particular example, cancer cells tend to breed in an acidic environment (~ pH 6.5), whereas normal human blood has pH value of 7.35, which slightly decreases to 7.2 by the intake of food [107]. In consequence, pH detection and monitoring provides meaningful health information. Furthermore, there are many biochemical reactions accompanying pH changes by which the concentration of target biomolecules can be traced for bio-sensing applications.

Combined with extremely sensitive electronic properties of SWCNTs, pH sensors have recently been reported [17, 18]. Although the pH sensing mechanism has been generally known to be protonation/deprotonation, it has been interpreted in different ways [17]. The LbL self-assembled nanoparticle or CNT had a pH sensing capability with high sensitivity and fast response [12]. However, the sensing mechanism has not been clearly

---

* Reprinted with permission from D. Lee and T. Cui, *Journal of Vacuum Science and Technology B,* pH-dependent conductance behaviors of layer-by-layer self-assembled carboxylated carbon nanotube multilayer thin-film sensors, Vol. 27, pp 842-848, 2009. Copyright 2009, American Vacuum Society.

understood. In this section, two different types of pH-dependent conductance behaviors of LbL self-assembled polyelectrolyte and SWCNT multilayer thin film are presented. More importantly, the pH sensing mechanism of the LbL film is clearly explained from the semiconductor perspective. Poly(methyl methacrylate, PMMA) was used in order to passivate the ionic penetration into transducing SWCNT film. The fabricated SWCNT sensors showed completely different pH responses from the reports [17, 18] by using carboxyl group f-SWCNTs and a dielectric for the isolation of semiconducting SWCNTs.

3.1.2. Experiments

A thin film structure of [$(PDDA/PSS)_2(PDDA/SWCNT)_5$] was assembled as described in Chapter 2. PMMA was spun to yield about a 300 nm thick film on the SWCNT thin film to compare results of devices with and without PMMA. The devices were baked at 150 ºC for 3 minutes to cure the PMMA. Two types of electrical characterizations were used: current-voltage (I-V) measurement at steady state and dynamic (transient) responses using a semiconductor parameter analyzer (HP 4156A) and data logging system (Agilent 34970A Data acquisition/switch unit), respectively. After adding each pH buffer, the incubation time of 1 minute is allowed to reach the steady state followed by the I-V measurement. The real-time measurement of dynamic conductance of the LbL assembled SWCNT multilayer resistors was performed from initial conductance at the atmosphere to different pH buffers. The fabricated SWCNT thin film was characterized with a field emission gun SEM (JEOL FE-SEM 6500) with an acceleration voltage of 10 kV. Prior to that, the fabricated device was sputtered with a layer of platinum 5 nm thick to enhance the surface conductivity.

3.1.3. Results and discussion

The fabricated LbL assembled SWCNT thin film is illustrated in Figure 3-2. In the LbL multilayer hierarchy, as shown in Figure 3-2 (a), there are $(PDDA/PSS)_2$ as a precursor layer for the charge enhancement and $(PDDA/SWCNT)_5$ as an electrochemical transducer material. The spun PMMA in the outmost layer plays a role of ionic blocking

layer from the bulk pH buffers. The conductance behavior and pH sensing mechanism will be discussed in the absence and presence of the dielectric PMMA. The fabricated SWCNT thin film depicted in Figure 3-2 (b) was submerged into pH buffers with the Ag/AgCl reference electrode connected to the source electrode to provide a stable potential. The current flowing through SWCNT multilayer was acquired at bias voltages from 0 to 1 V.

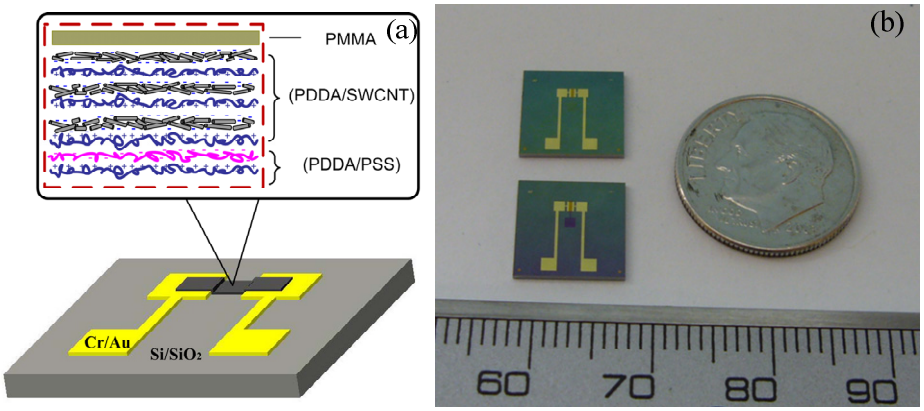

Figure 3-2 A fabricated LbL assembled SWCNT multilayer thin film pH sensor: (a) schematic diagram of the device with a multilayer hierarchy and (b) a photograph of the individual devices

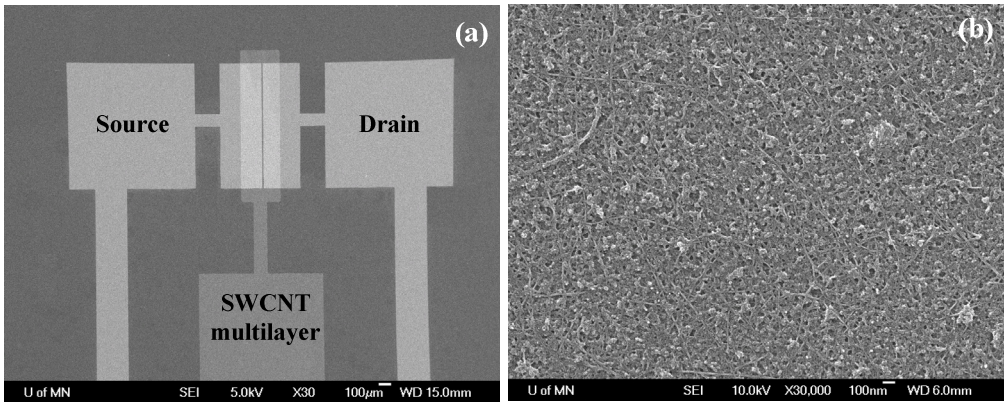

Figure 3-3 Scanning electron micrograph (SEM) image of (a) source and drain electrodes along with SWCNT multilayer film on the channel area, and (b) SWCNT terminated surface

SEM images of the fabricated device are shown in Figure 3-3. The drain and source electrodes along with SWCNT multilayer pattern in the channel area are shown in Figure

3-3 (a). The dimension of the sensing channel used in this study is 10 μm long and 1 mm wide. The surface of $(PDDA/PSS)_2(PDDA/SWCNT)_5$ is illustrated in Figure 3-3 (b), where the individual SWCNTs, bundles, and random network are clearly observed.

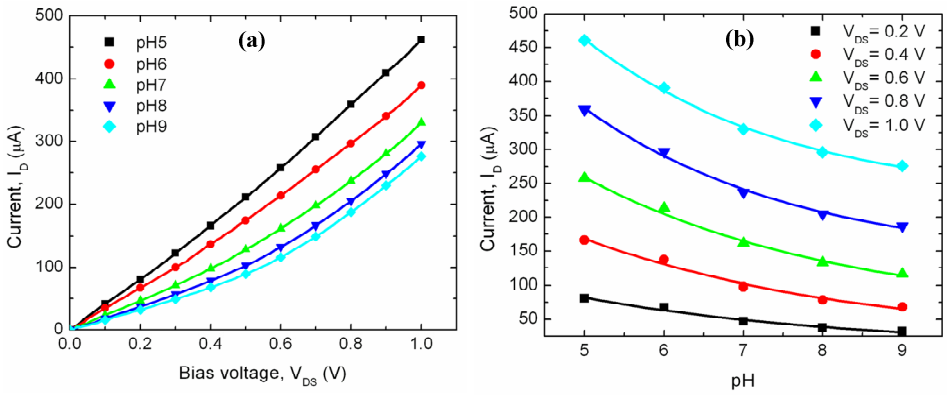

Figure 3-4 I-V characteristics of SWCNT multilayer thin film sensor at different pH buffers (a) and pH-dependent currents at various bias voltages (b) in the absence of PMMA

I-V characteristics of SWCNT multilayer without PMMA layer is shown in Figure 3-4. It is evident that the current decreases with pH increase over the bias voltage used, as indicated in Figure 3-4 (a), which is opposite to the pH-dependent conductance change in the reported results [17, 18]. They argued that the electric conductance of pristine CNTs was changed due to proximal hydrogen (H^+) or hydroxyl ions (OH^-). The pH-dependent conductance behavior shows an entirely different tendency upon grafting carboxylic groups. Moreover, considering that protonation/deprotonation occurs in the carboxylated SWCNTs when pH changes [108], a comprehensive Henderson-Hasselbach equation for carboxyl group f-SWCNT can be described as following:

$$SWCNT - COOH \overset{K_a}{\Leftrightarrow} SWCNT - COO^- + H^+$$

$$\frac{[SWCNT - COOH]}{[SWCNT - COO^-]} = 10^{pK_a - pH}$$

where pK_a is the negative logarithmic value of acid dissociation constant (K_a). The exponential decay function was fit to current values at the same bias voltage and found to

be in strong agreement with experimental data, as shown in Figure 3-4 (b). Consequently, the carboxylated SWCNT behaves as a weak polyacid and the protonation/deprotonation plays an important role in shifting the conductance of SWCNTs at different pH buffer solutions. However, it is noted that the metallic SWCNTs that are predicted as 1/3 of all SWCNTs in thin film [61] provide an offset current and an explicit relationship between [SWCNT-COOH]/[SWCNT-COO^-] and the conductance of the SWCNT has not been reported yet. Additionally, parabolic behavior in the current over bias voltage in each pH buffer, as shown in Figure 3-4 (a), suggests the ionic conductor plays an important role at higher bias voltage by driving salt and its counter ions to flow between the drain and source electrodes. Another possibility is that the contact characteristics changed from ohmic to Schottky between the metal electrode and SWCNT film and/or between SWCNTs due to physical swelling of the LbL film and the intervention of pH buffers.

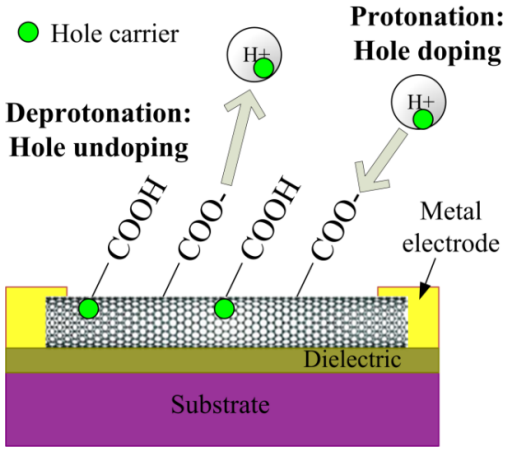

Figure 3-5 Hypothetical model of the conductance shift in carboxylated SWNT by means of protonation/deprotonation from solid-state semiconductor perspectives

Since the carboxylated SWCNTs are a p-type semiconductor [56] protonation/deprotonation can be interpreted as the hole doping/undoping from the solid-state semiconductor perspectives in the absence of PMMA layer. This hypothetical model is illustrated in Figure 3-5, where protonation/deprotonation of carboxylic groups on the surface of SWCNTs is considered as hole doping/undoping as charge carriers. As a

result, the conductance of SWCNTs reflects the collective protonation/deprotonation status of all carboxylic groups on the SWCNT surface.

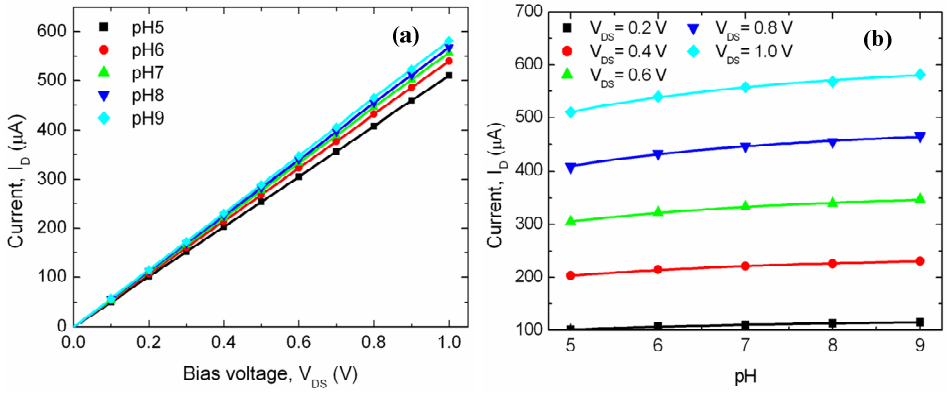

Figure 3-6 I-V characteristics of SWCNT multilayer resistor at different pH buffers (a) and pH-dependent current at various bais voltages (b) in the presence of PMMA layer as a dielectric

I-V characteristics of SWCNTs multilayer chemoresistor with PMMA layer is shown in Figure 3-6. As opposed to the absence of PMMA, the current increases with pH in the presence of PMMA dielectric layer, as shown Figure 3-6 (a). Even though the sensitivity is significantly decreased, a linear dependence of the current on bias voltage in each pH buffer is observed, which means the exclusion of the ionic conductor or Schottky contact barrier passivated by PMMA spin-coating. More importantly, it is considered that the difference in $[H^+]$ between the inside and outside PMMA layer plays a role of the gate voltage due to Nernst potential as follows:

$$V_{H^+} = C \log\left(\frac{[H^+]_o}{[H^+]_i}\right)$$

where C is the proportional constant, $[H^+]_o$ is the hydrogen ion concentration outside PMMA, which is determined by pH of bulk sample solution, and $[H^+]_i$ is the hydrogen concentration inside PMMA. By decreasing the hydrogen ion penetration, the pH increase in the bulk pH buffer solution is equivalent to a negative gate bias from conventional field-effect transistor (FETs). The schematic of this model is illustrated in Figure 3-7.

Therefore, the conductance of SWCNTs multilayer thin film resistor is enhanced as pH increases in the presence of PMMA layer, as shown in Figure 3-6 (b). The main chemical change in PMMA by pH driven hydrolysis of ester groups happens at terminal -O-CH_3 groups, which changes to –OH and in acidic $–O^-$ in basic and environment [109]. In this case, cleavage of PMMA backbone chain does not happen. Consequently, the surface charge induced by the hydrolysis of the ester groups in PMMA reinforces the effect of membrane gate potential induced by bulk pH solution. In acid, H^+ ions are pulled to monomer terminal groups, which gives constricted hydrogen ion concentrations, whereas negative charges are induced in basic solutions. Therefore, the surface charge induced in PMMA can boost gate potential effects in ISFET sensors.

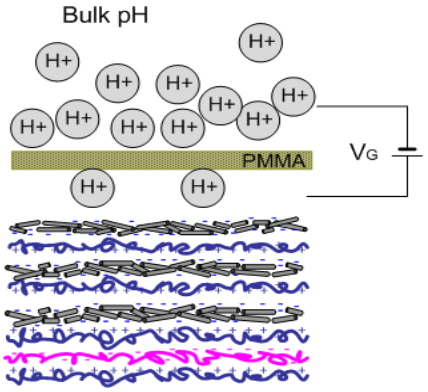

Figure 3-7 Hypothetical conductance shift model in the SWCNT thin film with PMMA passivation layer

Since the protonation/deprotonation is passivated by the PMMA layer, any Schottky barrier effect by the swelling of thin film was not observed. Instead, there is a significant change in ionic composition outside the PMMA layer and in surface charge of PMMA at different pH buffers. Therefore, the membrane potential forms across PMMA by Nernst equation. Furthermore, the pH change in bulk solution corresponds to the mutation of Nernst potential, which influences the conductance of semiconducting nanomaterial thin film.

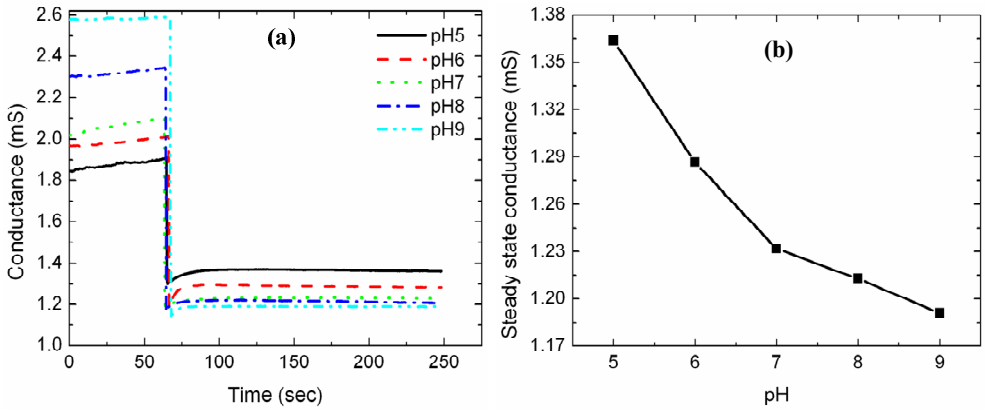

Figure 3-8 Time responses of the conductance change of SWNT multilayer sensor (a) and steady state conductance at difference pH buffer solutions (b) in the absence of PMMA layer.

The time responses of SWCNT multilayer sensors in the absence and presence of PMMA layer are illustrated in Figure 3-8 and Figure 3-9, respectively. The same device was used to characterize dynamic responses at each pH buffer with intermediate rinsing with DIH_2O, followed by drying. The initial conductance difference was substantially observed in the atmosphere, before a corresponding pH buffer was applied in both batches of sensors as shown in Figure 3-8 (a) and Figure 3-9 (a). After the application of pH buffers at the elapsed time of 1 minute, the conductance was significantly decreased and stabilized within 10 and 30 seconds as shown in Figure 3-8 (a) and Figure 3-9 (a), respectively. The abrupt reduction in conductance is primarily caused either by the decrease in interconnection of SWCNTs due to swelling or the surface wetting of the SWCNT thin film. Compared to a relatively stable signal in the buffer solutions, the substantial noise in the atmosphere was caused primarily by the wetting and drying status of the SWNT multilayer thin-film surface and by ambient air flow. The conductance was increased with the time after the intermediate washing since the moisture was evaporated. In addition, the reference electrode could not play a role of providing a stable potential without any buffer solutions. Without PMMA layer, in Figure 3-8 (b) the steady state conductance decreases exponentially with increase in pH, in good agreement with *I-V*

characteristics shown in Figure 3-4 (b). On the other hand, the conductance with PMMA layer increases with pH, which is also consistent with I-V curve in Figure 3-6 (b).

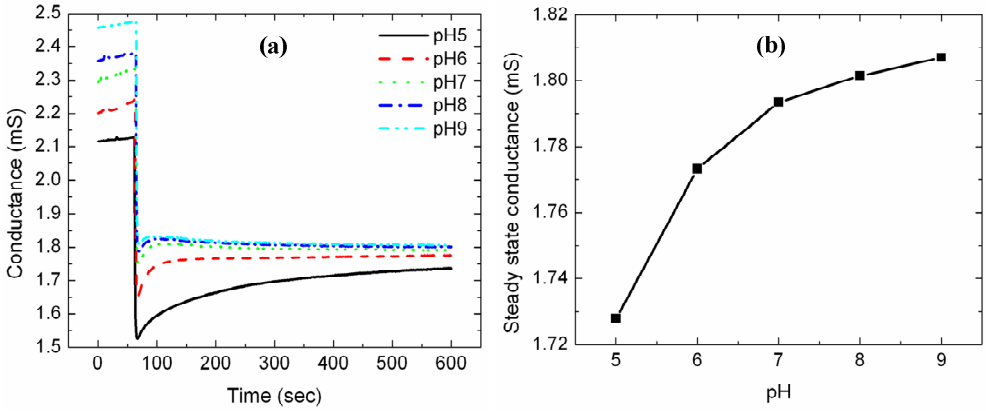

Figure 3-9 Time responses of the conductance change of SWNT multilayer sensor (a) and steady state conductance at difference pH buffer solutions (b) in the presence of PMMA layer

3.1.4. Summary

pH-dependent conductance responses of LbL assembled polyelectrolytes and carboxylated SWCNT multilayer thin-film resistors were demonstrated and the mechanism of conductance change depending on pH was elucidated in the absence and presence of a PMMA dielectric layer. In case of the resistor without the PMMA as an isolation layer, the conductance decreases exponentially with increase in pH. This is justified by hole doping/undoping as charge carriers to p-type semiconducting SWCNTs by means of molecular protonation/deportation. This tendency is completely different from the previously reported results [17, 18], where pristine SWCNTs were used. The different tendency can be attributed to the presence of carboxylic groups on the SWCNTs, having a weak polyacid behavior. In the presence of PMMA as a dielectric, the conductance increases with pH. The ionic Nernst potential across the dielectric layer plays a role of the gate potential for the p-type semiconducting SWCNT layer in a sense of conventional FETs. This device functions as an ion-sensitive FET (ISFET), where the metal gate is removed and ion concentrations act as the electrical potential. Based on the

different pH-dependent conductance mechanisms that we have found, versatile device structures can be constructed for various applications to chemical and biological sensors detecting the reactions accompanying pH change.

3.2. Carbon nanotube/weak polyelectrolytes composites

3.2.1. Introduction

The previous section described the idea that the pH-dependent conductance changes of SWCNT multilayer originates from protonation/deprotonation of SWCNTs. However, the effect of proximal ions on the conductance of the pristine CNTs network or individual CNTs acted in the opposite way with the conductance of CNTs increasing with pH [17, 18]. The authors argued that the changes in the microenvironment of CNTs, mainly hydrogen ions or hydroxyl ions, modulated the charge carrier transfer characteristics, thereby yielding the pH-dependent conductance or current at the fixed bias voltage. Even though it has been known that the ionic composition in microenvironment of CNTs influences their electrical conductance, the systemic studies have not been explored.

In this section, therefore, the effect of proximal ions on the conductance changes of SWCNTs multilayer is studied by employing weak PEs possessing amino functional groups as a pairing polycation instead of using PDDA in LbL assembly. PEs containing amino groups are weakly charged polycations, whose charge is affected by pH of dispersersant. The weak polyelectrolytes (wPE) used here are chitosan (Chit), poly(allylamine hydrochloride, PAH), and poly-L-lysine (PLL) whose molecular structures are depicted in Figure 3-10. All wPEs have the side amino groups that have different acid dissociation constants (K_a) as summarized in Table 3-1. The pK_a value of Chit, PAH, and PLL were reported as 6.5, 8.5 and 10.5 [110]. The wPE has the positive charge of $–NH_3^+$ in case where it is subjected to pH below pK_a and neutral charge of $–NH_2$ at pH above pK_a, so that it is stable in acidic environment as a colloide, which is essential for LbL assembly.

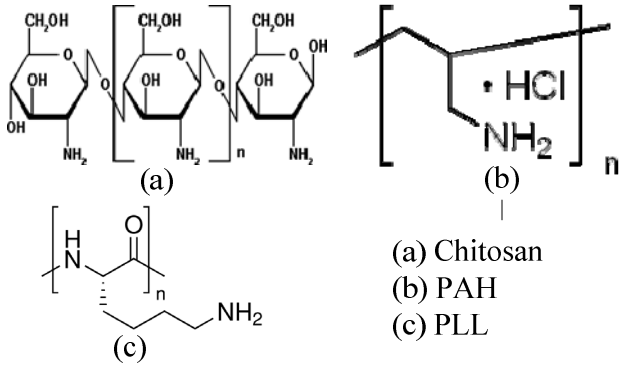

Figure 3-10 Molecular structures of weak polyelectrolytes accompanying amino groups used in this study

The wPEs are interlaid between SWCNTs layers using the LbL scheme. It is possible to perform LbL assembly of positively charged wPE and negatively charged SWCNTs, as schematized in Figure 3-11. The interlaid wPEs have a different capacity of holding hydrogen ions, which influences the conductance of SWCNTs layer. The pH sensitivity of $(Chit/SWCNT)_5$, $(PAH/SWCNT)_5$ and $(PLL/SWCNT)_5$ is characterized using chemoreistor scheme, where two terminals are used for I-V measurement. Their performance will be discussed based on the kind of interlaid wPEs in terms of pK_a, structure, and adsorption phenomena. Furthermore, the results will be compared with $(PDDA/SWCNT)_5$ devices as a standard.

Table 3-1 Specifications of weak polyelectrolyte used in this study

Polyelectrolytes	Charge	pK_a of amino group [110]
PDDA	strong polycation	-
Chit	weak polycation	6.5
PAH	weak polycation	8.5
PLL	weak polycation	10.5

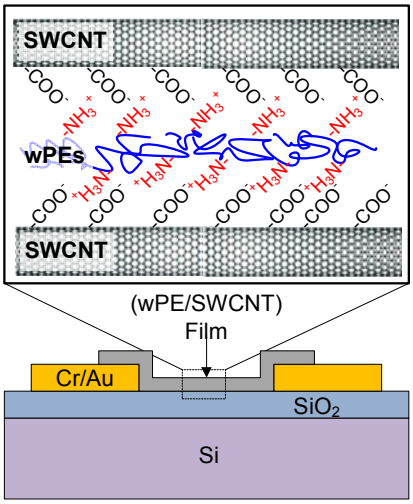

Figure 3-11 A schematic of SWCNT multilayer pH sensors employing weak polyelectrolyte (wPE) containing side amine groups: The different pK_a of wPEs influences the pH sensitivity

3.2.2. Experiments

The wPE solutions were prepared as follows. The chitosan (75-85% deacetylated, Sigma-Aldrich) of 0.1 wt% solution was prepared using sodium acetate buffer (pH5.2, 30 mM, Sigma-Aldrich) to make sure that chitosan polymer have enough positive charge to be a stable solution. PAH (M_w= ~56k) and PLL (M_w= 70-150k) and were obtained from Sigma-Aldrich. The PAH was dissolved into DIH_2O with a concentration of 0.3 wt%, so that the final solution yielded pH 6.4. The PLL was 0.1 wt% aqueous solution at pH 9.0 and used without further treatments. The metal electrodes were prepared and (wPE/SWCNT) multilayer film was pattered in the way that was described previously. The channel dimension tested was 10 μm long and 1 mm wide. After the precursor layers of $(PDDA/PSS)_2$, the LbL assembly of $(wPE/SWCNT)_5$ was performed with the dipping time of 10 min and 15 mins for wPEs and SWCNT, respectively. The LbL process was monitored by quartz crystal microbalance (R-QCM, Maxtek Inc.) at room temperature to evaluate the amount of PEs and SWCNTs and correlate those to surface charge of the previously adsorbed species. The used crystal is the AT cut 9 MHz with the active oscillation area of 0.34 cm^2. Prior to QCM test, crystals were covered with $(PDDA/PSS)_2$ and one additional wPEs layer. The thickness of $(wPE/SWCNT)_5$ films was measured on

12 different spots with surface profiler (P-16, KLA-Tencor) with a force of 2 mg (19.6 μN) and a speed of 20 μm/sec to estimate the internal structure of multilayer. The electrical resistance of devices was measured with semiconductor parameter analyzer (HP4145B). pH sensitivity test was performed for 5 devices with each wPE in the way mentioned previously.

3.2.3. Results and discussion

The fabricated devices are shown in Figure 3-12. The surface of $(PLL/SWCNT)_5$ was characterized with field emission gun–scanning electron microscope (FE-SEM, Jeol 6700) and the image is shown in Figure 3-12 (b). The film morphology does not demonstrate significant difference from $(PDDA/SWCNT)_5$, $(Chit/SWCNT)_5$, and $(PAH/SWCNT)_5$ multilayers.

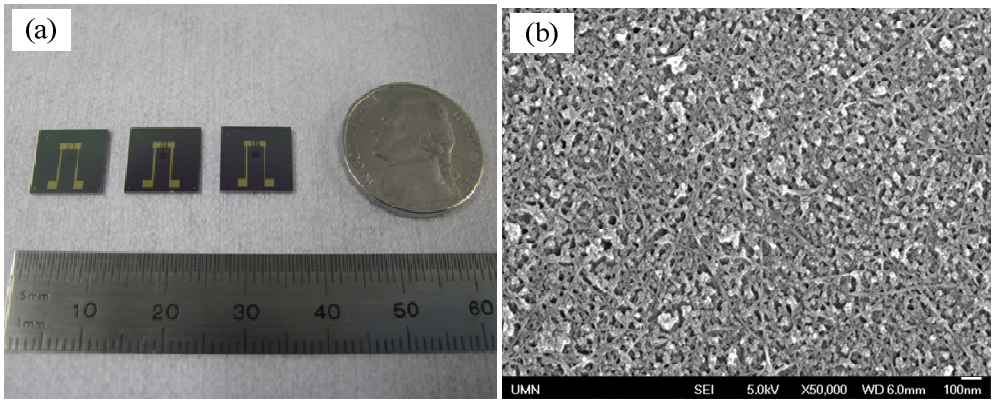

Figure 3-12 The fabricated $(wPE/SWCNT)_5$ multilayer devices for pH sensitivity testing: (a) optical image and (b) SEM image of $(PLL/SWCNT)_5$ devices

The result of QCM measurement is presented in Figure 3-13. It is observed that SWCNT multilayer grows linearly with wPEs as seen in LbL assembly with a strong PE, PDDA [57] in Figure 3-13 (a). Furthermore, it is evident that the growth rate is dependent on the species of wPEs used. The growth rate of (PLL/SWCNT) is the greatest of 3 wPEs tested, showing almost 2 times greater than that of (Chit/SWCNT). The charge and/or conformation of wPE chains may influence the growth rate [111]. The averaged frequency shift for wPEs and SWCNT is depicted in Figure 3-13 (b). While the amount

of wPEs increases slightly, that of SWCNTs increases significantly on the order of Chit, PAH, and PLL, approaching the amount deposited in LbL process of (PDDA/SWCNT). It is obivious to see smaller amounts of PEs and SWCNT due to the weak charge on PEs.

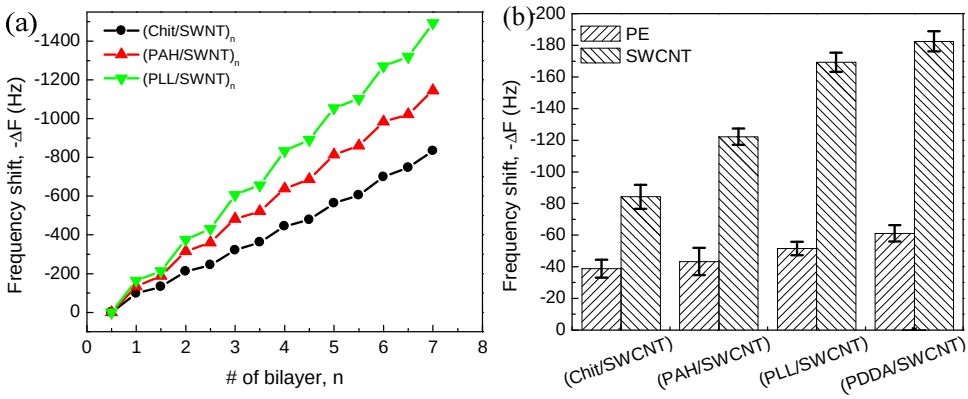

Figure 3-13 Quartz crystal microbalance (QCM) measurement of (wPE/SWCNT) multilayer growth: (a) the monitoring of multilayer growth and (b) the averaged amount of wPEs and SWCNTs in QCM test with the comparison to (PDDA/SWCNTs)

The mass assembled seems to be correlated with the acid dissociation constants (pK_a) and solution pH of wPEs and SWCNT. The pH of wPE solutions was designated in the way that pH is lower than pK_a to make sure that wPEs are stable in the aqueous solution. It is assumed that pK_a of SWCNTs is 4.5, respectively on the following considerations. During SWCNT assembly, the surface of the subrate is covered with wPEs whose charge is dependent on pH of SWCNT solution. The relative surface charge of PEs in SWCNT solution is defined as the substraction of pH of SWCNT solution from pK_a value of wPEs: $pK_{a,\,PE} - pH_{CNT}$. In case of wPEs deposition, on the other hand, the charge of SWCNT-terminated surface is defined as the substraction of pH of wPEs from pK_a of SWCNT ($pK_{a,\,CNT} - pH_{PE}$). The pH and pK_a for each wPE along with relative wPE and SWCNT surface charege in the opposite solutions are summarized in Table 3-2.

The relative surface charge is correlated with the frequency shift, as shown in Figure 3-14. The amino groups on wPEs are protonated or deprotonated depending on pH of SWCNT solution, which corresponds to wPEs surface charge in SWCNTs solution. The

amount of SWCNT absorbed is linearly dependent on the relative surface charge of wPEs assembled in the previous step of self-assembly. In the same way, the carboxylic groups on SWCNTs are protonated or deprotonated depending on the pH of wPE solutions. Therefore, the amount of wPEs is determined by the relative charge of SWCNTs in wPE solutions with a linear relationship. As a result, the amount assembled is in great linear relationship with relative surface charge that was extracted from pK_a of wPEs and SWCNT and solution pH.

Table 3-2 Consideration of pH and acid dissociation constant of wPE and SWCNT in conjunction with frequency shift

PEs	pH	pK_a	Freq. Shift (Hz)			PE surface charge in SWCNT solution ($pK_{a,\,PE}$- pH_{CNT})	SWCNT surface charge in wPE solution ($pK_{a,\,CNT}$ - pH_{PE})
			PE	SWCNT	bilayer		
Chit	5.2	6.5	-38.8	-84.2	-123.0	2.0	-1.2
PAH	6.4	8.5	-43.3	-122.2	-165.5	4.0	-2.4
PLL	9.0	10.5	-51.5	-169.3	-220.8	6.0	-5.0
PDDA [57]	-	-	-61.1	-182.5	-243.6	-	-

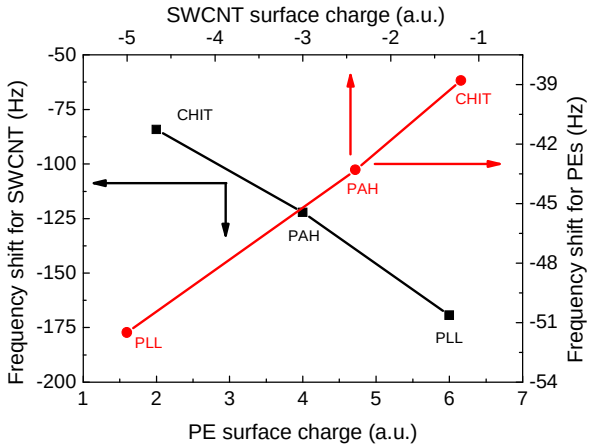

Figure 3-14 A linear relationship of relative surface charge to the amount of species adsorbed during LbL assembly

The resistances were calculated at the voltage of 0.5 V from I-V measurements in semiconductor parameter analyzer (HP4145B). Generally, the weak polyelectrolyte devices had 3 orders higher resistance than $(PDDA/SWCNT)_5$ devices, as shown in Figure 3-15, even though the amount of SWCNT assembled is comparable to that in $(PDDA/SWCNT)_5$ devices. It is apparent that the electrical resistance of SWCNT devices with wPEs is not dependent solely on the amount of SWCNT assembled. For the electrical charge carrier transfer, SWCNTs should be in contact with each other on the same layer or a layer of SWCNT should come in touch with neighboring SWCNT layers. However, wPE chains tend to be more serpentine than PDDA molecules due to the reduced repulsive force between charged side groups. The thickened wPE layer may hamper the physical contacts between the consecutive SWCNT layers.

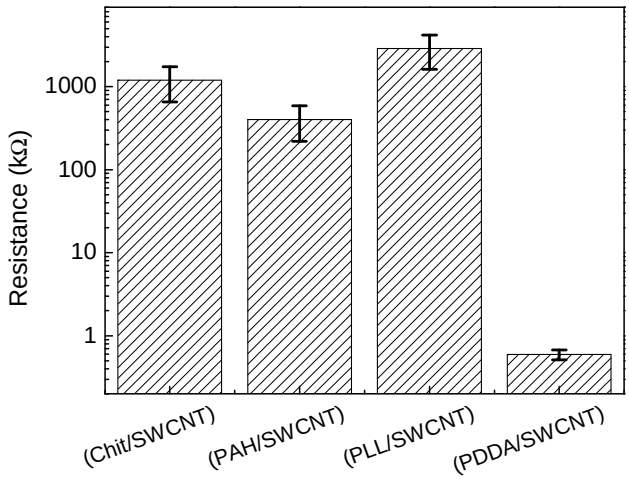

Figure 3-15 The resistances of $(wPE/SWCNT)_5$ with the comparison to $(PDDA/SWCNT)_5$ devices: $(wPE/SWCNT)_5$ shows 3 orders higher resistance than (PDDA/SWCNT) devices

The thickness of $(wPE/SWCNT)_5$ film measured by the surface profiler is shown in Figure 3-16. The thickness of (wPE/SWCNT) multilayer is dependent on the amount of wPE and SWCNT assembled during LbL assembly. However, the thickness of $(PAH/SWNT)_5$ is comparable to that of $(PDDA/SWCNT)_5$ [57]. The thicker PAH layer

due to their weak charge makes the low density, such that SWCNTs penetrate into sparsely packed wPE layer to some degree in next step of LbL assembly, resulting in smaller effective thickness of SWCNT layer. The weak charge induces less amount of SWCNT assembled, but produces thinner film in (Chit/SWCNT) and thicker film in (PLL/SWCNT) than (PDDA/SWCNT). The thickness of $(Chit/CNT)_5$ and $(PLL/SWCNT)_5$ showed the half of and almost double of $(PAH/SWCNT)_5$. A major reason of the doubled thickness in $(PLL/SWCNT)_5$ is a distinctive interlaid PLL layer due to more coiling of polymer chains inside the structure. Indeed, the wPEs made their own characteristics of thin film structures.

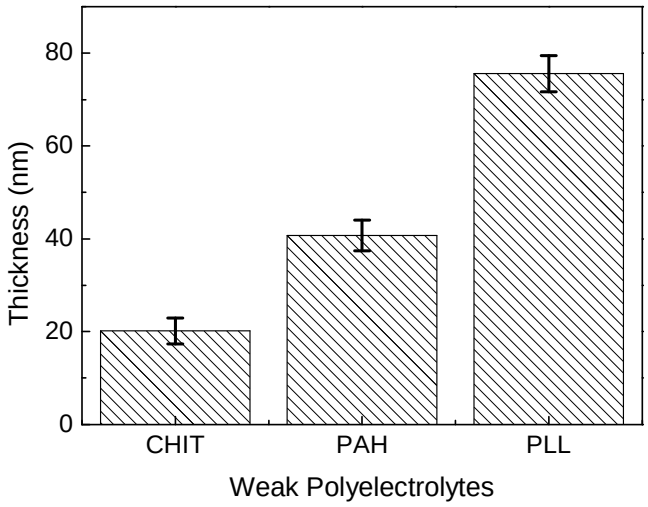

Figure 3-16 Thickness of $(wPE/CNT)_5$ composites measured in surface profiler

After I-V curves were measured at each pH buffer, the currents at the bias voltage of 0.5 V were extracted and plotted as a function of pH. Then, the currents were normalized with the one at pH 5 to compare the general behavior of pH sensitivity. The normalized currents from 5 devices are shown in Figure 3-17. While the normalized current of $(Chit/SWCNT)_5$ decreases slightly and increased after pH 7, the ones for $(PAH/SWCNT)_5$ and $(PLL/SWCNT)_5$ monotonically decrease. However, in the basic region, the normalized current of $(PLL/SWCNT)_5$ is smaller than that of $(PAH/SWCNT)_5$,

which suggests a higher sensitivity at basic region. All (wPEs/SWCNT) devices tested have their own hydrogen ion holding capability in the side functional amino groups, which influences the conductance of SWCNT layer. It is significantly changed in the basic region due to the p-type semiconducting SWCNTs since the increase in pH corresponds to the application of negative gate voltage, resulting in more conductive channel formed within SWCNT layer. It is noted that individual SWCNTs still have their own pH-responsive conductance, which is assumed to have the same effect in three kinds of devices tested. As a result, the tunable pH sensitivity of the (wPE/SWCNT) composit film could be obtained by employing the pairing wPEs with different K_a, which could be more controllable by grafting different functional groups on SWCNTs through other funcationalization schemes.

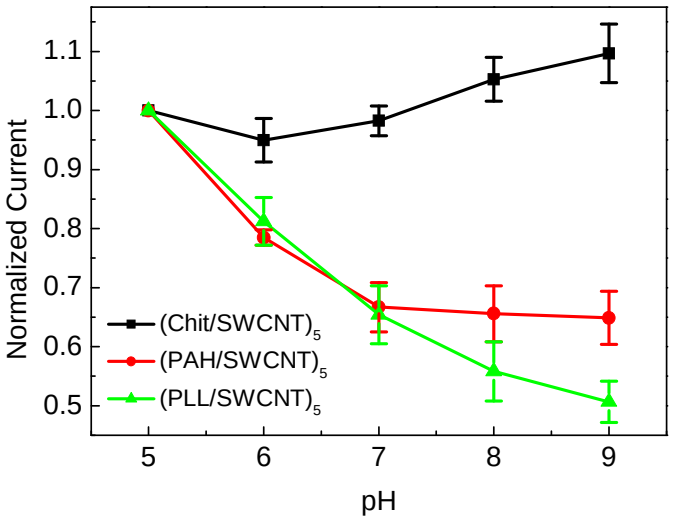

Figure 3-17 pH sensitivity behaviors of (wPE/SWCNT) devices

3.2.4. Summary

The wPE has been used as a paring species along with carboxylated SWCNTs in LbL assembly, resulting in different internal structures from (PDDA/SWCNT) multilayer. The multilayer growed linearly with the number of dipping time and the amount of adsorbed

species was correlated with the surface charge of the opposite species that had been deposited in previous step of LbL assembly. It is proven to be in great linear relationship with the relative surface charge. The (wPE/SWCNT) showed 3 orders higher resistance than (PDDA/SWCNT) devices due to the sparsly packed wPE layer caused by the weak charge. Finally, they exhibited the pH response, which had a different trend of sensitivity in basic region due to the p-type semiconducting SWCNTs.

It has been already reported that carboxylated SWCNTs have exponentially decreasing conductance with increasing in pH on the physiological range [11]. Other works [17, 18] showed pristine SWCNTs exhibited increasing conductance with pH because they were considered p-type semiconductor, so that the conductance of SWCNTs decreased with positive shift of gate voltage due to decreasing hydrogen ion concentration. Indeed, the presence of pH-responsive functional groups on SWCNT plays an important role in tuning the conductance in different pH buffers. Furthermore, the proximal ion effect has been studied in this work by employing wPEs with amino groups possessing different pK_a to control the ability of capturing hydrogen ions in the vicinity of SWCNTs.

3.3. Role of silica nanoparticles

3.3.1. Introduction

A series of nanomaterial-based ISFETs as pH and acetylcholine sensors were reported [12, 13, 68, 97, 104] possessing SNPs as a dielectric layer on top of semiconducting nanomaterial thin film. However, pH buffers or analyte solutions tested in biosensors penetrate significantly into the underlying semiconducting nanomaterial layer due to the porous nature of LbL assembled thin film. The proximal ionic composition change or protonation/deprotonation of the surface functional groups of semiconducting nanomaterials influences the electrical properties of nanomaterial thin film itself as dicussed previously. In case of SWCNT ISFET with SNP dielectrics [104], pH decrease in sample solution induces more positive charge on SNPs surface due to the protonation

of surface hydroxyl group according to the conventional ISFET theory. It plays the role of positive shift in the gate voltage, resulting in decreasing conductance in p-type semiconducting SWCNTs. However, SWCNT ISFET with SNP layer showed the linearly increasing conductance with dereasing in pH [104], which meant the protonation/deprotonation of carboxylic groups on SWCNTs play a dominant role to determine overally behavior in modulating the semiconducting layer. On contrary, the sample solution penetration might be beneficial to n-type semiconducting nanomaterials, e.g. INP, since the gate voltage shift by SNP layer is positive. Nonetheless, this dual effect of solution pH in the presence of SNPs on the conductance of semiconducting nanomaterials makes it difficult to estimate the behavior of nanomaterial devices, exploit new materials, and design novel nanostructures that might have a higher performance. Furthermore, the pH sensing mechanism and role of SNP layer havs not been explained clearly.

The SWCNT multilayer showed the pH-responsive conductance without the aid of SNP layer as reported [105], since the SWCNTs solely demonstrated pH-dependent conductance [10, 11], which suggested the elimination of gate dielectric layer. If SNP layer was used as a dielectric layer as in the conventional ISFETs such as SiO_2, Si_3N_4, Al_2O_3, or Ta_2O_5, etc, the conductance of underlying p-type SWCNTs should be increased with pH, which is the opposite behavior to the reported result. Therefore, in this section, a new analysis on the pH-dependent conductance of SWCNT and INP ISFETs and the role of SNPs layer will be eludicated through the systematic study.

Firstly, the effect of SNP layer on the SWCNTs resistors is evaluated in the atmosphere and pH buffers. SWCNT ISFETs are considered in the same way as the resistor. Finally, in the structure of INP and SNP multilayered film as a semiconducting and dielectric layer, respectively, the effect of SNP layer is evaluated and compared. Based on perfect ion blocking of SNP layer, pH increase is equivalent to the application of negative gate voltage which is favorable to p-type semiconductor resulting in increased source to drain currents. However, it is detrimental to n-type semiconductors, meaning

that pH increase results in the decrease in drain currents (I_D). Therefore, CNT-SNP dual structure had a linear response of source to drain currents. The presence of SNP layer linearizes the exponential behavior of SWCNT layer by increasing gate voltage (V_G) positively. INP-SNP dual structure had exponential response of source to drain currents, but different exponential behavior was found in pure INP layer.

3.3.2. Experiments

The device fabrication process followed the standard method mentioned in Chapter 2. SWCNT resistors were fabricated with and without SNP layer following the sequence of [PDDA (10 min) + PSS (10 min)]$_2$ + [PDDA (10 min) + SWCNT (15 min)]$_5$ and the additional dielectric layer of [PDDA (10 min) + SNP (4 min)]$_6$. Instead of using PSS solution described in Chapter 2, the PSS solution whose pH was adjusted to 3.9 with HCl (PSS2) was used as a pairing species for INP in LbL assembly to preserve the surface charge of INPs in the PSS2 solution. INP ISFETs were fabricated in the sequence of [PDDA (10 min) + PSS (10 min)]$_2$ + [INP (15 min) + PSS2 (10 min)]$_5$ and the additional layer of [PDDA (10 min) + SNP (4 min)]$_6$. The nanomaterial multilayer was fabricated as in the 2nd generation.

The SWCNT multilayer devices can be considered as either resistor due to the presence of metallic SWCNTs or ISFETs due to the semiconducting ones. The presense of metallic SWCNTs deteriorates the functionality of solid-state FETs, resulting in a positive threshold voltage, high leakage current between drain and source electrodes, and low on/off ratio. However, it is valuable for chemical and biological sensors, since they can yield the output signal sensitive to the aqueous environment [105]. Therefore, the SWCNT devices with and without SNP layer were characterized with both chemoresistor and ISFET characterization scheme. On the other hand, the INP ISFETs regardless of the presence of SNP layer were characterized with ISFET characterization scheme. In chemoristor scheme, I-V measurement was performed in semiconductor parameter analyzer (HP4146B) at pH buffers, and the currents at the fixed bias voltage are

demonstrated as a function of pH. In ISFET scheme, the drain-to-source voltage (V_{DS}) was scanned from 0 to 1 V at the fixed gate voltage (V_G), the drain currents (I_D) were obtained at various pH buffers. The extracted I_D was illustrated versus pH. A dozen of device types were characterized, normalized and averaged.

3.3.3. Results and discussion

The surface of semiconducting SWCNT and INP surfaces as well as SNP layers on top of SWCNT and INP, respectively, were characterized in field emission gun scanning electron microscope (FE-SEM, Jeol 6700), and SEM images are presented in Figure 3-18. The SWCNT and INP semiconducting layers are shown in Figure 3-18 (a) and (c), while SNP layers on top of SWCNT and INP are shown in Figure 3-18 (b) and (d), resepctivley. The different surface morphology is observed in (b) and (d) presumably due to the underlying semiconducting SWCNT and INP layer.

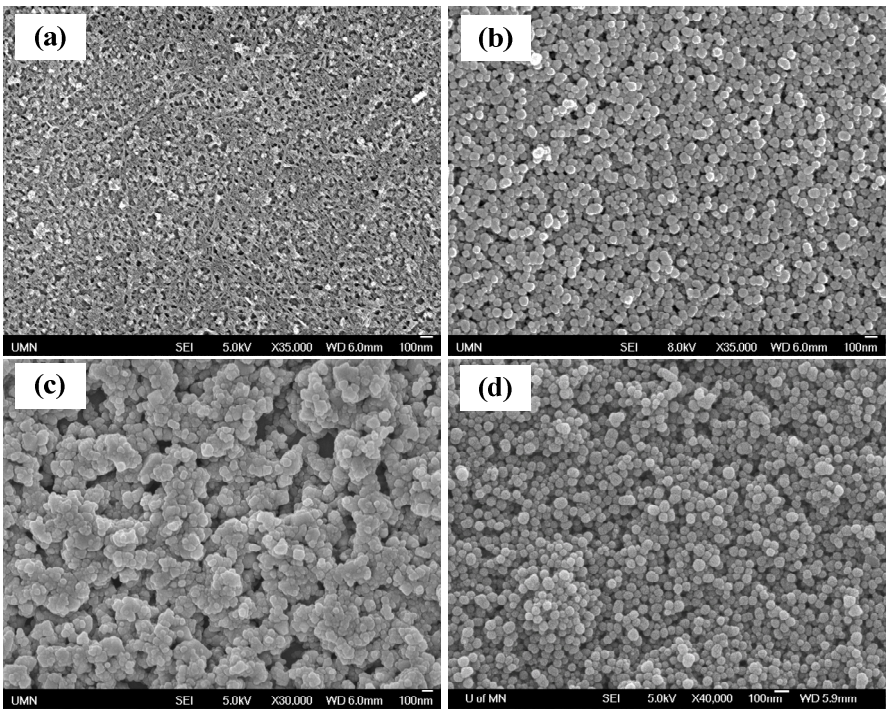

Figure 3-18 SEM images of SWCNT (a) and SNP (b) surfaces in SWCNT ISFETs, and INP (c) and SNP (d) surfaces in INP ISFETs: the differences between (b) and (d) is surface roughness induced by underlying SWCNT and INP multilayer

Firstly, I-V measurement was performed for SWCNT resistors with and without SNP at the atmosphere. The device showed a linear realationship between the current and voltage in both forward and negative biases, suggesting the ohmic contact between SWCNT film and metal electrodes, and between SWCNTs. The resistance was extracted at the bias voltage of 1 V, and results are shown in Figure 3-19. The resistances on the variable channel lengths of 5, 10, 20, and 50 μm with the fixed width of 1 mm are shown in Figure 3-19 (a). The resistance of devices with SNP is 50-60 % higher than that of devices without SNP layer. The surface adsorption onto SWCNTs seemed to be the primary reason for the increased resistance due to the reduced free surface permitting less charge carrier transfer. This phenomenon has been found in the suspended SWCNT film discussed in chapter 2. The resistivity is calculated from the slop of fitted lines based on the assumption that the thickness of the film is 38 nm [57]. The resistances of the film are found to fit to R = 39.94 Ω/μm×L + 225 Ω and R = 57.76 Ω/μm×L+ 378 Ω for device without and with SNPs, respectively, where L is the channel length. The resistivity found is 0.15 and 0.22 Ωcm, and contact resistances between metal electrodes and SWCNT film were found as 113 and 189 Ω for the resistors in the absence and presence of SNP layer. The resistivity of SWCNT film with SNPs on top is 45 % greater than that of the film without SNPs. The sheet reistance versus the channel length are shown in Figure 3-19 (b) in order to compare the sheet resistance on the different channel length. The sheet resistance of SWCNT multilayer with SNP is 50-60% higher than that of SWCNT without SNP. The sheet resistance calculated from the resistivity determined in Figure 3-19 (a) was 39.94 and 57.76 Ω/□ without and with SNP layers, respectively. It is clearly noted, furthermore, that the sheet resistance of CNT film fabricated as bulky paper in the vacuum filtering showed 356 Ω/□ [112], which is greater than the LbL assembled film in this work. The chemically functionlized SWCNTs showed lower sheet resistance of 200 Ω/□ [113], but it is still bigger than the sheet resistance found in this work. The sheet resistance of SWCNT film is known to be dependent on the amount of SWCNTs [112, 114], which means a high loading of SWCNTs can be implemented using LbL self-

assembly. However, the sheet resistance of film regardless of the existence of SNPs decreases as the channel length increases reaching the values calculated from resistivity.

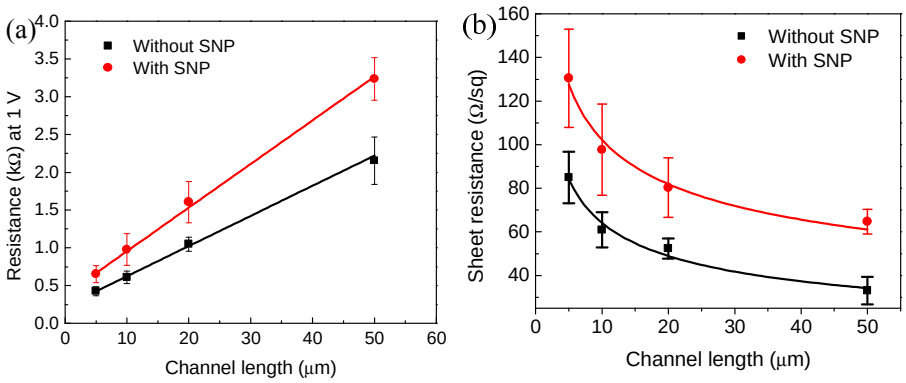

Figure 3-19 Resistances (a) and sheet resistances (b) of SWCNT resistors with and without SNP layer on variable channel lengths of 5, 10, 20, and 50 μm with the fixed width of 1mm

A typical pH sensitivity of SWCNT resistor without SNP layer is shown in Figure 3-20. I-V curves at different pH buffers are shown in Figure 3-20 (a) and the currents are extracted from the bias voltage of 1 V and replotted as a function of pH as shown in Figure 3-20 (b). The pH-responsive current exhibits the behavior well fit to exponential function. On the other hand, pH sensitivity from the SWCNT resistor with SNP layer illustrated in Figure 3-21 showed a linear response. The exponential behavior without SNP layer is in good agreement with previous results reported [10, 11]. It is obivious that the device with SNPs had higher resistance in nature as shown in Figure 3-19, but higher currents at pH buffers. This conflicting phenomenon may come from 2 aspects. First, the significant swelling effect in SWCNT multilayer is found, which might decrease with SNP layer. Second, the accumulation mode of conducting channel might be induced due to the charges on SNP layer, even though the molecular doping/undoping happens. The SNP layer might play an important role of modulating pH sensitivity.

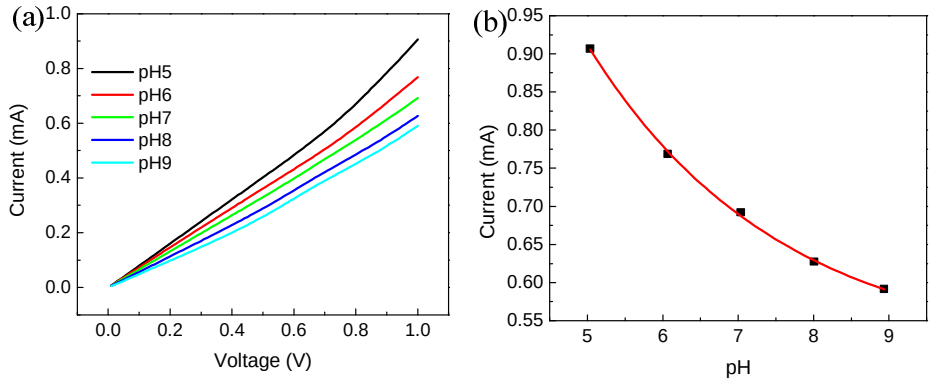

Figure 3-20 A typical pH sensitivity of SWCNT chemoresistor without SNP layer: (a) I-V curves at different pH buffers and (b) exponential pH-responsive currents at the bias voltage of 1 V

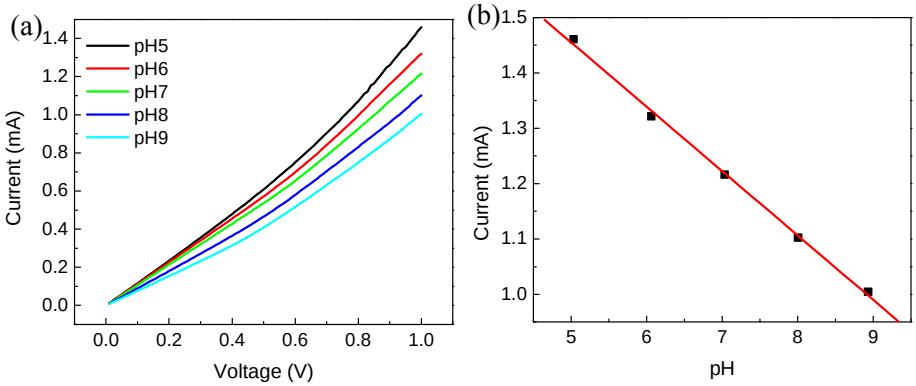

Figure 3-21 A typical pH sensitivity of SWCNT chemoresistor with SNP layer: (a) I-V curves at different pH buffers and (b) linear pH-responsive currents at the bias voltage of 1V

The multiple devices were tested and normalized with the current at pH 7 and averaged to estimate the general behavior of pH sensitivity of SWCNT chemoresistors. The reason why the current at pH 7 was chosen is that the deprotonatin of –SiOH takes place at pH 6.8. SNPs play a role of charge collector, depending on pH of bulk solution as shown in Figure 3-22 (a), such that it may shift to positive or negative depending on the protonation/deprotonation of the surface hydroxyl groups. Decrease in pH induces protonation of –OH or $–O^-$ and increase in pH results in the deprotonation of –OH or $–OH_2^+$ [115]. So protonation/deprotonation are equivalent to positive/negative shift in pH gating voltage, thereby resulting in decreasing/increasing conductance of the underlying

SWCNTs. Furthermore, the surface functional groups of $-SiOH_2^+$ could be formed through the protonation of –SiOH below pH 2.3. In acidic environment, the conductance of SWCNT increases due to the hole doping of SWCNTs, but decreases due to the positive gate bias caused by SNP layer. Overally, the effect of direct doping/updoping plays a dominant role in pH sensitivity as shown in Figure 3-22 (b), and the SNP layer may modulate the sensitivity and linearize the response particularly in acid.

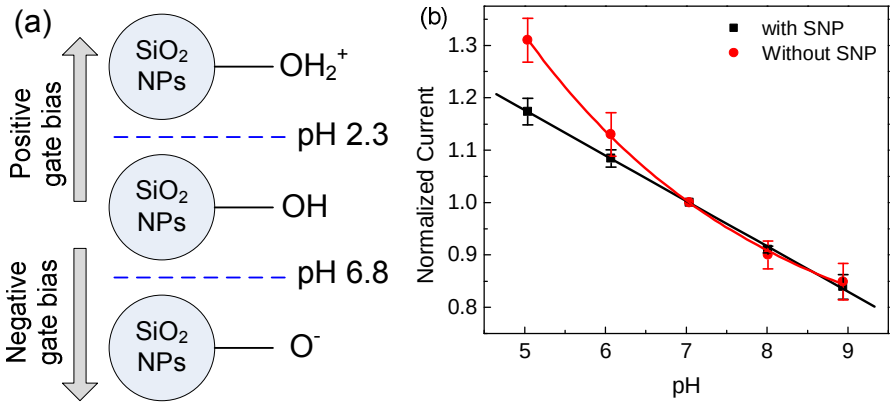

Figure 3-22 General behavior of SWCNT chemoresistors without and without SNPs: (a) scheme of pH-responsive surface functional groups in SNPs and (b) pH sensivity of SWCNT resistor normalized with the current at pH 7 in the presence and absence of SNP layers

SWCNTs multilayer was characterized with ISFET scheme with aid of reference electrode. A typical pH sensitivity of SWCNT ISFETs without and with SNP layer is shown in and Figure 3-24, respectively. Commonly, the explicit field-effects are observed regardless of the existence of SNPs as functionality in Figure 3-23 (a) and Figure 3-24 (a). The I_D versus V_{DS} curve was extracted from each pH buffer and replotted in Figure 3-23 (b) and Figure 3-24 (b). However, pH sensitivity found in in Figure 3-23 (c) and Figure 3-24 (c) is significantly different each other. The SWCNT ISFET with SNP showed linear pH response, which the one without SNP revealed exponential relationship. This can be attributed to adjusted sensitivity particularly in acidic region due to positive charge collector, thereby causing derease in conductance.

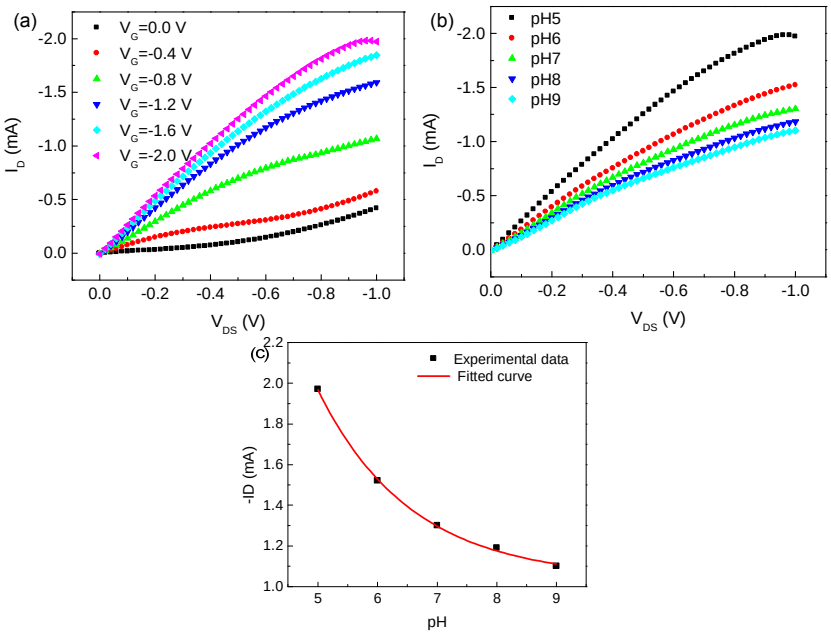

Figure 3-23 A typical pH sensitivity of SWCNT ISFETs without SNP layer: (a) field-effect test at pH5 buffer, (b) drain currents at different pH buffers at the fixed V_G= -2.0 V, and (c) exponential pH-responsive drain at the fixed V_G= -2.0 V and V_{DS}= -1.0 V

Generally, the SWCNT ISFET showed the same tendency as SWCNT chemoresistors as shown in Figure 3-25: linear and exponential sensitivity in the presence and absence of SNPs. Indeed, SNP layer linearizes the pH response in both SWCNT chemoresistor and ISFET. Furthermore, it is observed that the sensitivity in ISFETs increased compared to the chemoresistors in the presence of SNPs, whereas more sensitive response is shown only at acidic environment in ISFETs compared to the chemoresistors in the absence of SNPs. With SNPs, the p-channel formed by the use of external reference electrode diminishes due to positive charge of hydroxyl groups in SNP, allowing less drain current in response to pH. Therefore, SNP layer play a role of forming conductive channel in SWCNT film by collecting the charges in bulk solution. However, the other part of SWCNT can change their conductance by molecular doping/undoping. The use of external reference electrode enhances the condutive channel and reduces the effect of molecular doping/undoping.

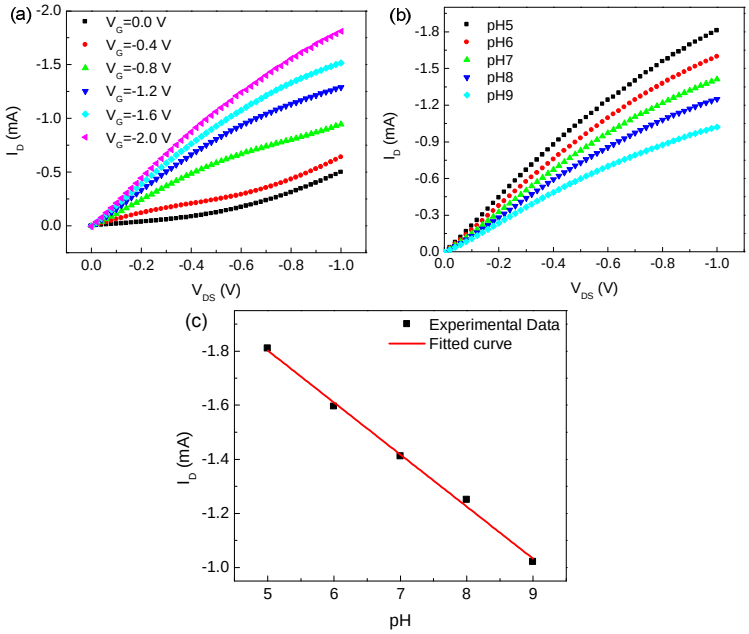

Figure 3-24 A typical pH sensitivity of SWCNT ISFETs with SNP layer: (a) field-effect test at pH5 buffer, (b) drain currents at different pH buffers at the fixed V_G= -2.0 V, and (c) linear pH-responsive drain at the fixed V_G= -2.0 V and V_{DS}= -1.0 V

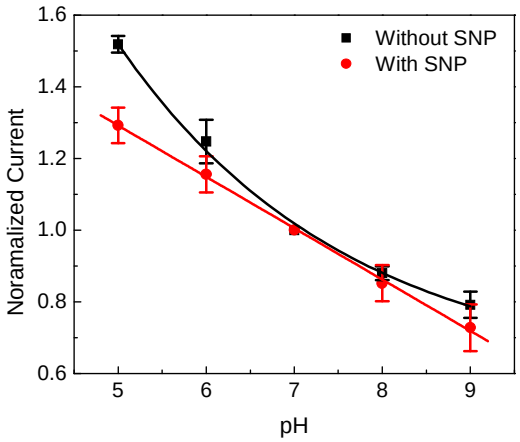

Figure 3-25 pH sensivity of SWCNT ISFETs normalized with the current at pH7 in the presence and absence of SNP layers

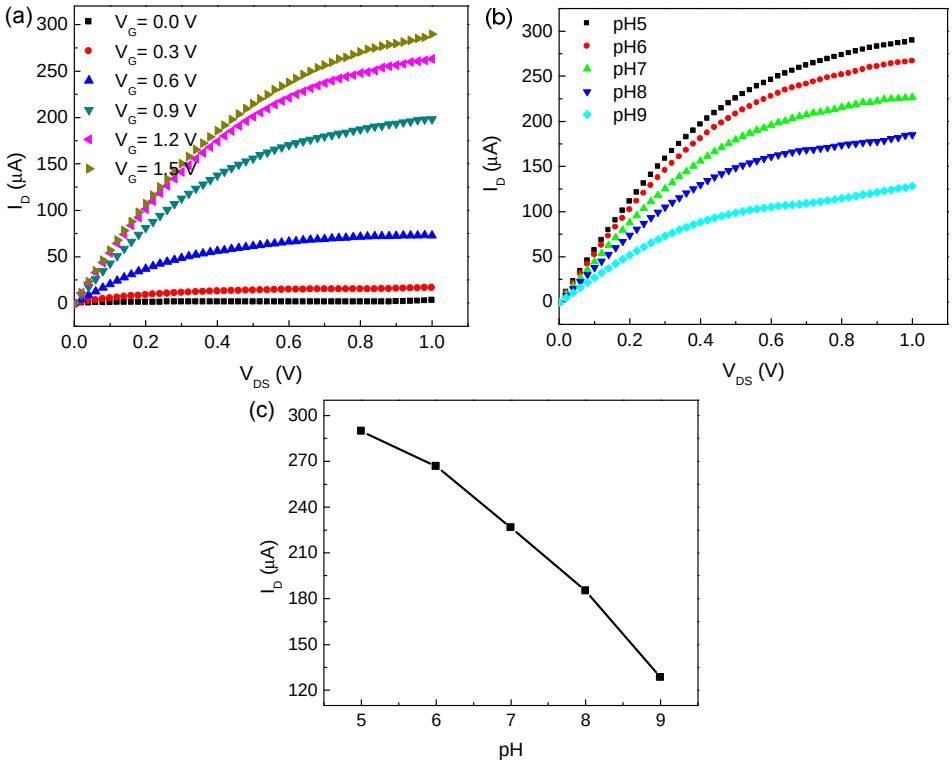

Figure 3-26 A typical pH sensitivity of INP ISFETs without SNP layer: (a) field-effect test at pH5 buffer, (b) drain currents at different pH buffers at the fixed V_G= 1.5 V, and (c) pH-responsive drain currents at the fixed V_G= 1.5 V and V_{DS}= 1.0 V

Also, INP ISFETs were constructed with and without SNP layer and characterized with ISFET characterization scheme. The different level of V_G was chosen to get reasonable field-effect at pH 5 buffer as shown Figure 3-26 (a) and Figure 3-27 (a). The I_D versus V_{DS} curve was extracted from each pH buffer and replotted in the same way done for SWCNT ISFETs. It is noticeable that the effect of SNP layer is different from the one observed in SWCNT ISFETs. The pH shift induces the change of protonation/deprotonation status in both INPs and SNPs. Without SNPs, the protonation status on INP surface determines the conductance of film by space-charge model [103]. The pH decrease corresponds to less negative charges on the surface that makes space-charge layer thinner, leading to the reduced the interparicle Schottky barrier. The reason why a higher sensitivity was found in basic region is that isoelectric point of INP is 8.7

[101]. On the other hand, in the presence of SNPs, the effect of SNP comes into play keeping the effect of space-charge model. The pH decrease corresponds to the positive shift on SNP, which accumulates the conducting electrons, permitting more current. It is apparent that the sensitivity is higher in acidic region on the consideration that silica surface keeps being protonated as mentioned earlier.

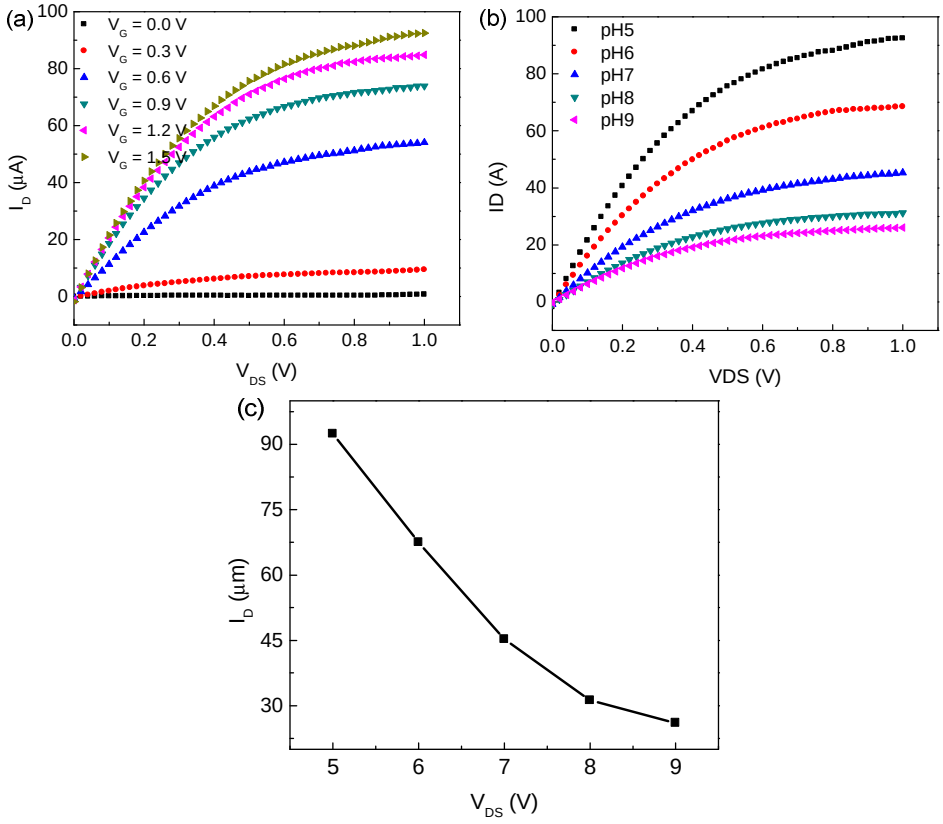

Figure 3-27 A typical pH sensitivity of INP ISFETs with SNP layer: (a) field-effect test at pH5 buffer, (b) drain currents at different pH buffers at the fixed V_G= 1.5 V, and (c) pH-responsive drain currents at the fixed V_G= 1.5 V and V_{DS}= 1.0 V

3.3.4. Summary

The various structures of SWCNT and INP devices have been characterized electrochemically in pH buffers, and the effect of the existence of SNP layer on the

conductance of underlying semiconducting material has been evaluated. In SWCNT resistors, SNP played role of increasing resistivity, contact resistance, and sheet resistance by the surface adsorption. However, in SWCNT chemoresistors, it linearized pH sensitivity from exponential behavior in the device without SNPs particularly in acidic region. This linearization is attributed to a positive shift in pH gating voltage in p-type SWCNTs. A similar effect was observed in SWCNT ISFETs, but it resulted in a higher sensitivity in presence of SNPs. In the same way, SNP played the role of changing surface charge, thereby gate voltage effect on the semiconducting INP layer. Without SNP, INP ISFET is in the mode of space-charge. By adding SNP layer, the pH gating voltage come into play and sensitivity showed increasing conductance upon decreasing pH. The difference of sensitivity curve shape orginates from the different isoelectric point of INP and SNPs.

3.4. Conclusion

In conclusion, various pH sensitivities are found in the nanomaterial devices in the form of either chemoresistors or ISFETs. They depend on the materials themselves, structures, and electrochemical characterization methods. Therefore, pH sensitivity can be modulated by employing appropriate nanomaterials and nanostructures. Particlularly, the ability of nanotechnology to tailor the size, structure, composition and surface chemistry may yield engineered nanomaterials or nanostructured sensing platform with a higher performance. The nanoengineered pH sensors could be a cornerstone in the future for developing biologica sensors since many biochemical reactions accompany pH shift.

pH sensors demonstrated in this study may show primarily either linear or exponential response due to the surface functional groups on the nanomaterials and electrochemical transducing thin film structures. The sensors that showed linear responses have potential applications to detect molecules that have a huge change during the biochemical reactions due to the log scale nature of pH. In addition, it can be applied for the detection of

pathogens as a variety of assays. On the other hand, the sensors with the exponential response to pH are used to detect the molecules that have changes on the same order (e.g. glucose). This development scheme of biosensors based on pH sensing behavior is depicted in Figure 3-28. Furthermore, there is more room to develop nanomaterial pH sensors either by functionalizing nanomaterials with various surface groups with more sensitive to chemical changes in sample solution or by exploiting elegant and novel nanostructured sensing elements. In the meantime, biosensors can be implemented in a variety of ways that the sensing performance is maximized.

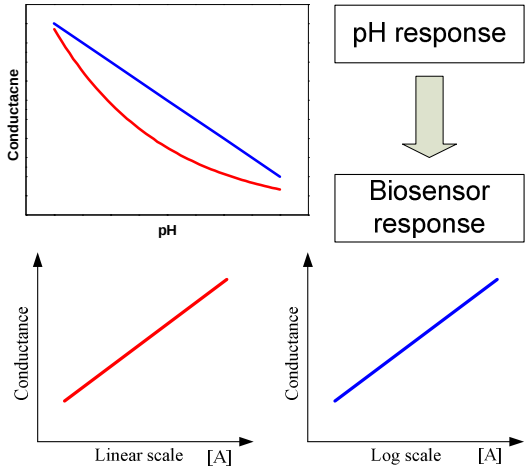

Figure 3-28 The developmental scheme of biosensors based on pH sensing behavior: different pH responses induces different type of response from biosensors

4. Nanomaterial glucose sensors

Glucose is one of the most important carbohydrates in human body, since cells utilize it not only as an energy source but also as metabolic intermediates. Normally glucose level in blood is regulated on the range of 4-8 mM (70 to 150 mg/dL in the U.S). Both hypoglycemia and hyperglycemia result in fatal problems. Since glucose is the sole energy source in some organs such as brain, testes, erythrocytes and kidney medulla, hypoglycemia may cause various symptoms: nonspecific "not feeling good", coma and permanent brain damage. On the other hand, prolonged hyperglycemia may be associated with organ damages, especially the kidneys, eyes, nerves and vessels. According to World Health Organization (WHO)[†], at least 171 million people suffered from diabetes in 2006, and it is estimated to be double by 2030. 7% of US population, 20.8 million people, suffered from diabetes, and it is rapidly increasing. National Diabetes Information Clearinghouse (NDIC)[‡] estimated in 2002 that diabetes cost $132 billion in the United States alone every year.

The incorporation of nanomaterials to devices as a sensing element as well as enzyme immobilization sites is beneficial to develop enzymatic biosensors. In general, the enzymatic biosensors are suffering from the lack of simple and stable immobilization method and the denaturation. However, CNTs and nanoparticles are biocompatible such that the immobilized enzyme on nanomaterials retains its activity and structure [116, 117]. Furthermore, they accommodate a large amount of enzyme due to the huge surface-to-volume ratio, which can be tethered to biomoleclues. Recent efforts to immobilize enzymes onto nanomaterials were demonstrated with the great enhancement of sensor capabilities [118, 119]. Hydrogen peroxide sensor using gold nanoparticles for horseradish peroxidase (HRP) immobilization sites was fabricated [120]. In addition, enzyme ion-sensitive FET (ENFET) was constructed for glucose sensing using silica

[†] http://www.who.int/en/

[‡] http://diabetes.niddk.nih.gov/

nanoparticles as an immobilization matrix on the gate dielectric [121]. In both cases, fabricated sensors had a high sensitivity and extended lifetime due to the biocompatibility and high enzyme activity. Also glucose sensor prepared by silver and gold nanoparticles showed an increased sensitivity and stability [122]. Moreover, layer-by-layer constructed aminated silica nanoparticles/GOx sensor can tune performance such as sensitivity and detection limit by controlling the number of layers [123]. The activity of LbL assembled GOx/Au nanoparticle increased with the increasing number of depositions [124]. Besteman *et al.* [125] suggested the use of individual semiconducting SWCNTs on which GOx was immobilized for glucose sensing. The solid gate was replaced by hydrogen ions that alter SWCNTs conductance.

In this section, nanomaterials are extensively used to develop glucose biosensors. The ion-sensitive SWCNT and INP/SNP glucose sensors are constructed based on the pH sensing mechanism explored in Chapter 3. Firstly, CNTs conductometric glucose chemoresistor sensors composed of SWCNT and GOx on the silicon substrate is introduced. The concentrations of glucose are electronically characterized based on the fact that hydrogen ions from glucose oxidation with the aid of GOx change the local pH value in the vicinity of SWCNT multilayer thin-film, thereby yielding a higher conductance. The overall sensitivity is 10.8 μA/mM and the resolution of device fabricated is 1 pM at the bias voltage of 0.6 V.

Secondly, low-cost, transparent, and flexible ion-sensitive field-effect transistors (ISFET) constructed on a polyethylene terephthalate (PET) substrate are presented for pH/glucose sensing. The pH sensing is accomplished by the same mechanism as SWCNT ISFET built up on silicon wafer. Glucose is detected by the local pH change in the vicinity of SWCNTs with the aid of glucose oxidase (GOx) enzyme. The glucose sensor shows a sensitivity of 18-45 μA/mM on a linear range of 2-10 mM. The apparent Michaelis-Menten constant (K_m^{app}) is 14.2 mM, indicating a high affinity of LbL assembled GOx to glucose.

Lastly, a conductometric INP/SNP biosensor array is presented to address the significant electrical property variation in nanomaterial biosensors due to the nature of random network. To demonstrate enzymatic biosensing capability, glucose oxidases (GOxs) are immobilized on the SNPs layer for glucose detection. It is successfully demonstrated that glucose is detected in many different sensing sites within a chip leading to the concentration dependent currents. The sensitivity is found to be dependent on channel length of the resistor, 4-12 nA/mM on the channel lengths of 5-20 μm, while the apparent Michaelis-Menten constant (K_m^{app}) is invariable at 18-20 mM. This work shed light on the applicability of the developed microsensor array to multi-analyte sensors, novel bioassay platforms, and a sensing components in lab-on-a-chip system.

4.1. SWCNTs chemoresistor sensor[§]

4.1.1. Introduction

The glucose sensors are in the forefront of recent advances in biosensors due to the high demand of diabetes diagnosis and the necessity of the monitoring glucose level in the fermentation process in the food industry. Most glucose sensors have been developed as an amperometric type, where electrons are transferred from the glucose to the solid-state electrode with or without the aid of glucose oxidase (GOx) as a catalyst. Emphasis has been placed on the surface modification of metal electrodes to increase the sensitivity and reduce the response time. The surface modification by various functional nanomaterials has become the main stream of electrochemical sensors to exploit their novel properties. MWCNT modified glucose sensors showed higher sensitivity and longer stability than glassy carbon based sensors [126]. As a further advance form,

[§] © 2009 IEEE. Reprinted with permission from IEEE Sensors Journal, Layer-by-layer self-assembled single-walled carbon nanotubes based ion-sensitive conductometric glucose biosensors, D. Lee and T. Cui.

MWCNTs were decorated with nanoparticles [127] and conducting polymers [128] to enhance the electrochemical property of CNTs themselves. Recently, combined with a facile LbL self-assembly technique, CNT was deposited on the electrode surface to construct the glucose sensors alternated with GOx [129], gold nanoparticles [130], and both chitosan and GOx [131]. Other electrochemical glucose sensors are conductometric types based on ion-sensitive field effect transistors (ISFETs). Nanomaterial based glucose sensors were constructed using SiO_2 [121] and MnO_2 nanoparticles [132] in combination with GOx as a gate electrode. INP/SNP ISFET sensors for glucose sensing have been reported [97].

The planar devices are advantageous in that they can be used for continuous monitoring using the simplicity of the electronic detection and are low-cost due to the possibility of mass production [133]. Furthermore, it can be incorporated into implantable device for possible *in-vivo* applications and lab-on-a-chip as a sensing part. A hydrogen ion-sensitive SWCNT multilayer on which GOx enzymes were immobilized using is described. The LbL assembled SWCNT multilayer showed pH-dependent conductance, which decrease exponentially with increases in pH values due to protonation /deprotonation of a SWCNT network. The pH changes induced in the process of glucose oxidation by the enzyme GOx cause the conductance changes of SWCNT multilayer, resulting in the current changes flowing through the multilayer. The LbL assembled SWCNT multilayer is proven to be versatile for sensing biochemical reactions with many other enzyme systems.multialyers.

4.1.2. Experiments

The devices were fabricated in the way that was described in Chapter 2. For glucose sensing application, three bi-layers of (PDDA/GOx) were LbL-assembled as bio-receptors. The schematic diagram of the LbL assembled SWCNTs and GOx based glucose sensor is shown in Figure 4-1. There are three different layers, $(PDDA/PSS)_2$ as a

precursor layer for the charge enhancement, $(PDDA/SWCNT)_5$ as an electrochemical transducer, and $(PDDA/GOx)_3$ as a bio-receptor.

The whole process for LbL assembly of both SWCNT transducing layers and GOx bio-receptors was monitored by quartz crystal microbalance (R-QCM, Maxtek Inc.) at room temperature. The used crystal is the AT cut 9 MHz with the active oscillation area of 0.34 cm^2. First of all, two bi-layers of (PDDA/PSS) were deposited on the 9 MHz crystal for the charge enhancement of the crystal surface, followed by 5 bi-layers of (PDDA/SWCNT) as the transducer materials. Finally, GOx was assembled on the SWCNT layer alternatively with PDDA. After every layer, thorough washing with DIH_2O was performed to prevent precipitations, which hampered uniform coating of subsequent materials, followed by a nitrogen (N_2) drying. This QCM characterization simulated the exact process of the fabrication of glucose sensors. Frequency shift after the assembly of each layer was monitored and recorded with the sampling frequency of 1.25 kHz.

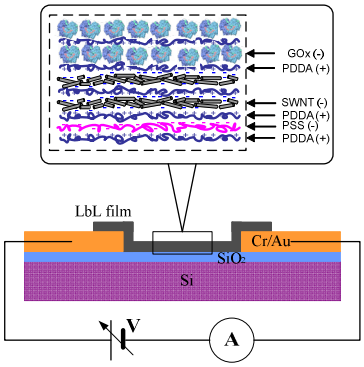

Figure 4-1 Schematic diagram of the LbL assembled SWCNT and GOx based glucose sensor along with the electronic testing scheme. Bias voltage is applied to source and drain electrodes with sample solution on top of LbL thin-film and the current is sampled.

A silicon wafer with silicon dioxide 2 μm thick was cleaned with piranha as aforementioned to remove the organic contaminants for Fourier transform infrared spectroscopy study. To demonstrate the assembly of GOx onto PDDA terminated surface, GOx was assembled with an alternative layer of PDDA after depositing two bi-

layers of (PDDA/PSS). The reflective FTIR (Nicolet Magna IR 750) spectroscopy was used to characterize PDDA, (PDDA/PSS), and $(PDDA/PSS)_2$(PDDA/GOx) surfaces with the background of the bare SiO_2 surface. FTIR spectra were obtained in the mid infrared (MIR) region, 4000-1000 cm^{-1} by an average of 500 scans with a spectral resolution of 2 cm^{-1}.

Three different kinds of devices (the ones only with GOx, the ones only with SWCNT, and the ones with both SWCNT and GOx) were prepared to show that the combination of SWCNT and GOx plays a key role of glucose sensing. Furthermore, devices were characterized using parameter analyzer at different glucose concentration on the physiological ranges (2-10 mM) as well as low concentration to evaluate the performance of the fabricated sensors. The characterized devices were stored at 4°C for 15 days and re-characterized to investigate the stability of devices.

4.1.3. Results and discussion

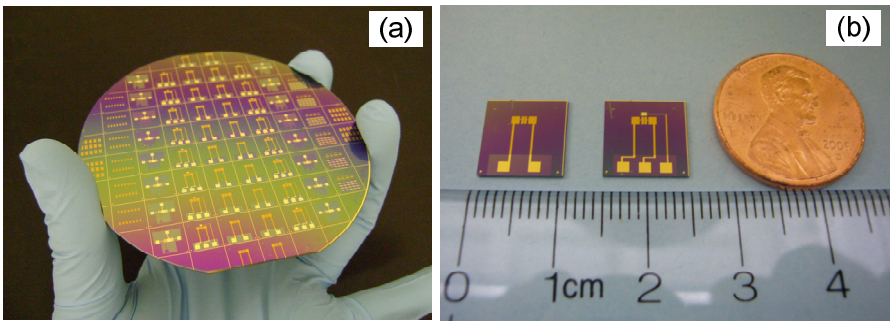

Figure 4-2 A fabricated conductometric glucose sensor: (a) standard 4 inch wafer scale fabrication and (b) individual chips

The fabricated devices on the standard 4 inch wafer and individual chips are shown in Figure 4-2, where only two terminal devices are used. To characterize the SWCNT terminated surface with scanning electron microscope (SEM, Jeol 6500), the surface of $(PDDA/PSS)_2(PDDA/SWCNT)_5$ were sputter-coated with platinum 50 Å thick. SEM images were obtained at an acceleration voltage of 10 kV as shown in Figure 4-3. The

individual SWCNTs as well as their bundles are observed and they form a random network.

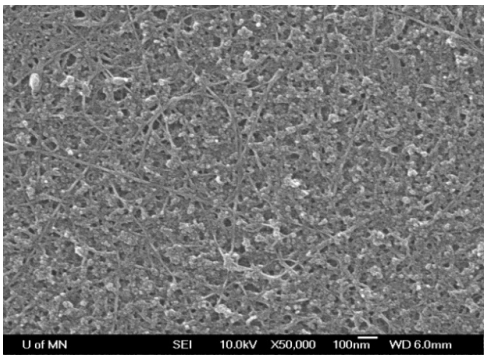

Figure 4-3 Scanning electron microscopy (SEM) image of SWCNT terminated surface: Individual SWNTs, bundles, and their random network are observed

The QCM characterization result for the whole LbL assembly process of glucose sensor is shown in Figure 4-4. It is clearly observed that the frequency decreases with the number of layers assembled as shown in Figure 4-4 (a). The reason for the abrupt frequency increase corresponding to PDDA assembly after PSS, SWCNT, and GOx is the viscosity of PDDA solution since frequency shift was collected in the solution not in the atmosphere. It assures exclusion of the effect of any moisture left after intermediate drying and contaminants adsorption from the atmosphere. The saturated frequency shifts are shown in Figure 4-4 (b). The average frequency shifts of either polycation like PDDA or polyanion such as PSS, SWCNT, and GOx reveal the mass adsorbed on the surface as Sauerbrey equation, given by

$$\Delta f = -C_f \Delta m_s$$

where Δf is the frequency shift in *Hz*, C_f the sensitivity factor of the used crystal (0.181 $Hz \cdot cm^2 \cdot ng^{-1}$ for the 9 MHz AT cut crystal), and Δm_s the mass adsorbed per unit area in ng/cm^2. This is based on the fact that the crystal is fully covered with the mass for LbL assembly [134] and sustained by fully distributed SWCNTs as shown in Figure 4-3. The average of frequency shifts for (PDDA/PSS), (PDDA/SWCNT), and (PDDA/GOx) bi-

layers is 198, 299, and 65 Hz, respectively. In particular, the frequency decrease for (PDDA/SWCNT) bi-layer is substantially consistent with the previous result [57]. The mass of assembled bi-layers, (PDDA/PSS), (PDDA/SWCNT), and (PDDA/GOx) are calculated as 83, 125, and 27 ng, respectively. In addition, the thickness for each material can be calculated with the assumed density [57]. The thicknesses for PDDA and SWCNT are 2.8 and 4.8 nm, respectively. Based on the assumed density, 1.3 g/cm^3 [135], the bio-receptor thicknesses can be calculated as 2.8 nm under assumption that linear polyelectrolyte (PDDA) fully covers GOx, so that only GOx size is dominant. The smaller film thickness than actual diameter of GOx (~ 7 nm) can be attributed to the sparse packing of GOx on the surface. From the QCM data, it is obvious that GOx is negatively charged, and can be built up multilayer alternatively with positively charged PDDA.

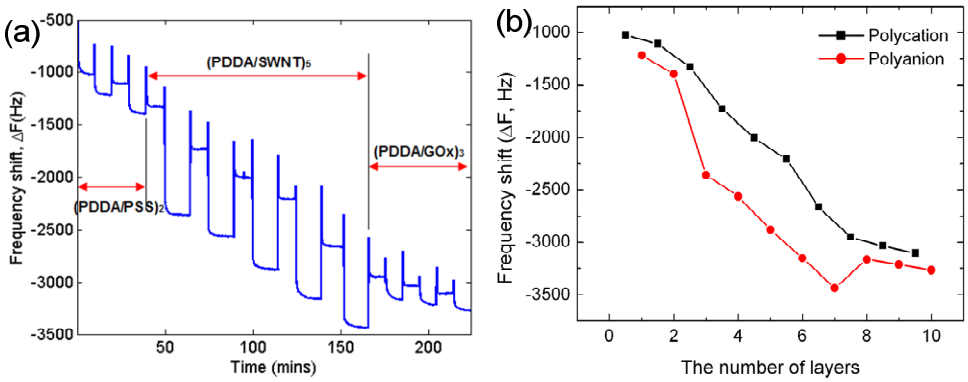

Figure 4-4 QCM study of multilayer growth process of SWCNT as an electrochemical transducer and GOx as a bio-receptor to fabricate the glucose sensors: (a) real-time monitoring of frequency decrease by adsorption and (b) the saturated frequency shift of polycation (PDDA) and polyanion (PSS, SWCNT, and GOx).

Complementary to QCM, FTIR was used to demonstrate GOx could be self-assembled onto the positively charged PDDA surfaces. The reflective FTIR spectra of PDDA, (PDDA/PSS), and $(PDDA/PSS)_2$(PDDA/GOx) are shown in Figure 4-5. Unlike the spectra of PDDA and (PDDA/PSS) control groups, the spectrum of GOx surface has several characteristic peaks. The strong absorption peak at 1664 cm^{-1} corresponds to C=O

stretching vibration (amide I band, 1700-1600cm^{-1}) of peptide bonds of GOx backbone absorbed onto PDDA surface. Another strong peak at 1520 cm^{-1} results from N-H bending vibration (amide II band, 1600-1500cm^{-1}) of peptide bonds. Both strong peaks are in good agreement with reported results [136]. These two peaks are evident indications of the presence of GOx. Moreover, the weak peak at 3320 cm^{-1} is caused by N-H stretching of the peptide backbone, and peaks ranging from 1300-1240 cm^{-1} are attributed to amide band III [137]. In consequence, the absorption peaks found in the $(PDDA/PSS)_2(PDDA/GOx)$ compared to PDDA and (PDDA/PSS) ensure that enzyme GOx is negatively charged, and can be self-assembled alternatively with positively charged PDDA. Furthermore, FTIR is proven to be a potent tool to demonstrate the protein immobilized by LbL assembly, since it has been used for determination of protein secondary structure [137].

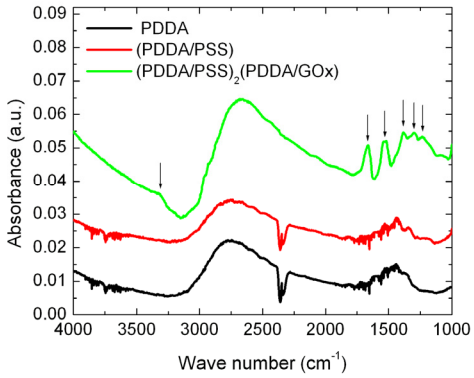

Figure 4-5 Reflective FTIR spectra of PDDA, (PDDA/PSS), and $(PDDA/PSS)_2(PDDA/GOx)$ on the silicon surfaces: Arrows indicate the presence of amide bonds in GOx

The glucose testing of LbL assembled devices is shown in Figure 4-6. All data of current versus glucose concentration were collected using the semiconductor parameter analyzer. First of all, two control groups, $(PDDA/PSS)_2(PDDA/SWCNT)_5$ and $(PDDA/PSS)_2(PDDA/GOx)_3$ has been chosen as control groups in the absence of the bio-receptor and transducer, respectively, in order to demonstrate that the combination of SWCNT and GOx shows the capabilities of glucose sensing. The currents are depicted in Figure 4-6 (a) at a bias voltage of 0.6 V. The current in $(PDDA/PSS)_2(PDDA/GOx)_3$ is

almost constant at zero compared to other two groups, indicating that other salt ions do not play a significant role of transferring electrons or holes between source and drain electrodes. On the other hand, the current in devices with only SWCNT multilayer diminishes almost linearly with the increase of glucose concentration presumably due to the adsorption of glucose molecules onto SWCNT surface or changes of the proximal ionic environment. Contrary to these, it is explicitly observed that the cooperation of SWCNT and GOx shows the augmenting current with glucose concentration.

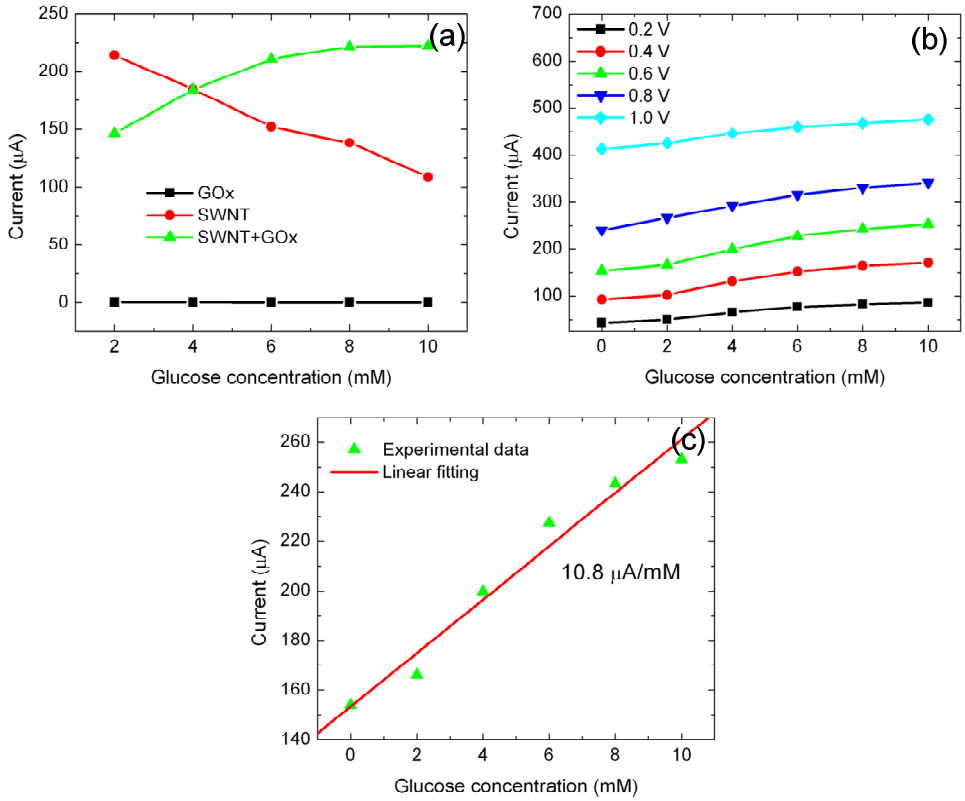

Figure 4-6 Glucose concentration test of the fabricated sensor: (a) sensing capability of the combination of SWNT and GOx multilayer, (b) current versus glucose concentration at the various bias voltages, and (c) linear curve fitting to current data at the bias voltage of 0.6 V

Based on the pH-dependent conductance changes in SWCNT multilayer, the current flowing through the multilayer is dependent on glucose concentrations. Even though pH in the bulk solution maintains relatively constant owing to the buffering power of PBS,

the local pH changes near GOx leads to protonation/deprotonation of carboxylic groups on SWCNTs causing the conductance variation. Moreover, the effect of bias voltage on the current is shown in Figure 4-6 (b). As driving voltage increases, the current increases. It is expected that the sensitivity should be constant regardless of glucose concentration at the constant bias voltage considering the exponential pH sensitivity. However, it is worthy of mentioning that the sensitivity in the glucose sensing decreases with glucose concentration as shown in Figure 4-6 (c). The decreasing sensitivity is caused by the enzyme GOx kinetics since the current corresponds to the rate of reaction in electrochemical sensors, and it is obviously enzyme limited reaction, which has been proven in QCM results. The overall sensitivity upon linear fitting has been found as 10.8 μA/mM at the bias voltage of 0.6 V. The sensitivity found in this study is remarkable compared to other planar devices reported previously [97, 138, 139] due to the highly sensitive SWCNTs.

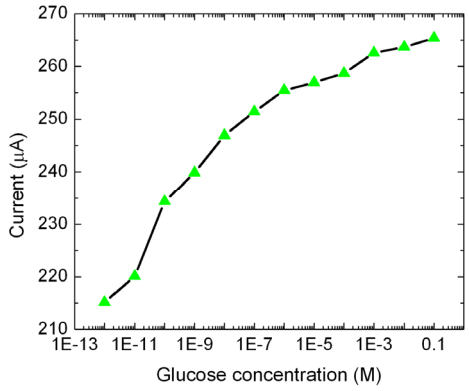

Figure 4-7 Resolution test of the fabricated glucose sensor at the bias voltage of 0.6 V

The resolution of device fabricated is shown in Figure 4-7 at the bias voltage of 0.6 V. Even though it shows a different current level and scale from the ones in Figure 4-6, which was measured in the different chip, it is observed that the device can detect down to 1 pM glucose concentration due to highly sensitive SWCNTs. In addition, the result for the stability test is shown in Figure 4-8. The device was stored at 4ºC. The decreased overall sensitivity from 9.5 to 8.6 μA/mM is observed due to decreased enzyme activity,

but the current level is increased 15 days after fabrication presumably due to surface adsorption of the atmospheric particles or surface oxidation.

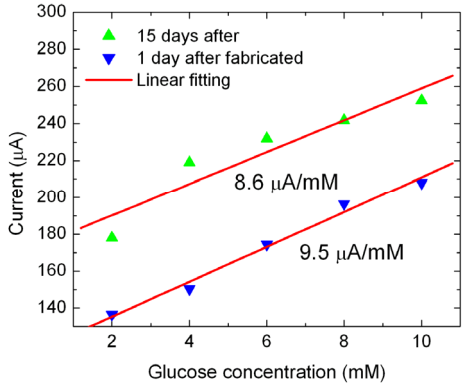

Figure 4-8 Stability test of the fabricated glucose sensor stored in dry state at 4 ºC

4.1.4. Summary

The conductometric glucose sensors has been fabricated using LbL assembled SWCNT and GOx on the silicon substrate. The GOx has been proven to be charged negatively and assembled successively using LbL technique as shown in FTIR and QCM results. LbL assembled thin-film SWCNT multilayer shows exponential pH-dependent conductance by protonation/deprotonation of carboxylic functional groups on the SWCNTs. Hydrogen ions penetrate into SWCNT multilayer and have influence on its electronic conductance. Based on conductance change caused by pH change, glucose concentration can be detected by the local pH changes, which is caused basically by the oxidation of glucose catalyzed by GOx. The overall sensitivity and the resolution of device fabricated are 10.8 μA/mM and 1 pM, respectively, at the bias voltage of 0.6 V. LbL assembled SWCNT thin-film multilayer may detects many other biochemical reactions accompanied by pH change assisted by enzymatic reactions.

4.2. Flexible SWCNTs ISFET[**]

4.2.1. Introduction

There has been much research effort to attain flexible electronics with emphasis on applications like electronic bar codes, RFID tags, smart credit cards, and flexible displays [140]. Transparency allows the multilayer packaging such that internal product information is visible, which provides the simplicity of inspection. For this reason, the assembly of nanomaterials on the flexible and transparent substrate, with the capability of selective placement or patterning of the assembled film, is getting more important in order to exploit novel properties for the emerging application of not only electronics but also nanoscale physical or chemical sensors. In this section, CNTs were integrated into ISFET sensors as a channel material by LbL assembly and lithographic patterning on the low-cost, transparent and flexible PET substrate, and pH/glucose sensing applications are demonstrated. The fabricated SWCNT-based flexible ISFET sensor has been proven to be a versatile chemical and biological sensor, which makes *in-vivo* application promising due to biocompatible nature of polymer substrate. The assembly of nanomaterials on flexible substrate via LbL bottom-up construction is cost-effective and suggests new paradigm of manufacturing process.

4.2.2. Experiments

Polyethylene terephthalate (PET) polyester flexible substrate (250 μm thick, 100 mm in diameter) was cleaned in acetone, methanol, and isopropyl alcohol for 5 minutes, respectively, in order to remove organic contaminants followed by rinsing with deionized water (DIH_2O). From metal deposition to the assembly of SWCNTs and GOx, the fabrication process of the flexible sensor is exactly same as the one described in Chapter

[**] Reprinted from Biosensors and Bioelectroncs, Vol. 25, D. Lee and T. Cui, Low-cost, transparent, and flexible single-walled carbon nanotube nanocomposite based ion-sensitive field-effect transistors for pH/glucose sensing, pp 2259–2264, Copyright 2010, with permission from Elsevier.

2 for the silicon substrate. The thin film structure used in ths topic had [$(PDDA/PSS)_3$+$(PDDA/SWCNT)_3$] and additional biomolecular multilayer of $(PDDA/GOx)_3$ for pH and glucose sensing, respectively.

The electrochemical detection of pH and glucose concentration was performed using the ISFET characterization. V_{DS} was scanned from 0 to –1.0 V with a step of -20 mV and V_G was swept from 0 to -1.5 V with a step of -0.3 V. The used sample solution was sucked and the sensor surface was washed with DIH_2O several times between measurements without repositioning of reference electrode. The time response measurement was conducted differently from ISFET characterization of pH and glucose. The conductance of the LbL SWCNT multilayer was collected using Data logging/switch system (Agilent 34970A) without the reference electrode. After the acquisition in one pH buffer, the used buffer was sucked and new pH buffer was applied without rinsing sensor surface.

4.2.3. Results and discussions

The fabricated standard 4 inch wafer level devices and diced individual chips are shown in Figure 4-9 (a) and (b), respectively. SWCNT terminated surface was characterized with field emission gun scanning electron microscope (FE-SEM, Jeol 6500). SWCNTs are selectively assembled only on the channel area which is 10 μm long and 1 mm wide, as shown in Figure 4-9 (c). The magnified SEM image of an SWCNT film on the channel is shown in Figure 4-9 (d) where random SWCNTs network is observed.

The fabrication was performed with freestanding flexible PET substrates that are identical in size to the standard 4 inch wafer without attaching it to flat wafers as described elsewhere [13, 141]. Furthermore, multiple lithographic techniques were used due to the chemical and thermal resistance of PET polymer. The fabricated flexible SWCNT ISFET in this study features the absence of the inorganic dielectric layer such as SiO_2, Si_3N_4, Al_2O_3, or Ta_2O_5, etc, which has played a role of the receptor or donor of

charge carriers in the traditional ISFET. Instead, SWCNTs play a role of inorganic dielectric layer using abundant carboxylic groups on SWCNTs surface. Therefore, variation of the surface charge induced by the shift in ionic composition directly influences the conductance of semiconducting SWCNT layers [11].

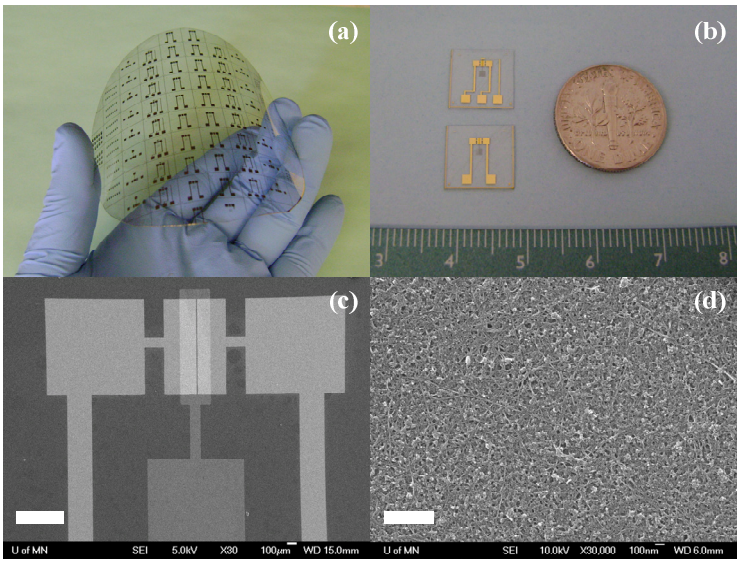

Figure 4-9 A fabricated flexible SWCNT ISFET sensor: (a) standard 4 inch wafer level devices with a demonstrative bending, (b) 1 cm × 1 cm individual chips, and SEM images of (c) microfabrcated electrodes and SWCNT pattern (scale bar: 500 μm) and (d) SWCNT film on the channel area (scale bar: 500 nm)

First of all, the flexible SWCNT ISFET pH sensor was characterized at pH 5 buffer to demonstrate a basic functionality of transistors as shown in Figure 4-10. The explicit field effect and gate transfer characteristics demonstrated that SWCNTs are p-type semiconducting materials as shown in Figure 4-10 (a). As V_G increases, the conductance of SWCNT multilayer increases, thereby yielding increasing I_D. Furthermore, the saturation effects are observed above V_G = -0.6 V below which the ionic conductor and/or Schottky contact behavior are observed above V_{DS} = -0.8 V. The effect of those was observed significantly in the SWCNTs resistors [11]. It means that the high negative gate voltage localizes positively charged ions, suppressing the ionic conducting effect. At low gate voltage, however, V_{DS} plays a dominant role of driving charged species for ionic

conductor. The linear curve fitting was performed on the range of V_G = -0.6 ~ -1.2 V in Figure 4-10 (b), where ionic conductor was suppressed, and threshold voltage (V_{th}) was found as 0.8 V based on the theory for the conventional silicon MOSFET in saturation region as follows:

$$I_{D,saturation} = \frac{wC_i\mu}{2l}(V_G - V_{th})^2$$

where C_i is the capacitance per unit area of the gate insulating layer, μ is the charge carrier mobility, w and l are the channel width and length of the channel, respectively, and V_{th} is threshold voltage. The *on/off* current ratio ($I_{on/off}$) found was 3.7. The reason for the positive V_{th}=0.8 V for p-type semiconductor and low $I_{on/off}$ =3.8 is the presence of metallic SWCNTs in the LbL assembled film, which allows current flow even though semiconducting SWCNTs are in off-state. Nevertheless, SWCNTs ISFET sensors are still useful for chemical and biological sensors, since the ion-responsive electrical signals are obtained. The gate leakage current shown in Figure 4-10 (c) was less than 1 μA under V_G = -1.5 V and V_{DS} = 0 V, which is remarkably smaller than the reported one in previous SWCNTs ISFET sensors [68], where Ag/AgCl wire without the electrolyte was used as a reference electrode. By exposing wire surface to sample solution, there might be side electrochemical reaction, which can be seen as gate leakage current that resulted in failure to providing the stable solution potential [142]. By using the internal filling solution of 3 M KCl, low gate leakage current 1,300 times smaller than I_D at the highest V_{DS} and V_G tested was obtained. For comparison, the reported one [68] was 10 times smaller than I_D at the highest V_{DS} and V_G tested.

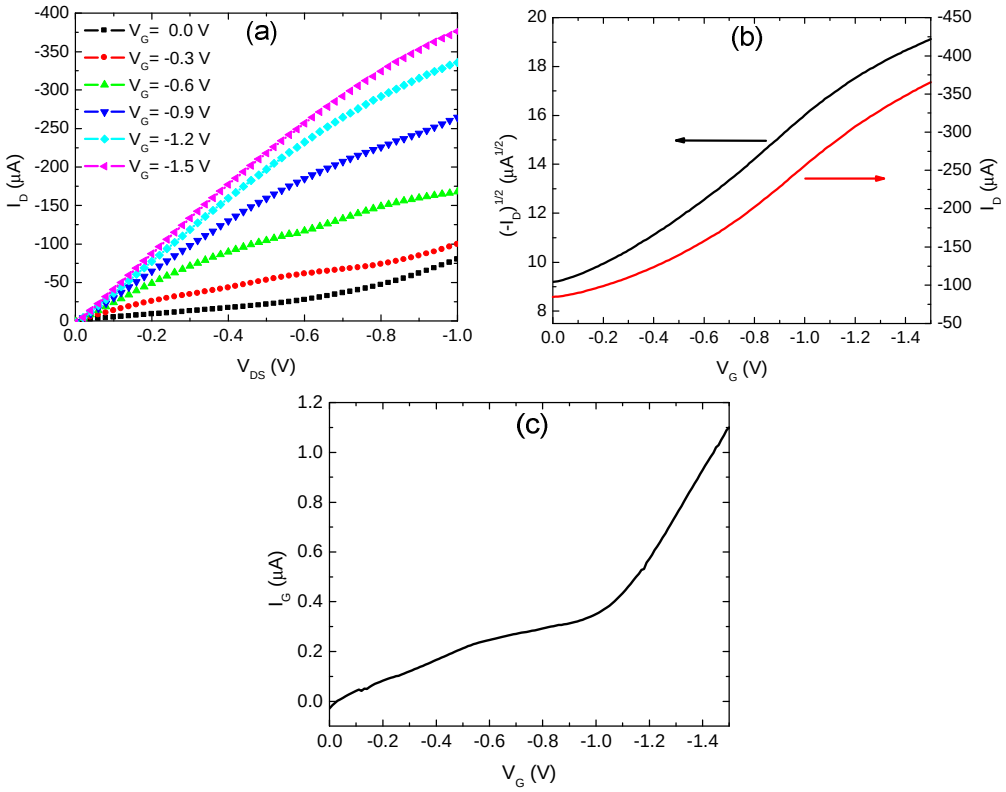

Figure 4-10 A representative basic functionality of flexile ISFETs in pH5 buffer: (a) field-effect, (b) gate transfer characteristic at fixed V_{DS} = -1.0 V, and (c) leakage current at V_{DS} = 0 V

The pH response of the fabricated flexible SWCNT ISFET sensor is also shown in Figure 4-11. It is apparently observed in Figure 4-11 (a) that a higher current flows at a lower pH at the fixed V_G = -1.5 V throughout the V_{DS} tested. In SWCNT resistors [11] where the gate electrode was not used, *I-V* was in parabolic relationship. In ISFETs, however, saturation effects are found in I_D due to the gate voltage, which localizes charged ions and suppresses the ionic current as mentioned. The I_D at the fixed V_{DS}= -1.0 V and V_G= -1.5 V were extracted and redrawn versus pH in Figure 4-11 (b). The current is exponentially dependent on pH, which indicates that molecular protonation/deprotonation plays a role of the electrical property change in SWCNTs [11]. The I_D at the fixed V_{DS}= -1.0 V and V_G= -1.5 V were normalized by the current at pH7, since current levels from devices in one batch were different due to the difference in initial conductance of SWCNT ISFETs caused by the random network of SWCNTs. 8

devices with 10 μm channel length were tested and currents were normalized. $I_D/I_{D,pH7}$ versus pH curve was shown in Figure 4-11 (b). The time response of the SWCNT multilayer conductance to pH buffers without the gate voltage applied is shown in Figure 4-11 (c). In the atmosphere where the conductance of SWCNTs is susceptible to micro-environment such as ambient air flow and wetting status, the conductance is in transition. However, once the pH buffer solution is applied, the conductance of the SWCNT multilayer decreases exponentially, followed by the stabilization with the time constant of within 1 min. This pH dependent conductance without the gate reference electrode implies that the local pH in the proximity of SWCNTs plays a role of the substitutive gate voltage which is ameliorated by external electric voltage.

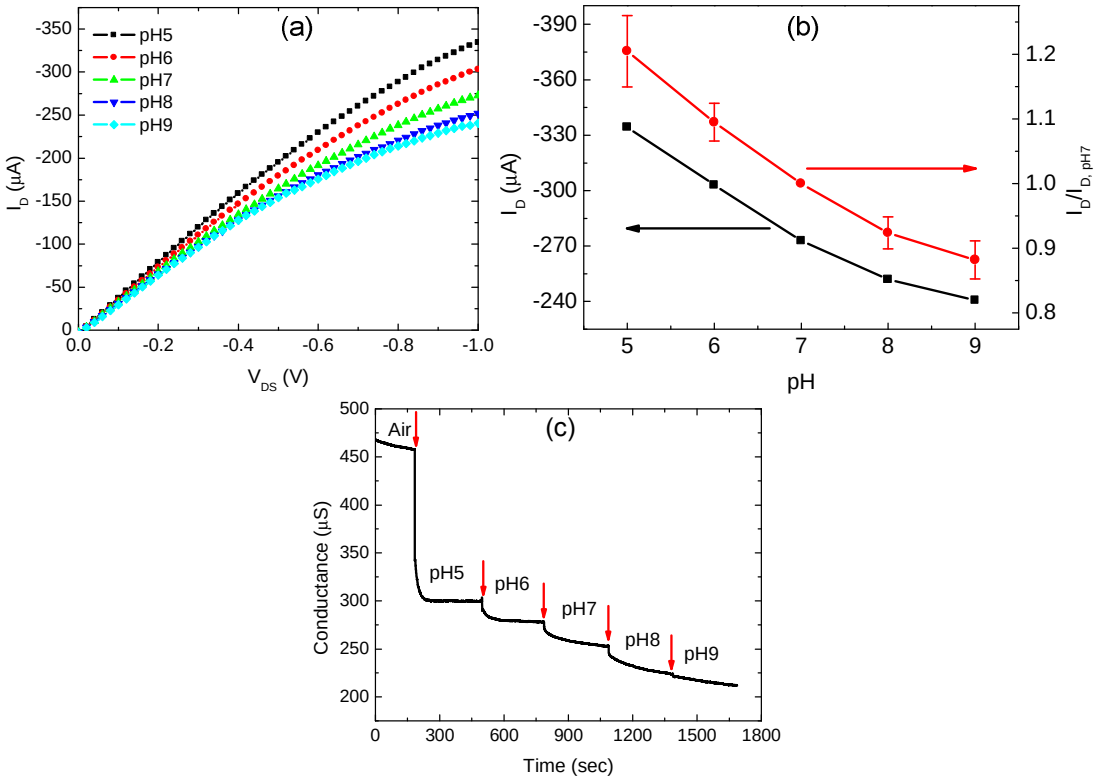

Figure 4-11 The pH response of the fabricated flexible SWCNT ISFET sensor: (a) representative drain current (I_D)-voltage (V_{DS}) curves funder different pH buffers at fixed V_G = -1.5 V, (b) pH-responsive drain current and normalized I_D by the current at pH 5 buffer from 8 devices tested at fixed V_{DS} = -1.0 V and V_G = -1.5 V, and (c) time response of the flexible SWCNT multilayer conductance to pH without gate voltage applied

The basic functionality of the flexible SWCNT ISFETs with $(PDDA/PSS)_3(PDDA/SWCNT)_3(PDDA/GOx)_3$ at 10 mM glucose concentration was tested as shown in Figure 4-12. A field-effect in Figure 4-12 (a) was also clearly observed and reveals that SWCNTs are p-type semiconducting materials. The gate transfer characteristic showed V_{th} of 1.1 V and $I_{on/off}$ of 2.7 in Figure Figure 4-12 (b), which were different from those in pH sensing at fixed V_{DS} = -1.0 V presumably due to the sample solution used and the mutation in electrochemical properties of SWCNTs by additional GOx layers. The leakage current in Figure 4-12 (c) was less than 1.6 μA over the entire V_G range tested, which was 740 times smaller than I_D at the highest V_{DS} and V_G tested.

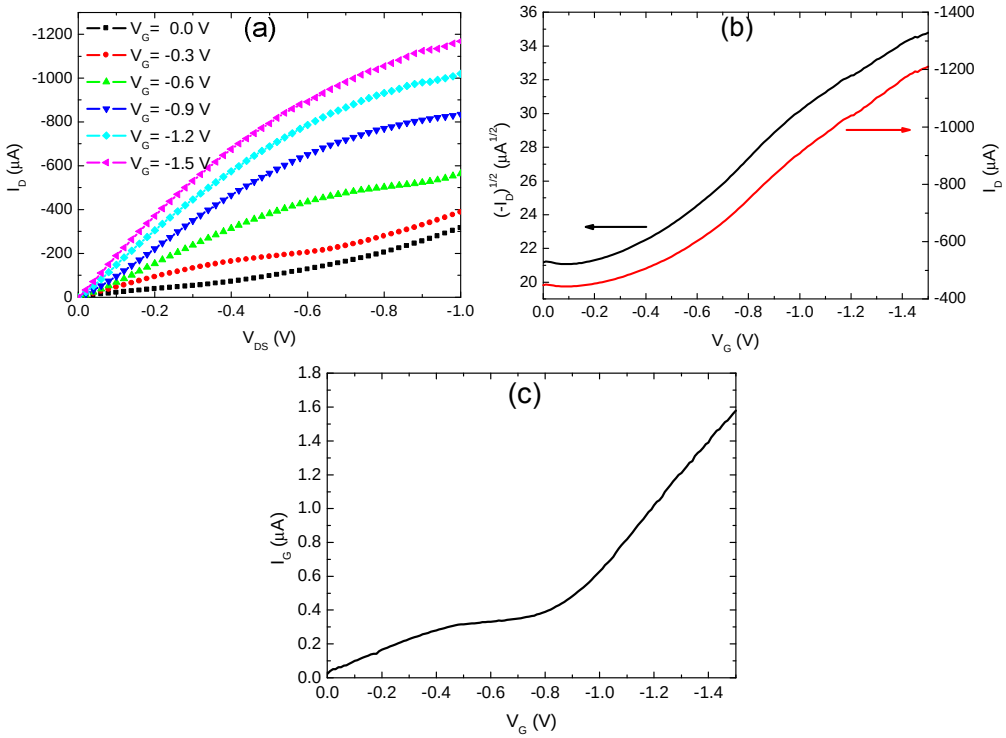

Figure 4-12 A representative basic functionality of flexible ISFETs in 10 mM glucose: (a) field effect, (b) gate transfer characteristics at fixed V_{DS} = -1.0 V, and (c) leakage current at V_{DS} = 0 V

The flexible SWCNT ISFETs were tested in various glucose concentrations. The glucose responsive flexible sensor behaviors are shown in Figure 4-13. I_D increases with increase in glucose concentration at fixed V_G = -1.5 V over the entire V_{DS} tested as shown in Figure 4-13(a). The glucose responsive I_D from one device at fixed V_{DS} = -1.0 V and

V_G = -1.5 V is depicted in Figure 4-13(b), where a sensitivity of 28.4 µA/mM was found on the linear range of 2-10 mM. 7 devices with 10 µm channel length were tested for glucose sensing, and currents were normalized with the current at the glucose concentration of 6 mM. $I_D/I_{D,6mM}$ versus glucose concentration curve was added in Figure 4-13(b). Generally, sensitivities were found as the range of 18-45 µA/mM due to the initial conductance variance of devices themselves even though all devices tested showed a linear range of 2-10 mM. This fact suggests the possibility of the physiological glucose diagnostics with the normalization scheme The sensitivities found were larger than the ones reported for planar devices [11, 97, 139].

However, it is noticeable that the saturation is clearly observable above 10 mM due to enzyme limited reactions. The reaction rate in Michaelis-Menten kinetics of the enzyme corresponds to the current flow in the electrochemical sensors, which can be considered as the hydrogen ion production rate in SWCNT ISFETs. A new reaction rate $\Delta I_D{}^*$ is defined as follow on the consideration of th normalization:

$$\Delta I_D{}^* = \frac{I_D - I_{D,PBS}}{I_{D,6mM}}$$

where $I_{D,PBS}$ is drain current at PBS and $I_{D,6mM}$ drain current at 6 mM glucose. Subsequently, Lineweaver-Burk plot is constructed as shown in Fig. 5c between $\Delta I_D{}^*$ and glucose concentration, [G] based on the following equation.

$$\frac{1}{\Delta I_D{}^*} = \frac{K_m^{app}}{\Delta I_D{}^*{}_{\max}[G]} + \frac{1}{\Delta I_D{}^*{}_{\max}}$$

where K_m^{app} is the apparent Michaelis-Menten constant, and $\Delta I_D{}^*{}_{\max}$ corresponds to the maximum rate of the reaction. The derived K_m^{app} of 14.2 mM is considerably lower than free GOx [143], and comparable to reported results for other CNT-based glucose sensors [144, 145], indicating a high affinity of LbL assembled GOx multilayer to glucose. In other words, LbL assembly of GOx on the CNT multilayer preserves the bioactivity.

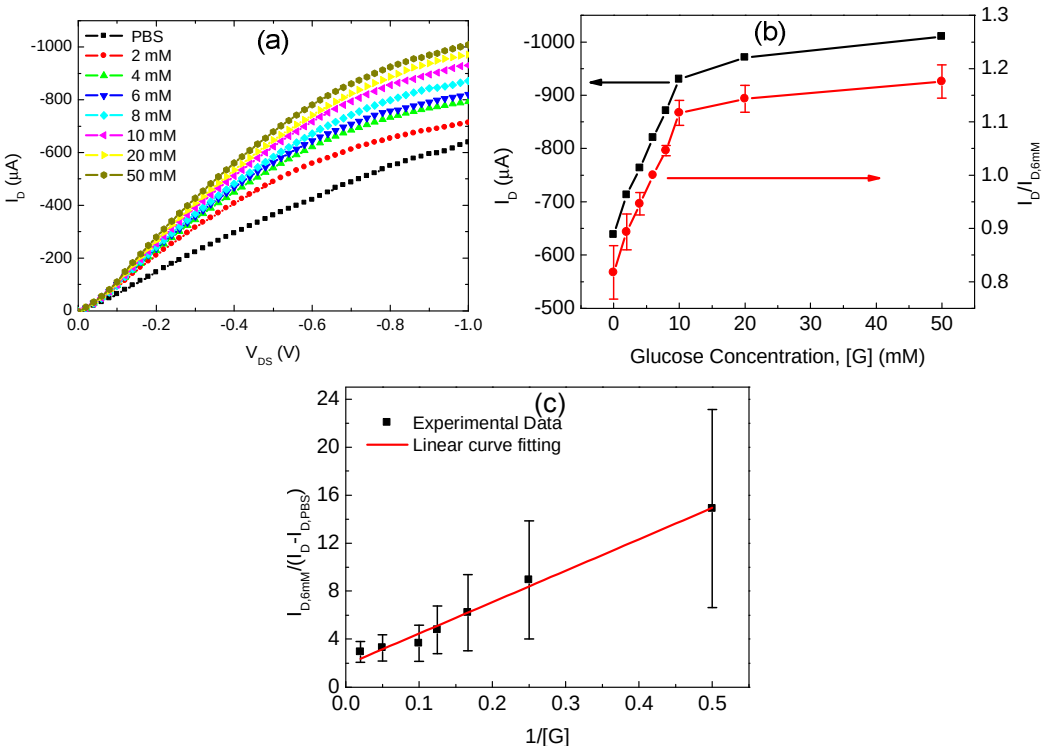

Figure 4-13 Glucose concentration test using the flexible SWCNT ISFET sensor with the layer of $(PDDA/PSS)_2(PDDA/SWCNT)_3(PDDA/GOx)_3$: (a) representative drain current (I_D)-voltage (V_{DS}) curves in different glucose concentrations at fixed V_G = -1.5 V, (b) glucose-responsive drain current (I_D) and normalized I_D by the current at 6 mM from 7 devices tested at fixed V_{DS} = -1.0 V and V_G = -1.5 V, and (f) Lineweaver-Burk plot of ΔI_D^* and glucose concentration, [G]

4.2.4. Summary

The fabrication of flexible SWCNT ISFET sensors has been investigated using all lithographic techniques with LbL bottom-up construction, which makes the final product cost-effective due to the inexpensive polymer substrate and mass production. In addition, the flexible polymer substrate is biocompatible due to the material nature, which eliminates the need of dielectric layer, and makes *in-vivo* application promising. The pH has been characterized based on the molecular protonation/deprotonation of carboxylated SWCNTs to show exponential decrease in drain current with increase in pH. Glucose has also been detected by the local pH change with the aid of bio-receptors, glucose oxidase (GOx) multilayer. The field-effects at pH 5 buffer and 10 mM glucose are significantly

observed. Although V_{th} and $I_{on/off}$ are not as high as in solid-state devices, flexible SWCNT ISFETs have been proven to be useful for chemical and biological sensors. The sensors have shown low leakage currents due to the use of the Ag/AgCl reference gate electrode, which blocks ionic movements. Generally, glucose ISFETs have a sensitivity of 18-45 μA/mM on the linear range of 2-10 mM, and follow Michaelis-Menten kinectics. The derived Michaelis-Menten was 14.2 mM, indicating a high affinity of LbL assembled GOx to glucose. The LbL assembly of nanomaterials and enzymes on the transparent and flexible substrate suggests various chemical and biological sensors suited for *in-vivo* applications.

4.3. In_2O_3/SiO_2 nanoparticle sensor array

4.3.1. Introduction

Indium oxide (In_2O_3) nanoparticles (INPs) have been used for pH [12] and neurotransmitter acetylcholine sensing [13] as the type of ion sensitive field effect transistors (ISFETs). Even though nanomaterials have excellent sensing properties, nanomaterial based sensors have disadvantages of a significant variation in electrical properties from device to device presumably due to the random network nature of nanomaterial film. However, synthesizing highly ordered nanostructures is time-consuming and involves wet chemistry in order to address this disadvantage. Instead, keeping the random network, all-nanoparticle based conductometric sensor array was fabricated in this work, and it was successfully demonstrated as a glucose biosensor with the aid of glucose oxidase (GOx) enzyme and microfluidic sample delivery system. As a result, glucose sensors were successfully demonstrated as a model biosensor array resulting in concentration dependent currents due to the electrochemical properties of nanoparticles. Glucose could be detected in many different sensing sites within a chip. And statistical analysis was performed in terms of sensitivity and the apparent Michaelis-Mention (K_m^{app}) constant depending on the channel length of resistors. The developed

sensor array has potential applications to multi-analyte detection, sensing components in a lab-on-a-chip microsystem, and bioassay platform capable of single-shot detection.

4.3.2. Experiments

The interdigitated electrodes are used in this study as shown in Figure 4-14. 16 sensor chips with the size of 15.5 mm x 15.5 mm were embedded on a 4 inch silicon wafer. Each chip contained 40 sensing sites which were accommodated within the circular microchamber with the diameter of 8 mm. The channel gaps of 5, 10, 15, and 20 μm between two interdigitated electrodes were designed in a single chip to evaluate the effect on device performance in ambient and in PBS. The number and length of fingers in a single sensing site are 5 and 400 μm, respectively, as shown in Figure 4-15 (a).

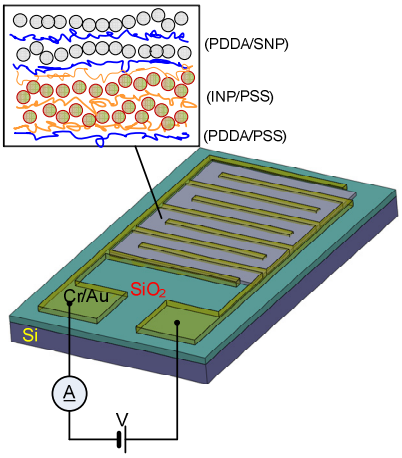

Figure 4-14 The schematic of the ion-sensitive conductometric nanoparticles resistor: an interdigitated electrode is used for the single sensing site

INPs were assembled as a semiconducting channel material alternately with the negatively charged PSS2 as done previously. Subsequently, SNPs were deposited with the pair of the positively charged PDDA as the enzyme immobilization site due to the abundant charged surface groups [146]. The dipping time for INPs and SNPs was 15 and 4 minutes, respectively. The final thin-film structure fabricated was $[(PDDA/PSS)_2 (INP/PSS2)_5 (PDDA/SNP)_6]$. After the lift-off in the acetone and the dicing into

individual chips, glucose oxidase (GOx) was assembled with PDDA in the same way as reported previously [10].

LbL assembled chips were mounted onto a 256 lead ceramic pin grid array (PGA, Global Chip Materials, LLC) and wire-bonded as shown in Figure 4-15 (b). The distribution of sensing sites and connection diagram into XTB systems (TSI Inc) are shown in Figure 4-15 (c). The sensing sites are grouped according to the channel length (5 µm: E and H; 10 µm: K and N; 15 µm: Q and T; 20 µm: W and B) to apply the bias voltage readily. The source electrodes in each group of sensing sites were connected to the common terminals that were expressed in blue rectangles in Figure 4-15 (c). The drain electrodes were connected to the electrometers in XTB system.

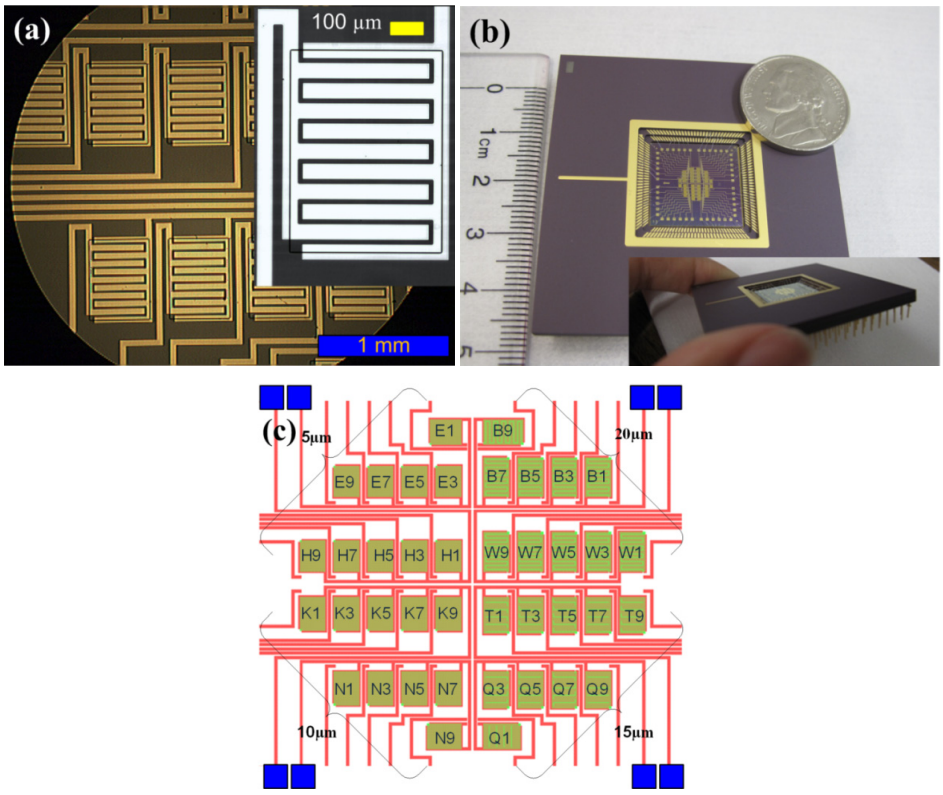

Figure 4-15 A fabricated sensor array: (a) interdigitated electrode patterns with the inset of a single sensing site, (b) a chip mounted onto ceramic pin grid array (PGA) by wire-bonding, and (c) distribution of sensing sites and connection diagram to XTB system (Rectangles represent common terminal for each letter of sensing sites)

XTB testing apparatus is demonstrated in Figure 4-16. Standard glucose solutions and washing phosphate buffered saline (PBS) were delivered automatically by syringe pumps with the rate of 100 and 500 µl/min, respectively. A multichannel electrochemical characterization was performed as follows. Firstly, the microchamber was filled with washing buffer and incubated for 5 minutes. The target glucose solutions were injected sequentially with the intermediate rinsing with PBS buffer. One concentration of glucose was fed for 2 minutes to ensure that target glucose solution filled microchamber. It was incubated for 1 minute for enzymatic reaction to occur and I-V characteristics were measured on the range of -1 to 1 V with the voltage step of 5 mV for 40 sec. The current was acquired with a sampling frequency of 10 Hz. Next, washing buffer was fed to wash out sensor surface continuously for 2 minute, and new glucose solution was delivered, followed by I-V measurements as described above.

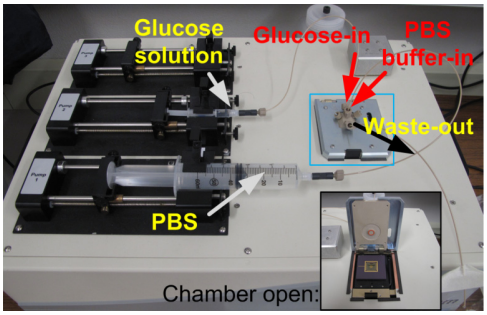

Figure 4-16 A photograph of multichannel sensing system equipped with the syringe pump driven sample delivery: Inset shows the microchamber at open position.

4.3.3. Results and discussion

The surface morphology of INP- and SNP-terminated surfaces, $(PDDA/PSS)_2(INP/PSS2)_5$ and $(PDDA/PSS)_2(INP/PSS2)_5(PDDA/SNP)_6$, was characterized with scanning electron microscopy (SEM, Jeol 6700). A 50 Å of platinum was sputter-coated and SEM images were obtained at an acceleration voltage of 5 kV. SEM images of INPs and SNPs layer are shown in Figure 4-17, where enlarged images are embedded in the inset to substantiate the particle sizes. The INP layer is composed of single nanoparticles and agglomerates whereas the SNP layer has the uniform single

particles presumably due to their own zeta potentials. The SEM of INPs validates the existence of big agglomerations which was found as the mean diameter of 255.1 nm in DSL measurement.

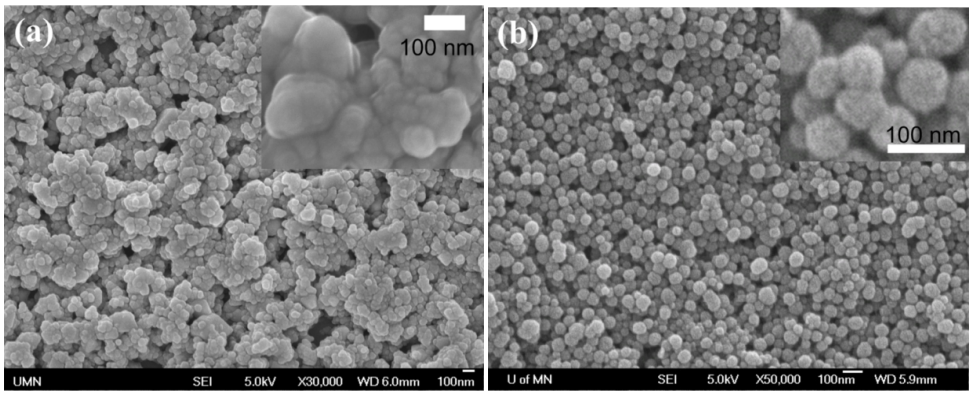

Figure 4-17 SEM images of INP and SNP terminated surface: (a) $(PDDA/PSS)_2(INP/PSS2)_5$ and (b) $(PDDA/PSS)_2(INP/PSS2)_5(PDDA/SNP)_6$

I-V characteristics of nanoparticle resistors on the range from 0 to 1 V in the ambient air and PBS are shown in Figure 4-18. Multiple curves for each channel length came from five sensing sites. I-V curves in the ambient air, as shown in Figure 4-18 (a), indicate that the nanoparticle multilayer forms Schottky contacts between nanoparticles [103] and/or between nanoparticle multilayer and metal electrodes. This is different from LbL assembled SWCNT resistor that showed the ohmic contacts [10, 11]. For the device with 5 and 10 μm channel gap, particularly, the bias voltage greater than 0.6 V is large enough to overcome the interparticle barriers [103] to allow the significant current, while it is still low for the devices with channel gaps of 15 and 20 μm. On the other hand, currents at PBS, as shown in Figure 4-18 (b), are about 30 times higher than those at atmosphere. It is also entirely different from LbL assembled SWCNT resistor [11], where the conductivity abruptly drops when sample solution was added presumably due to the swelling of multilayer film resulting in reduction of interconnection among SWCNTs. In addition, it is noticeable that I-V curves showed a diode-like behavior with a consistent transconductance to the channel length on the bias voltage larger than 0.6 V. The reason for the increasing conductance of NPs resistors in PBS comes from three aspects: (1)

reduction of contact barriers among INPs, (2) mutation of contact resistance between nanoparticle layer and metal electrodes, and (3) the formation of the conductive channel in the particles.

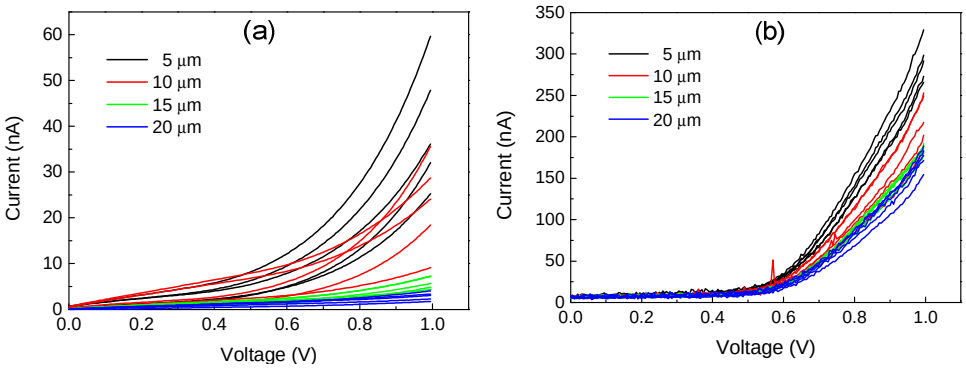

Figure 4-18 *I-V* characteristics of nanoparticle resistors: (a) in the ambient air and (b) in PBS buffers; multiple curves for each channel length come from 5 sensing sites.

An equivalent electrical circuit of nanoparticle resistor-type sensors is illustrated in Figure 4-19. The intrinsic resistance in electrolyte solution (R_E) and the electric double layer capacitance (C_{dl}) of metal electrodes are in series. In addition, they are parallel to the contact resistances (R_C) between electrodes and nanoparticle multilayer and nanoparticle film resistance (R_{ip}) including interparticle barrier. Due to the great amount of C_{dl} in the miniaturized chemoresistors [147] and use of direct current (DC) in I-V measurement, the combinative impedance through bulk solution is assumed to be huge and constant, whereas R_C and R_{npf} are sensitive to their microenvironment. Therefore, the electronic conduction corresponding to analytes concentration occurs preferentially through the nanoparticle film rather than bulk sample solution. The monitoring of R_{npf} is key role in nanomaterial sensors because of their high surface-to-volume ratio and ability to make tremendous contacts. Specifically, the sensing current greatly increased in biosensors with the enzymatic layer, which produces new charged ions continuously under the assumption of enough substrates.

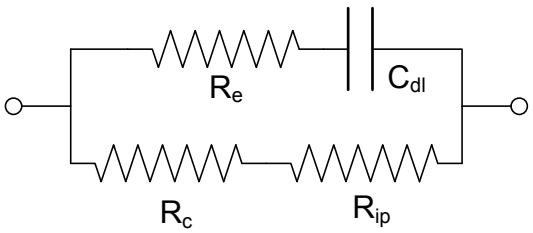

Figure 4-19 An equivalent electric circuit of nanoparticle resistor: Miniaturized sensor array and the application of DC voltage give rise to C_{dl} drastically so that analyte dependent currents are obtained through nanoparticle layer rather than bulk sample solution.

Time responses of each channel length to increasing glucose concentrations at the bias voltage of 0.7 V are shown in Figure 4-20. One glucose concentration was fed for a period of time and another concentration of glucose was injected without intermediate washing during the application of bias voltage. Even though output currents were sometimes unstable presumably due to the fluidic instability, increasing output currents were observed with increasing glucose concentration. The products in GOx enzymatic reaction, especially hydrogen ions, play an important role in protonation of surface hydroxyl groups leading to the effect of positive surface charge. More positive surface charge enhances more conductive channel inside n-type INPs [12].

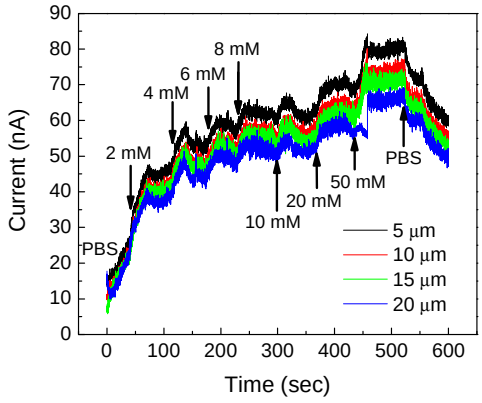

Figure 4-20 Time response curves from one sensing site per channel length at bias voltage of 0.7 V

Even though discernible I-V curves were not found at the low bias voltage that is not enough to overcome interparticle barriers, I-V curves on the range from 0.9 to 1.0 V at

various concentration of glucose are consistent as illustrated in Figure 4-21 (a) from one 10 μm channel sensing site. The concentration dependent currents are observed at higher bias voltage. The currents (I) at the bias voltage of 1.0 V at various glucose concentrations were extracted and normalized with the one in PBS. Normalized currents (I^*) are shown in Figure 4-21 (b) as a function of glucose concentration at different channel lengths. Although the current level is different from site to site within a channel length, saturation effects are observed in normalized currents (I^*) presumably due to the enzyme kinetics. Furthermore, decreasing normalized currents are observed with increasing channel length, while devices with 20 μm channel gap showed higher current than the ones with 5 and 10 μm channel gap. To evaluate enzyme kinetics, Lineweaver-Berk plot was constructed as shown in Figure 4-21 (c), demonstrating the average K_m^{app} value of about 20 mM for the sensing sites with 5, 10, and 15 μm and 17.7 mM for the ones with 20 μm.

The testing results are summarized in Table 4-1. The sensitivity found was different depending on the channel length, which showed decreasing with increasing channel length. On the other hand, it is noticeable to observe constant K_m^{app} at about 20 mM, which was thought to be the characteristics of immobilized GOx enzymes onto nanoparticles. The differences in the number of sensing sites considered are originated from the failure of wire-bonding. It is interesting to see different behaviors in the device with 20 μm channel length, an increased sensitivity and reduced K_m^{app}. The extracted K_m^{app} are smaller than the free GOx enzyme but larger than LbL assembled GOx on SWCNTs. It is noticeable that K_m^{app} is different depending on the immobilization site due to the steric effect.

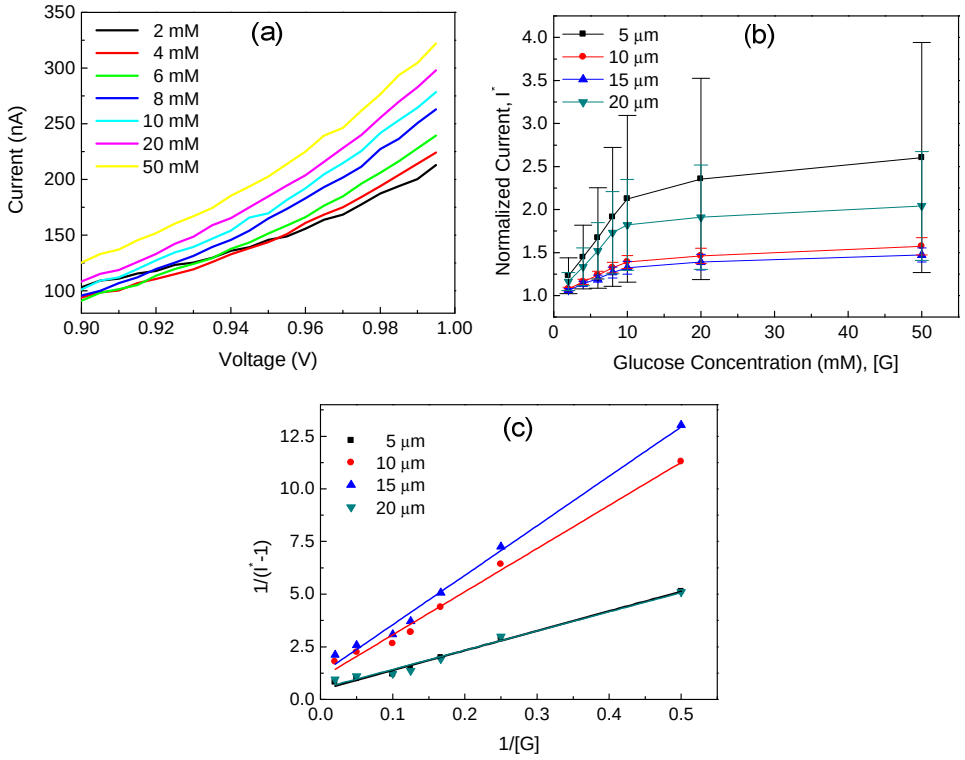

Figure 4-21 Glucose sensing results of nanoparticle resistor array: (a) I-V curves on the range from 0.9 to 1.0 V at various glucose concentrations extracted from one 10 µm channel device, (b) normalized currents with respect to the current in PBS at the bias voltage of 1.0 V versus glucose concentration, and (c) Lineweaver-Burke plots of normalized current, I^* and glucose concentration, [G]

Table 4-1 Summary of multichannel sensor testing

Channel length (µm)	# of devices considered	Sensitivity (nA/mM)		K_m^{app} (mM)
		Mean	Standard deviation	
5	10	11.9	3.9	20.3
10	8	5.7	2.6	20.1
15	7	4.4	1.5	19.6
20	7	6.9	2.9	17.7

4.3.4. Summary

An enzymatic nanoparticle biosensor array has been fabricated uinsg INPs and SNPs and demonstrated successfully as a conductometric glucose biosensor. The NP resistor showed different I-V characteristics at the ambient air and aqueous PBS environment presumably due to the charge carrier transfer mechanism. Glucose was successfully detected in most sensing sites within a chip with a single-shot of sample delivery. The current dependent on glucose concentration was normalized, averaged, and analyzed, and sensor array was evaluated statistically in terms of sensitivity and K_m^{app}. The sensor array showed showed a linear response on the physiological range of glucose, yielding a sensitivity of 4-12 nA/mM and the apparent Mechaelis-Menton constant of 20 mM. The developed nanoparticle conductometric sensor array has potential applications of multiplexed sensors, various bioassay platforms and sensing part in the lab-on-a-chip.

4.4. Sensing mechanism and sensor evaluation

A variety of glucose sensors have been demonstrated in this chapter in terms of materials, structures, the type of subrates and characterization methods. The sensing mechanism in each type is discussed and compared. To access the performance of each type, in addition, sensitivity and apparent Michaelis-Menten constant are compared and discussed.

The glucose breakdown reaction with the aid of GOx enzyme is generally described as follows:

$$\beta - D - glucose + O_2 \xrightarrow{GOx} D - glucono - \delta - lactone + H_2O_2$$
$$D - glucono - \delta - lactone + H_2O \rightarrow D - gluconate^- + H^+$$
$$H_2O_2 \xrightarrow{+0.7V} O_2 + 2H^+ + 2e^-$$

β-D-glucose is oxidized to D-glucono-δ-lactone with the catalysis reaction of GOx, followed by the hydrolysis of D-glucono-δ-lactone and the electrooxidation of H_2O_2 under applied gate potential to produce hydrogen ions as well as electrons. The

comprehensive glucose sensing mechanism in nanomaterial-based glucose sensors is illustrated in Figure 4-22 in case transducing nanomaterial is SWCNT. In conductometric sensors, the first two equations are applied, so that one hydrogen ion is produced per glucose molecule. However, two more hydrogen ions as well as two electrons are generated with the aid of the gate voltage applied through Ag/AgCl reference electrode. The produed hydrogen ions penetrate into nanomaterial layer and protonation/deprotonation reactions occur in nanomaterial transducers as well as SNP dielectric layer, resulting in pH-dependent conductance behavior. Consequently, it is natural that a higher sensitivity is observed in ISFET sensing scheme. In addition, flexible polymer substrate may influence the bioactivity of immobilized enzyme, thereby affecting the sensitivity. Furthermore, the exponential pH-dependent conductance behavior is applied to develop glucose sensors aiming at linear response on physiological glucose concentration as discussed in chapter 3. It is evident that the exponential dependence of I or I_D in conductometric and ISFET sensors, respectively, on pH results in linear dependence on glucose due to a log scale nature of pH [11] at the low concentration of glucose.

The electrical conductance change in SWCNTs can be caused by: (1) the proximal ionic composition change, (2) direct molecular protonation/deprotoation, and (3) direct electron transfer in ISFETs. The local pH change in the vicinity of SWCNTs and the direct electron transfer play the role of drain current change in the SWCNTs layer. Particularly, the concentration of hydrogen ions produced from glucose breakdown is maintained constant in the vicinity of GOx layer from which ions diffuse away to reach SWCNT transducer layer or disappear towards the bulk solution due to the buffering power of the sample solution. Therefore, the ionic composition in the proximity of SWCNTs results in pH changes, thereby the conductance change of SWCNTs. On the other hand, the direct electron transfer might take place from glucose directly to SWCNT surface. The transferred electrons flow through SWCNT layer and contribute to the drain current.

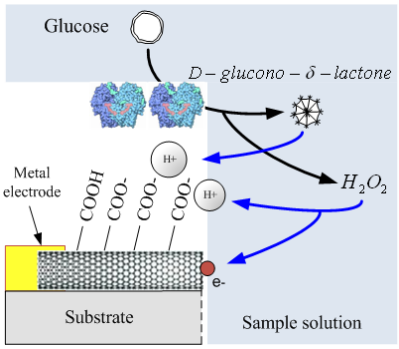

Figure 4-22 A suggested comprehensive glucose sensing mechanism in case of sensing material of SWCNT

Biosensors are highly dependent on enzyme activity. Especially, enzyme kinetics can be considered as an important factor for evaluating enzymatic biosensors, since immobilized enzymes show a different activity from free ones. The saturation in current is generally observed as the concentration of glucose increases due to the limiatation of enzyme reaction, which is described as Michaelis-Menten kinetics. The reaction rate corresponds to the current in electrochemical enzymatic sensors. Therefore, the apparent Michaelis-Menton constant (K_m^{app}) is extracted from the Lineweaver–Burk plot to access the enzyme activity. Smaller values in K_m^{app} indicate a higher affinity of GOx to glucose. However, the sensor output becomes nonlinear above K_m^{app}, which is not desirable to the implementation of glucose sensors. Consequently, it is important to have K_m^{app} values slightly higher than physiological glucose concentration for the point-of-care diagnostic. The sensitivity and K_m^{app} values found in each type sensor developed in this chapter are summarized in Table 4-2.

The sensing performance of the developed glucose sensors is compared with the reported planar devices or CNT based condcutormetric sensors as shown in Table 4-3. As a result, the SWCNT thin film sensors demonstrated a higher sensitivity and an appropriate detection range targeted for physiological blood glucose sensing. Though the response time is a bit longer than some devices, it is still on the reasonable range for the application of domestic glucose monitoring and rapid diagnosis.

Table 4-2 Comparison of glucose biosensors studied in terms of sensitivity and Michaelis-Menton constant of GOx enzyme

Sensor type	Sensitivity (μA/mM)	Michaelis-Menten constant (mM)	Note (channel, μm)
SWCNT conductometric	10.8	2.1	10
Flexible SWCNT ISFET	18-45	14.2	10
INP/SNP conductometric	0.004-0.012	20	5,10, and 15

Table 4-3 Performance comparison of the developed nanomaterial electrochemical glucose sensor with the reported ones

Materail and sensor type	Sensitivity (μA/mM)	Detection range (mM)	Response time	Source
SWCNT conductometric	10.8	0-10	1 min	This work
Flexible SWCNT ISFET	18-45	0-10	3 min	This work
INP/SNP conductometric	0.004-0.012	0-10	< 1 min	This work
Prussian Blue	1.4	0.025-1	20 min	[133]
INP/SNP ISFET	2.13	2-10	15 sec	[97]
γ-APTES[††]/Nafion/PDMS[‡‡]	0.02	0-35	5 sec	[138]
Individual CNT conductometric	N/A	N/A	30 sec	[125]
Conducting polymer ISFET	0.006	0-10	0.2 sec	[148]

[††] γ-aminopropyltriethoxysilane

[‡‡] polydimethylsiloxane

5. Nanomaterial immunosensors

It is important to detect specific proteins since they are the primary actors within the cell carrying out the physiological and/or biochemical functions specified by the information encoded in genes: catalysis of chemical reactions, cell signaling and ligand binding, and structural elements, etc. Particularly, immunosensors are analytical devices to yield the measurable signals that are sensitive and selective to the specific proteins by means of the antigen-antibody interactions. It plays a role of the direct monitoring of molecular recognition event and the diagnosis of pathogenesis. A variety of immunosensors have been developed using different transducers that exploit changes in mass [149], heat [150], electrochemical [151-153], or optical properties [154-156].

It is desirable to optimize the sensitivity and detection limit of the immunosensors. Each protein has its own 'normal' reference range inside the body. For example, prostate-specific antigen (PSA), a secreted cancer biomarker, has the normal serum level ng/ml [157]. In case of interleukin-6 (IL-6), an oral cancer marker, the normal concentration is nearly 1000-fold lower than PSA leading to the detection challenge [158]. In addition, bioentities used for performing bioassay such as antibodies, antigens, enzymes, and fluorescence labels are expensive. Analytes such as blood or serum from a neonate and the spinal fluid are precious commodity and in small amount. Moreover, traditional methods such as enzyme-linked immunosorbent assay (ELISA), radioimmunoassay, and electrophoretic immunoassay require the sophisticated bench-top instrumentation and tedious and time-consuming sample preparation. Hence, the novel, simple, sensitive, reliable, and inexpensive diagnostic method is highly desired along with miniaturization without affecting their sensitivity or detection limit.

With the advent of nanomaterials, biosensors based on nanomaterials have attracted much attention due to inexpensive nanomaterials as the off-the-shelf building blocks, miniaturized device for a smaller sample volume, and excellent transducing properties. Even though nanomaterials have extraordinary properties, they themselves do not possess

the direct biomolecular recognition ability. Therefore, nanomaterial immunosensors have been developed in the form of field-effect transistors (FETs) and amperometric-type sensors. Of the various transduction mechanisms, the electrochemical transduction is advantageous since it combines the features of fast, sensitive, inexpensive, and miniaturizable measurement systems with the elegant immunoassay procedures. Furthermore, the excellent pH-sensitive electrochemical properties found in nanomaterial multilayers augment the application of nanomaterial multilayer to immunosensors.

In this chapter, immunoglobulin G (IgG) and swine influenza virus (SIV) immunosensors are demonstrated using INP/SNP dual structure and SWCNT multilayer, respectively. ELISA-based immunosensors can be miniaturized and fabricated using intrinsic electrochemical properties as a transduction mechanism studied in chapter 3. The facile electronic detection of sandwiched ELISA structures is implemented using electrochemical properties of INP/SNP multilayer structures. The conventional ELISA assay is conducted on the novel platform of nanomaterials, and electric signals are generated in response to the concentration of targen antigen using labeled detecting antibodies. The labeled detecting antiby catalyzes the reaction by which pH of substrate solution changes. The assay demonstrates the detection limit of 0.04 ng/ml of normal IgG whose molecular weight is 155kD.

Next, the LbL assembled SWCNT resistors are employed to detect novel H1N1 swine influenza viruses (SIVs) using excellent electronic properties. The resistance of immunochips tends to increase upon the surface adsorption of macromolecules such as poly-L-lysine, anti-SIV antibodies, and SIVs in the process of immunoassay. The resistance shift in the event of SIV immunobinding onto anti-SIV is normalized with the resistance of bare devices. The sensor specificity tests are performed with non-SIVs, showing the normalized resistance shift of 15 % as a background. The detection limit of 180 SIVs $TCID_{50}$/ml is obtained, suggesting a potential application point-of-care detection or monitoring systems.

5.1. In_2O_3/SiO_2 immuno-ISFET

5.1.1. Introduction

Immunoglobulin G (IgG) is one of the most abundant proteins with the typical concentration of 4-16 mg/ml in adult human serum and plasma sample. They play the role of the defense system against microorganisms and are produced by B lymphocytes. The IgG molecule has two separate functions; binding to the pathogen and recruiting other cells and molecules to destroy the antigen. The acquired immunodeficiency disorders usually result from use of drug or prolonged serious disorder such as cancer. It impairs the immune system's ability to fight with foreign or abnormal cells such as bacteria, viruses, fungi, and cancer cells, so that unusual bacterial, viral, or fungal infections or rare cancers may develop.

Despite the excellent sensitivity of clinical methods such as ELISA, fluorescent and chemiluminescent immunoassays, their application is limited by the necessity of expensive equipment and laborious sample preparation for point-of-care detection or monitoring system. One of alternative techniques is to detect immunological reactions electrochemically, which can be enabled by the presence of electroactive substance such as metal ions [159]. Quantum dot labeled electrochemical immunosensors demonstrated the detection range of 0.1-10 ng/ml and detection limit of 30 pg/ml IgG using voltametric response [160]. And gold nanoparticle was used as protein immobilization sites for aflatoxin B_1 (AFB_1) immunosensors [161]. Zirconia nanoparticles and quantum dots (ZnS@CdS, QDs) were used for construction of a biomarker of organophosphate (OP) pesticides, phosphorylated acetylcholinesterase [162]. However, the nanoparticles have been used as immobilization sites or labels to detect immnoreaction or catalyte electrochemical reaction.

The pH sensitive electrochemical properties of INP/SNP stimulate the development of electrochemical immunosensors without using electroactive metal ions. In this work, INPs are active transducing elements that convert chemical information to electrical

signal, while SNPs play a role of ELISA strucgture immobilization sites. The biomolecules used here are goat anti-rabbit IgG, normal rabbit IgG, and HRP conjugated anti-rabbit IgG as capturing antibody, antigen, and detecting antibody, repectively. Therefore, the secondary antibody was used to produce immunoreactions with primary antibody, normal rabbit IgG. The developed sensor can be utilized to detect IgGs using secondary antibody or pathogens with primary antibody that is specifit to such pathogens.

The catalytic cycle of HRP has been widely known, and a variety of substrate system was studied using conventional ISFET systems [163]. The oxidation of ascorbic acid (AA) leads to the formation of dehydroascorbic acid (DAA), which gives pH increase. However, it is known that the total rate of ascorbic acid oxidation by HRP was not high enough to detect. Instead, with the aid of o-phenylenediamine (OPD) as an electron mediator, the rate of the reaction and total pH shift increased significantly [163] as shown in Figure 5-1. INP/SNP FETs were used to detect the pH increase caused by the substrate oxidation. This work features in 3 aspects: (1) exploitation of developed all-nanoparticle ISFET sensors for ELISA immunoassay, (2) HRP catalyzed substrate-substrate activation for accelerated and enhanced pH shift, and (3) a simple ISFET characterization for pH shift. The IgG sensors developed in this study showed the detection limit of 0.04 ng/ml, which amounts to 0.26 pM and 1.56×10^8 IgGs/ml.

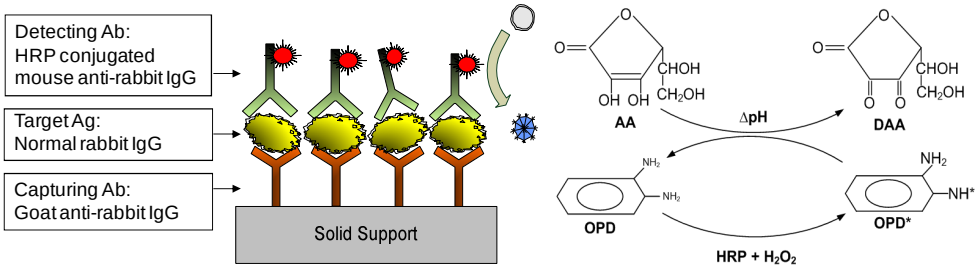

Figure 5-1 Immuno-sensing principle in pH-sensitive nanoparticle sensors: the structure of immunosensors employing sandwiched ELISA bioreceptor and the catalytic reaction of HRP for ascorbic acid (AA) and o-phenylenediamine (OPD)

The unique electrochemical properties of self-assembled semiconducting INP and dielectric SNP dual structures have been exploited. The self-assembled NPs thin film

platform employs the sandwiched ELISA structures as a bioreceptor as shown in Figure 5-1 (a). The capturing antibody (c-Ab) was immobilized on the outmost SNP layer treated with poly-L-lysine, and IgG was assembled onto c-Ab by the immuno-reaction. The detecting antibody (d-Ab) conjugated with horse radish peroxidase (HRP) enzyme was used in order to produce the pH change that is detectable in INP/SNP dual structure as studied in Chapter 3. The pH change corresponds to the amount of d-Ab labeled with HRP that is, in turn, dependent on the amount of IgG adsorbed by means of the immuno-binding. Thus, the concentration of IgG in a sample can be traced by measuring the pH change. We used the secondary antibody as capturing and detecting antibody (c-Ab and d-Ab), and the primary antibody as an antigen (Ag) for the demonstration of device functionality.

5.1.2. Experiments

Goat anti-rabbit IgG F(ab')$_2$ and normal rabbit IgG were purchased from Santa Cruz Biotechnology, Inc. Mouse anti-rabbit IgG conjugated with horse radish peroxidase (HRP) was from Chemicon Inc. Goat anti-rabbit IgG labeled with Alexa Fluor® 488 were purchased from Invitrogen Corporation. All antibodies were diluted into 1X phosphate buffered saline (PBS, GIPCO) or 3% BSA in PBS to yield an appropriate concentration. Goat anti-rabbit IgG F(ab')$_2$ was diluted 500-fold in PBS producing a concentration of 0.8 μg/ml as a c-Ab. Normal rabbit IgG, as a model antigen, was diluted to 3% BSA in PBS to yield serial concentrations of 0.04, 0.4, 4, 40, and 400 ng/ml. Mouse anti-rabbit IgG-HRP was diluted 2000-fold resulting in a concentration of 0.4 μg/ml. Ascorbic acid (AA) and o-phenylenediamine (OPD) were purchased from Sigma-Aldrich Inc in order to formulate a substrate solution for HRP catalyzed reaction. Bovine serum albumin (BSA) blocking buffers (Fraction V Solution 7.5%, Invitrogen) was diluted to produce 3 % concentration in 1X PBS.

After patterning of metal electrode, 200 cycles of aluminum oxide (Al_2O_3) was deposited using atomic layer deposition (ALD, Savannah, Cambridge NanoTech) as

described previously to protect the device from the sample solution during immunoassay. With patterned layer of photoresist, the opening window was made on the elongated measuring pads and the sensing channel as a result of etching in 10:1 buffered oxide etch (BOE). The following procedure was the same as used prviously. NPs were LbL assembled in a sequence of $[(PDDA, 10 min)/(PSS, 10 min)]_3$ + $[(INP, 15 min)/(PSS, 10 min)]_5$ + [(PDDA, 10 min)/(PSS, 10 min)] + $[(PDDA, 10 min)/(SNP, 4 min)]_6$. Finally, the silicon wafer was dipped into 0.1 wt% of PLL for an hour and lifted off using acetone, methanol and IPA, followed by rinsing with DIH_2O.

The fluorescence microscopy (FM) was used to study the PLL assembly onto outmost silica nanoparticles and the immobilization of the capturing antibody (c-Ab). For PLL assembly study, the aqueous solution of PLL labeled with FAM fluorophore (PLL-FAM, kindly provided by Professor Taton, Department of Chemistry, University of Minnesota) was used to optimize assembly time of PLL for c-Ab immobilization. Glass cover slips were treated with piranha solution (H_2SO_4: H_2O_2 3:1) at 80 °C for 20 minutes, followed by thorough washing with copious amount of DIH_2O. Three layers of $(PDDA/SNP)_6$ were LbL assembled on the glass cover slips. Then they were incubated in 0.01 wt% aqueous PLL-FAM solution for 10, 30, 60, and 180 minutes. The control was incubated in DIH_2O for 180 minutes. Fluorescent images were obtained using fluorescence microscope (Nikon, Eclipse TE200) with the blue excitation and green detecting filter at the same gain and exposure time. Fluorescence microscopy was also used in order to demonstrate the immobilization of capturing antibody (c-Ab) as shown in Figure 5-2. To verify the binding of c-Ab on the PLL terminated surface, photoresist was patterned onto the glass slide (1 cm × 1 cm). O_2 plasma was applied to change surface hydrophilic. The patterned glass slide was incubated in 0.1 wt% PLL aqueous solution for an hour. Goat anti-rabbit IgG conjugated with Alexa 488 fluorophore was assembled on the slide overnight in a concentration of 1 µg/ml (2000-fold dilution) at 4 °C. Finally, photoresist was lifted off using acetone, methanol, and IPA followed by the rinsing with PBS.

Fluorescence images were obtained before and after lift-off of photoresist to compare the green intensity at the same gain and exposure time.

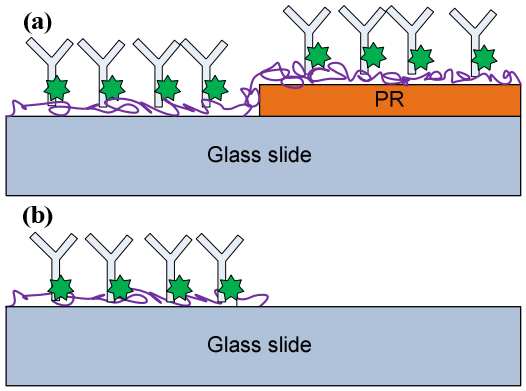

Figure 5-2 A scheme of detecting the capturing antibody immobilization: goat anti-rabbit IgG conjugated with Alexa-488 fluorophore was immobilized on the photoresist (PR) patterned glass slide (a) and PR pattern was lifted off (b)

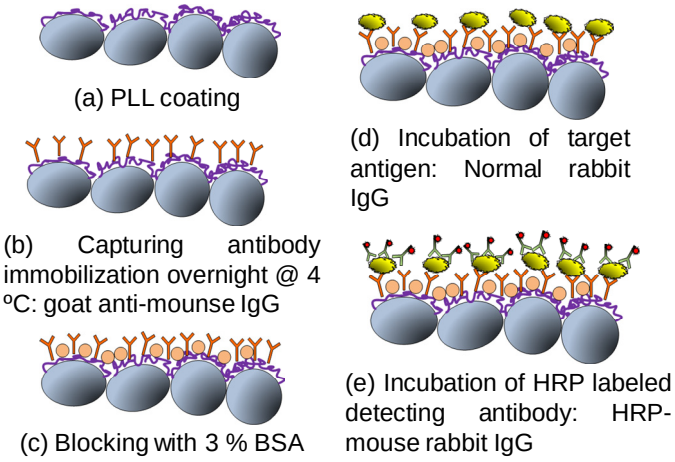

Figure 5-3 ELISA immunoassay on the surface of SNPs: The large surface-to-volume ratio can be fully exploited for antibody immobilization

The diced individual immnochips were sorted into 24-well microliter plates for the immunoassay. The immunoassay adopted in this study is schematized in Figure 5-3 with the solid support of SNPs and detailed as follows:

a. Incubate immunochips in goat anti-rabbit IgG solution with the concentration of 0.8 μg/ml overnight at 4 ºC
b. Rinse chips with 1× PBS 3 times using the shaker for 5 minutes each time
c. Incubate chips in 3 % BSA blocking buffers at room temperature for 3 hours to prevent the nonspecific binding, followed by rinsing as in step b
d. Incubate chips in normal rabbit IgG solution with various concentration of 0.04, 0.4, 4, 40, 400 ng/ml for 1 hour, followed by rinsing as in step b
e. Incubate chips in HRP conjugated mouse anti-rabbit IgG with the concentration of 0.4 μg/ml for an hour, followed by rinsing as in step b

The silicon wafer (1 in by 1 in) was treated in piranha solution (H_2SO_4: H_2O_2 3:1) at 120 °C for 20 minutes. The nanoparticle multilayer of [$(PDDA/PSS)_3$ + $(INP/PSS)_5$ + $(PDDA/SNP)_6$] was assembled. Silicon substrate was incubated in 0.1 wt% PLL aqueous solution for 1 hour. The static water contact angles were obtained using Contact Angle System (OCA-15, dataPhysics Corp) on 12 spots and averaged. The sessile contact angle was determined by placing a drop of water (5 μl) with a speed of 1 μl/sec on the surface and recording the angle between the horizontal plane and the tangent to the drop at the point of contact with the substrate. After each step of ELISA, (1) PLL coating, (2) c-Ab immobilization, (3) target IgG binding, and (4) d-Ab binding, the water contact angles were measured. The procedure for the contact angle study followed the aforementioned immunoassay procedure.

The substrate solution for the HRP catalyzed reaction was formulated as follows. The phosphate buffer at pH 6 with buffer strength of 5 mM was prepared along with 15 mM NaCl. And AA and OPD were added to yield a concentration of 1 mM, respectively. The substrate solution was used right after the formulation. Hydrogen peroxide (H_2O_2) with a concentration of 0.3 % was mixed with AA+OPD solution with a volume proportion of

1:30. 300 µl of the substrate solution was applied on the sensor surface and incubated for 5 minutes. The FET characterization scheme is applied through semiconductor parameter analyzer (HP4156B). Instead of using a series of field-effect tests, V_{DS} was fixed at 1.0 V and V_G was scanned from 0 to -5 V with a step of 50 mV for all imunochips prepared with various IgG concentration.

5.1.3. Results and discussions

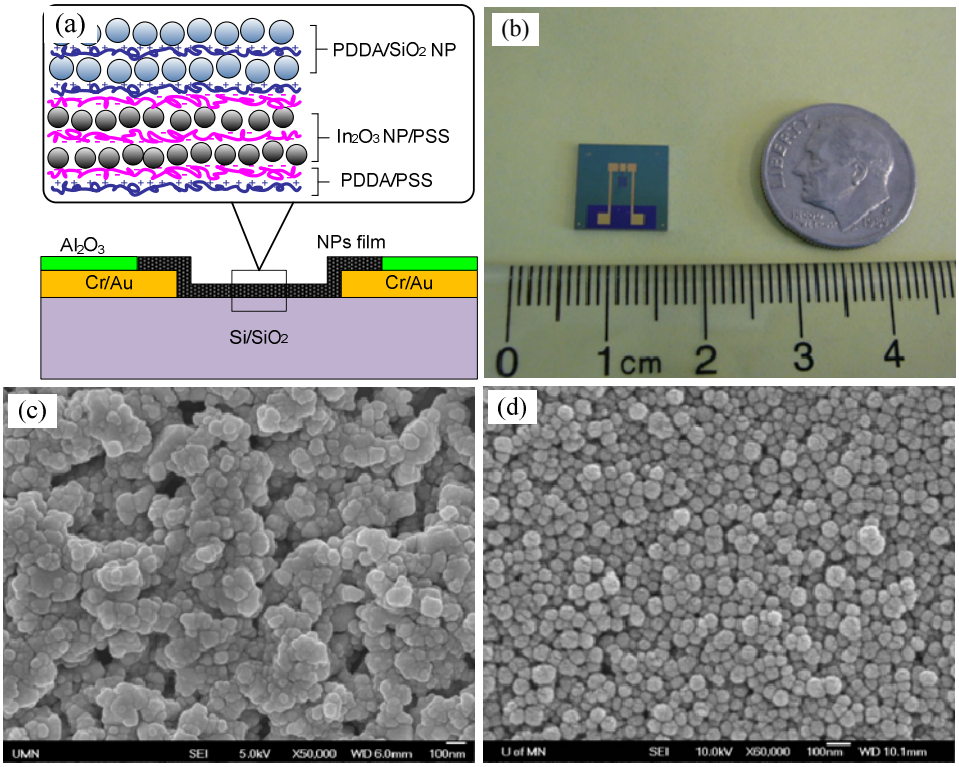

Figure 5-4 Fabricated immunosensors: (a) thin film architecture, (b) an individual device, (c) In_2O_3 nanoparticle terminated surface, and (d) silica nanoparticle surface for the enzyme immobilization

The fabricated immunochips are shown in Figure 5-4. The schematic internal structure of nanoparticle film and protective Al_2O_3 in areas other than channel for the passivation of biomolecular adsorption and electrochemical reaction are shown in Figure 5-4 (a), and NPs film was deposited only on the channel. The immunochips used for IgG sensor in this study is in the size of 1 cm × 1 cm, as shown in Figure 5-4 (b), with the channel

dimension of 10 μm legnth and 1 mm width. The SEM images of INP- and SNP-terminated surface are shown in Figure 5-4 (d). They are similar to the ones obtained in chapter 3.

FM images of glass cover slips are shown in Figure 5-5 (a) – (e) with different dipping time of 0, 10, 30, 60, and 180 minutes. The control sample is considered as 0 minute incubation time. Apparently, the green intensity increases with the dipping time, and it looks saturated at the dipping time of 60 minutes. No green signal was found in the control sample, which was dipped in DIH_2O for 3 hours. The green pixel values were extracted and averaged over the whole image. The averaged green pixel values over the image are illustrated in Figure 5-5 (f) as a function of the dipping time. It is obvious that the green intensity increases linearly and becomes saturated at the incubation time of 60 minutes.

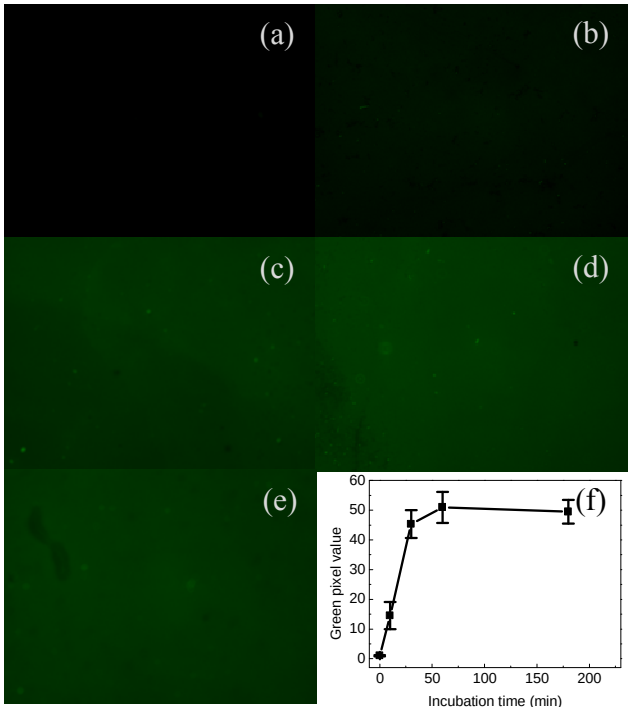

Figure 5-5 Fluorescent image of PLL-FAM covered glass cover slip at various incubation time: The saturation time of 60 minutes was observed: (a) control sample dipped into DIH_2O for 3 hrs, the sample incubated in 0.01 wt% PLL-FAM for 10 (b), 30 (c), 60 (d), 180 minutes (e), and green pixel values (f) extracted the images from (a)-(e)

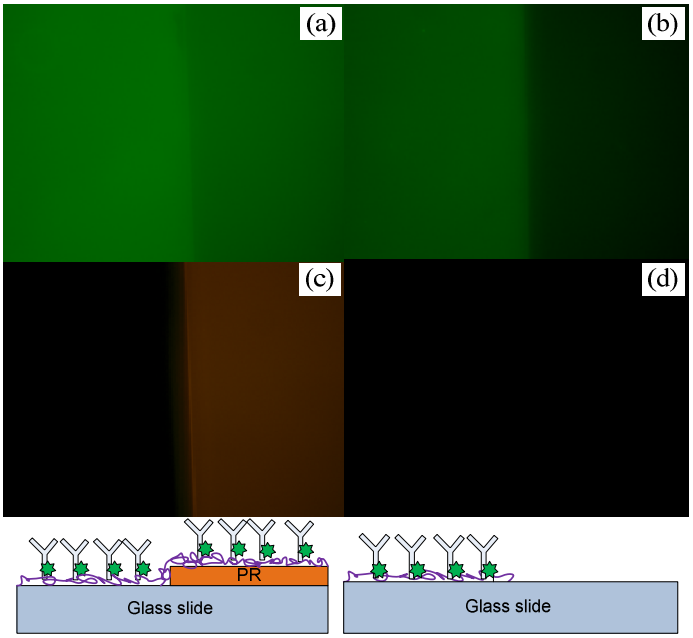

Figure 5-6 Fluorescence images of immobilized goat anti-rabbit IgG labeled with Alexa 488 on patterned glass slides for c-Ab immobilization test: (a) and (c) were obtained in the presence of photoresist with green and red detecting filter, respectively. (b) and (d) were taken after lift-off of photoresist with green and red detecting filter, respectively.

The FM images of the immobilized goat anti-rabbit IgG labeled with Alexa 488 are illustrated in Figure 5-6. The left column images, Figure 5-6 (a) and (c), were obtained with the photoresist pattern as shown in schematic below. The image (a) and (c) used the blue and green excitation and green and red detecting filters, respectively. On the other hand, the right column images, Figure 5-6 (b) and (d), were taken after the lift-off of the photoresist. The same combination of excitation and detecting filters were used as (a) and (c). It is apparent to observe green light all over the surface in Figure 5-6 (a), since c-Ab was immobililized on the photoresist as well as glass surface. Once the photoresist was removed the green light became dark resulting in the contrast image of (b), meaning that c-Ab is removed from the photoresist surface while they are still remained on the glass surface. It seemed the the red component in image (c) originated from the existence of photoresist that was disappeared in (d). Therefore, image (c) and (d) confirm that

photoresist was entirely removed from the surface. It is concluded that the capturing antibodies are successfully immobilized on the PLL treated glass surface.

Complementary to FM study, the static water contact angle was measured to readily verify the changes on the surface. If there are any changes in the surface energy from chemical [164] and topographical changes [165] on the surface, the water contact angle changes . The result of the static contact angle measurement is shown in Figure 5-7. The sessile water drop images at the surface of PLL (1), goat anti-rabbit IgG (2), normal rabbit IgG (3) bound in the concentration of 40 ng/ml concentration, and HRP labeled mouse anti-rabbit IgG (4) are illustrated in Figure 5-7 (a). The corresponding contact angles are depicted in Figure 5-7 (b), where decrease in CA upon c-Ab immobilization and gradual increase upon Ag and d-Ab binding. The contact angle measurement is a good tool to characterize immobilized proteins [166].

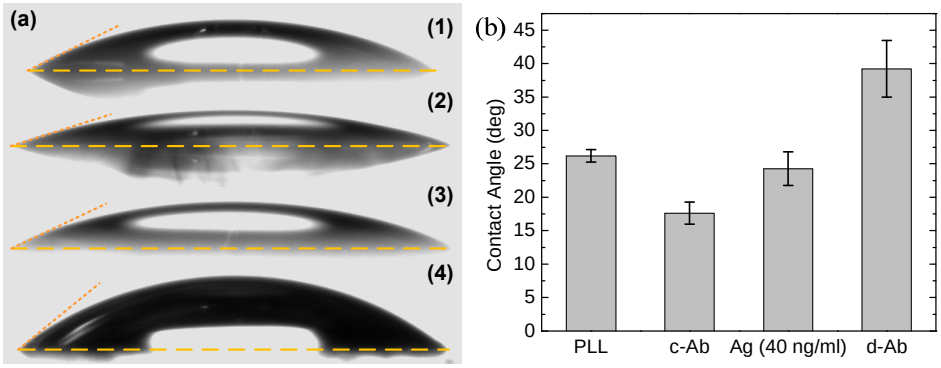

Figure 5-7 Static water contact angle measurement: (a) sessile water drop images at the surface of PLL (1), goat anti-rabbit IgG (2), normal rabbit IgG (3) in case of 40 ng/ml concentration used, and HRP labeled mouse anti-rabbit IgG (4) and (b) contact angle measurement at each step of ELISA

The result of ISFET characterization of immunochips prepared at various IgG concentrations is shown in Figure 5-8. As the gate voltage increases negatively, the conductance of the channel also increases resulting in more current. The immunochips with ELISA structures made at various IgG concentrations were tested, so that the

amount of IgG assembled determined the amount of d-Ab as a kind of signal amplification scheme. More HRP catalyzes the breakdown of more ascorbic acid resulting in greater pH increase. pH sensitivity found in INP/SNP dual structures tells us decreasing conductivity with pH increase [12]. The currents were replotted at the gate voltage of -5.0, -4.0, and -3.0 as shown in Figure 5-8 (b). It is noticeable that the linear response to pH in acidic region enables to obtain the linear response per decade from which the sensitivity of 0.87 μA/decade is extracted in case of V_G= -5.0 V, which is promising in the immunosensor development. The dotted lines represent background signal at the corresponding gate voltage applied, so that the limit of detection of electronic immunoassay using nanoparticles was found as 0.04 ng/ml, which corresponds to 0.26 pM and 1.56×10^8 IgGs/ml.

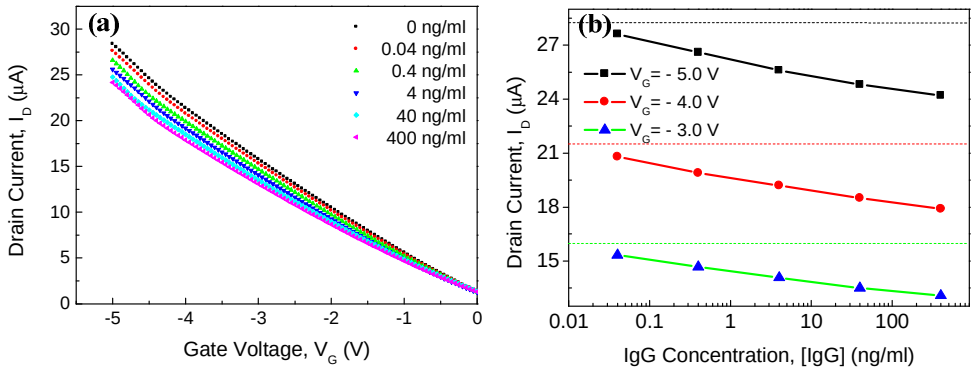

Figure 5-8 Electronic detection of IgG concentration using ISFET characterization scheme: (a) drain current versus gate voltage and (b) drain currents at various concentration of IgG

5.1.4. Summary

The INP/SNP thin film has been used as a platform for ELISA immunoassay for the electronic detection using the electrochemical properties of nanoparticles. The antibodies were immobilized effectively as indicated in fluorescence microscopy presumably due to the biocompatibility and size similarity. It is not necessary to use bench-top instruments to acquire observable signals. Furthermore it can be more miniaturized and combined with microfluidic systems to perform the elegant analytical assays. The detecting antibody labeled with HRP exploited the chain reaction between ascorbic acid and o-

phenylenediamine to accelerate and amplify pH change, which could be detected by underlying nanoparticle thin film. As a target model antigen, normal IgG was detected with the limit of detection of 0.04 ng/ml. Such nanomaterial-based platforms suggest the novel and delicate analytical devices eliminating the sophisticated bench-top instrumentation and tedious sample preparation.

5.2. SWCNT swine influenza virus sensors

5.2.1. Introduction

The novel H1N1 swine influenza virus (SIV) has spread worldwide and has resulted in 135,000 cases and 816 deaths by mid-2009 [167]. The swine influenza is an acute respiratory disease of pig and is transmissible to human causing a high fever, lethargy, nasal discharge, coughing, and dyspnea [168]. The pandemic influenza A (H1N1) is transmitted from person to person by the exposure to infected secretions from coughing or sneezing, which results in the public health issue due to the epidemic spread. Even in case of pathogens irrelevant to a human health, the large economic damage stimulates the necessity of an improved diagnosis and monitoring capability. However, the conventional methods including virus isolation assay, polymerase chain reaction (PCR), and enzyme-linked immunosorbent assay (ELISA) require extensive sample handlings, significant inclusion of laboratory resources, and long sample-to-answer time [169]. The reverse transcriptase-PCR assays have been demonstrated the highest resolution (<0.1 $TCID_{50}$/ml) [170] ever known for the detection of swine influenza. Despite the high resolution, RT-PCR assay craved expensive bench-top equipments, long assay time, and trained personnel. Consequently, it is desirable to develop rapid point-of-care detection systems for the appropriate control of such viruses.

The carbon nanotubes (CNTs) are one of the most promising materials for the rapid detection of human and animal pathogens [171] due to their excellent properties. The CNTs as nanoscale building blocks for sensors enable a better biotic-abiotic interface due

to the size similarity. The immobilized biomolecules preserves their bioactivities such as enzymatic reactions and recognition functions [171]. Furthermore, sensing platforms exploiting the nanomaterials can be miniaturized to realize an autonomous one-shot sample-to-answer bioassay via a sensing array incorporated into micro/nanofluidic systems. In addition, the unique electrochemical transduction functions found previously [10, 11] sustain the application of CNTs to biosensing toward the label-free electronic detection. The electronic detection of viruses using CNTs has the potential to revolutionalize traditional laboratory assays for the pathogen detection. However, the manipulation of individual CNTs for the construction of nanosensors is not easy due to their extreme small size. Instead, CNTs network has been used for biosensors in this work, exploiting a facile manipulation in solution phase and a robust LbL self-assembly.

Herein, self-assembled CNTs random network thin film is prepared for the electrical detection of swine influenza (H1N1) virus (SIV). The resistance shifts upon the virus binding on anti-SIV antibody are normalized with the resistance of bare devices, which extends the detection range with decreasing the channel length of SWCNT resistors. The SWCNTs networks are able to successfully detect as low as 180 SIVs $TCID_{50}/ml$ using normalized resistance shift upon the immunobinding of viruses on SWCNTs. The sensor specificity has been shown against non-SIV viruses e.g., transmissible gastroenteritis virus (TGEV) and feline calicivirus (FCV). This facile CNT-based immnoassay has potential applications as a point-of-care test or a platform for lab-on-a-chip.

5.2.2. Experiments

Poly-L-lysine (PLL, 0.1 wt%, Sigma-Aldrich) was used to immobilize the anti-SIV antibody on the surface of SWCNTs. Bovine serum albumin (BSA) blocking buffers (Fraction V Solution 7.5%, Invitrogen Corp.) was diluted to produce 3 % concentration in 1× PBS (KCl: 2.67 mM, KH_2PO_4: 1.47 mM, NaCl: 137.93 mM, Na_2HPO_4•7H2O: 8.06 mM). The anti-SIV antibody was obtained from USDA NVSL (National Veterinary Services Laboratory, Ames, IA). The hemagglutination test was conducted following the

protocol developed by NVSL, and titer was found as 1:1280. The SIV strain used in this study was obtained from the archives of Virology Lab, Minnesota Veterinary Diagnostic Lab (MVDL), University of Minnesota, St. Paul, MN. The stock virus was prepared by collecting the supernatant culture fluid from 75-100% infected Madin-Darby canine kidney (MDCK) cells. The cells were disrupted by freeze-thaw cycle (repeated thrice) and cell debris was removed by centrifugation at 2,000g for 10 minutes at 40 °C. The supernatant was removed, aliquoted (1 ml each in cryovials), and stored at -80 °C until the day of use. The undiluted virus stock was diluted using 3% BAS in PBS to produce appropriate dilutions.

The SWCNT multilayer thin film was assembled between microfabricated electrodes as a resistor as previously [11]. The silicon wafer was diced using wafer cutting system (Disco DAD 2H/6T). The individual chips had a channel width of 1 mm and variable lengths of 10, 20, or 50 µm.

The resistances of the chips were measured using digital multimeter and recorded before the assay. Individual chips were sorted depending on the channel length into 24-well plate for the assay. The immunoassay was performed as follows. The chips were incubated in 0.3 ml of 0.1 wt% PLL. After the incubation of 1 hour, PLL was removed and 0.5 ml of distilled water was added to all devices, which were placed on the shaker for 2 min followed by the removal of water. The rinsing process was repeated two times more, followed by the drying with nitrogen stream. The resistances of devices were measured and recorded. Next, 0.5 mL of 1:100 anti-SIV antibody diluted in 1× PBS was added and incubated at 4 ºC for 24 hours. The devices were washed in PBS 3 times and in distilled water 3 times, followed by drying with N_2 flow and the measurement of resistances. 0.5 mL of 3% BSA in PBS was added to prevent nonspecific binding. After the incubation of 3 hours at room temperature, 3% BSA/PBS was removed. Then the devices were washed in PBS and distilled water as done previously, and resistances were measured after drying. The devices were incubated in 0.3 ml of various virus dilutions of SIV, TGEV, and FCV in 3% BSA/PBS and 3 % BSA/PBS as a control and incubated for

1 hour, followed by rinsing, drying, and resistance measurement. The resistance shifts upon the virus binding were normalized in three different ways: (a) with the resistances of bare devices, (b) with the resistances after PLL assembly, and (c) with the resistances after anti-SIV antibody binding. The resistance shifts were normalized as follows:

$$\Delta R_x^* = \frac{R_{virus} - R_{Ab}}{R_x}$$

where *x* can be chip, PLL, or antibody meaning the resistances of bare devices, after PLL and antibody assembly. The device structure including antibody-virus complex is illustrated in Figure 5-9.

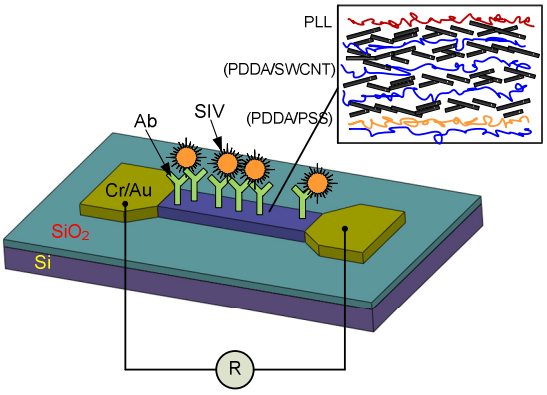

Figure 5-9 The schematic of an individual immunochip with close-up hierarchy of SWCNT multilayer thin-film

The propagation and titration [172] of FCV, TGEV, and SIV were done in Crandell Rees Feline Kidney (CRFK), Scheduled Tribes (ST), and Madin-Darby Canine Kidney (MDCK) cells, respectively. In order to determine the virus titer, serial 10-fold dilutions of each virus sample were made in Minimal Eagle Media (MEM). These dilutions were used to inoculate monolayer of corresponding cells grown in 96-well plates. After the inoculation plates were incubated at 37 ºC for 96 hours, the plates were observed for cytopathic effects (CPE) and virus titer was calculated by Karber Method.

5.2.3. Results and discussion

The fabricated device is shown in Figure 5-10. The diced individual immunochip is in size of 1 cm × 1cm as shown in Figure 5-10 (a). The SWCNT multilayer was patterned only on the channel area as shown in Figure 5-10 (b). The SEM image of SWCNT film in Figure 5-10 (c) was taken at an acceleration voltage of 5 kV (Jeol 6700) with the platinum coating of 30 Å. It demonstrates the random network of SWCNTs, which plays the role of transducer upon the SIV binding. The immnochips were sorted into 24-well plates as shown in Figure 5-10 (d) in order to conduct immunoassay.

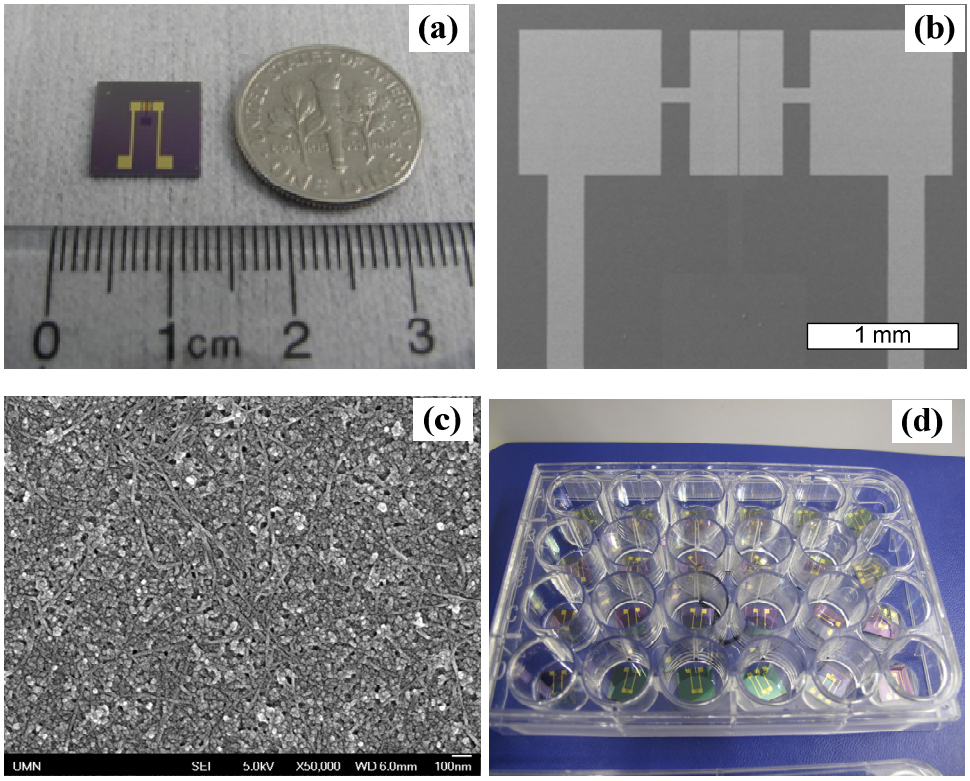

Figure 5-10 The fabricated device: (a) an optical picture of the individual chip, SEM images of metal (Cr/Au) electrode pattern (c) and SWCNTs multilayer thin film on channel area (c), and (d) sorted immunochips in 24-well microliter plate for immunoassay

The titer results are summarized in Table 5-1. The one per 100 µl is in the unit of antilog scale of virus particles, which is converted to the actual number concentration of virus particles. The titer for serial 10-fold dilutions of each virus sample showed the

considerably good linear relationship with dilutions as shown in Figure 5-11. As a result, undiluted FCV, TGEV, and SIV samples had the number concentration of 3.16×10^7, 5.62×10^5, and 1.77×10^5 virus particles/ml, respectively.

Table 5-1 The result of the titration for serial 10-fold dilutions of FCV, TGEV, and SIV stock sample

Virus	Dilution	Titer	
		Per 100 µl (antilog)	Per 1ml (particles)
FCV	Undiluted	6.5	3.16×10^7
	1:10	5.5	3.16×10^6
	1:100	4.25	1.77×10^5
	1:1000	2.75	5.62×10^3
	1:10,000	2.0	1×10^3
TGEV	Undiluted	4.75	5.62×10^5
	1:10	3.75	5.62×10^4
	1:100	3	1×10^4
	1:1000	2.25	1.77×10^3
	1:10,000	1.25	1.77×10^2
SIV H1N1	Undiluted	4.25	1.77×10^5
	1:10	3.25	1.77×10^4
	1:100	2.5	3.16×10^3
	1:1000	1.25	1.77×10^2
	1:10,000	0.5	3.16×10^1

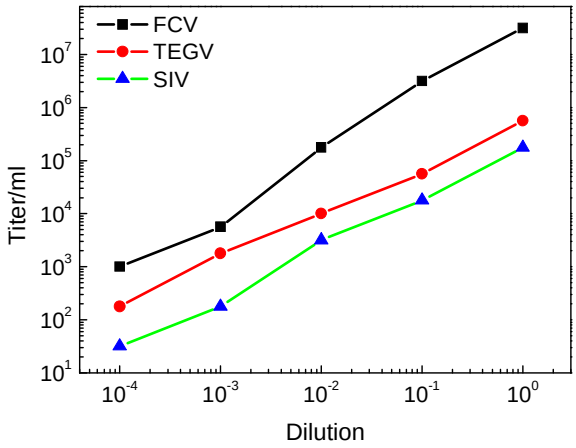

Figure 5-11 Titer for serial 10-fold dilutions of FCV, TGEV, and SIV samples

The measured resistances of bare, PLL coated, and anti-SIV antibody assembled chips are shown in Figure 5-12. The resistance tends to increase upon the surface adsorption of PLL and anti-SIV antibody, suggesting the resistance changes after the immunobinding of SIVs presumably due to their charge carrier donating/accepting properties and/or huge structure compared to CNTs and antibodies. The physical adsorption of viruses influences the electrical properties of CNTs, which, in general, increases the resistivity of CNTs film. Depending on the virus type, however, charge carriers on the conducting channel of SWCNTs may be enhanced or reduced in case of the charge carrier donating or accepting species, respectively. Furthermore, it is observed that the resistance keeps increasing in 10 μm channels, while it becomes saturated a bit in 20 and 50 μm channels.

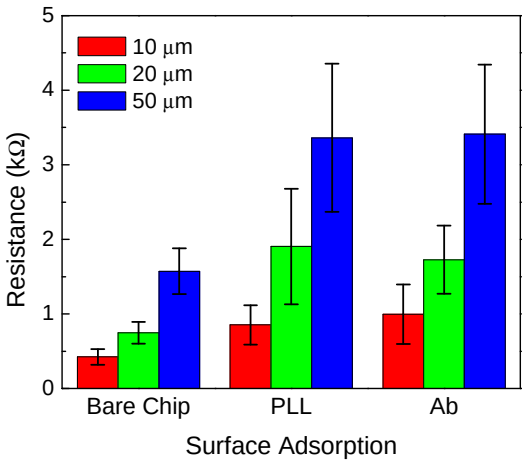

Figure 5-12 The effect of surface adsorption on the resistance of chips on the channel lengths of 10, 20, and 50 μm: resistances increased upon surface adsorption of PLL and Ab

The resistance shifts after the SIV binding are shown in Figure 5-13. The immnochips with 10 μm channel length exhibited a higher resolution, 10^4-fold dilution, but the saturated resistance change at high concentrations from undiluted to 10^2-fold dilution was observed. However, the ones with 20 and 50 μm channels still showed the consistent signal at high concentrations but a lower resolution, 10^3-fold dilution, meaning that the sensing area plays an important role in controlling the detection range and limit of

detection. However, it is noticeable that the sensitivity is almost the same on their detection range for all channels (30-40 Ω/decade).

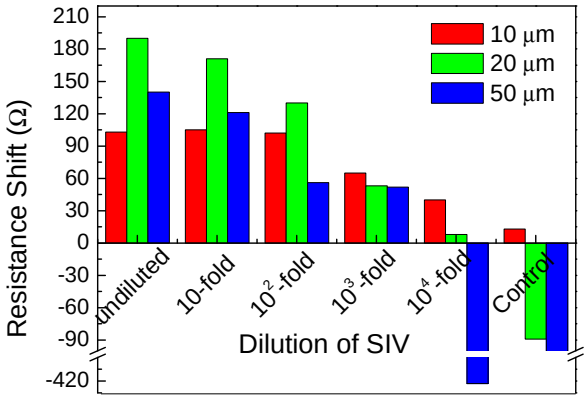

Figure 5-13 Resistance shifts upon the immunobinding of SIV on the channel lengths of 10, 20, and 50 μm: it tends to increase with the concentration of SIVs.

The normalized resistance shifts were illustrated in Figure 5-14 from a different set of immunoassay with all 10 μm channel devices. Once the resistance shifts were normalized with the resistances of bare chips, the sensitivity increased significantly to 6.4%/decade on the range of 10^1 to 10^4-fold dilutions from 3.0%/decade in case they were normalized with the resistances of devices with PLL and anti-SIV antibody assembled. However, the sensitivities upon the normalization with the resistances after PLL and antibody adsorption were almost same. Furthermore, the discernible signal was obtained on the saturated region, undiluted to 10^2-fold dilution if the resistance shift in Figure 5-13 was considered.

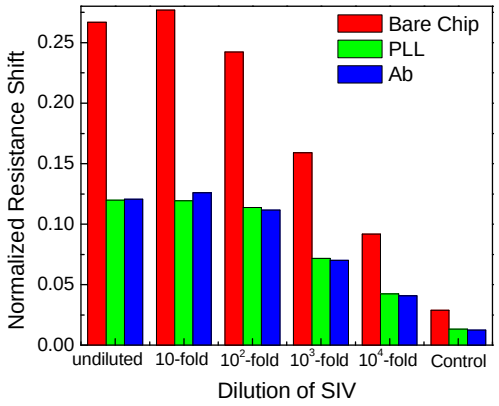

Figure 5-14 The normalized resistance shift with the resistance of bare chips, PLL coated, and anti-SIV antibody assembled chips in 10 μm channel chips: the sensitivity increased significantly upon the normalization with bare chips.

The specificity tests were conducted against TGEV and FCV using all 10 μm channel devices chips, and a typical result is shown in Figure 5-15. All resistance shifts were normalized the resistance of bare chips since it yielded a higher sensitivity. The normalized resistance changes for FCV and TGEV were within 15% and 5% in the all diluted samples except for the undiluted, while the normalized resistance shifts for SIV showed more than 20 % on the range of undiluted to 10^3-fold dilution. The reason of the high background signal for FCV might be a significant nonspecific binding of virus presumably due to 2 orders higher concentration of the undiluted virus stock as identified in Table 5-1. The signals for the control and 10^4-fold dilution of SIV revealed the background signal of 10 %. As a result of specificity test, the detection of SIV is specific down to 10^3-fold dilution, which is the number concentration of 1.77×10^2 virus/ml. As influenza viral concentration, the 50% tissue culture infectious dose ($TCID_{50}$) was used in this study, meaning that the pathogen produces pathological change in 50% of cell cultures inoculated with such amount. The range of influenza viral particles 10^3–10^5 $TCID_{50}$/ml has been found in the infected swine nasal samples [173]. Therefore, the electronic detection of SIV that had a detection limit of about 180 SIVs $TCID_{50}$/ml is suitable for rapid on-site diagnosis and/or monitoring. This results is comparative to the

results of 610 $TCID_{50}$/ml using microchip-based electrophoretic immunoassays with assay time of 6 minutes [173].

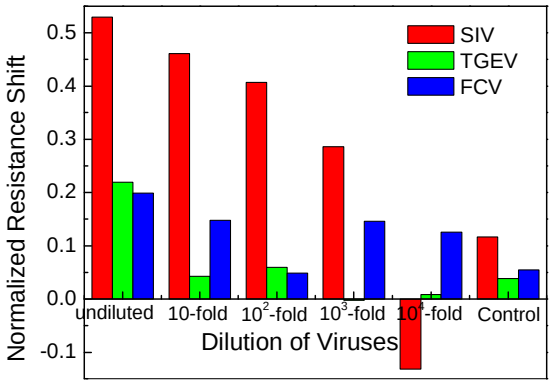

Figure 5-15 Sensor specificity tests of 10 μm channel devices against TGEV and FCV based on the normalization with the resistance of bare chips

5.2.4. Summary

The CNTs network for the electronic detection of SIVs has been demonstrated. The electrical resistance increases upon the surface adsorption of macromolecules such as PLL and antibody. Furthermore, the immunobinding of SIV on the sensor surface changes the resistance of SWCNTs film. The resistance shifts upon the virus binding are normalized with the resistance of bare devices, which extended the detection range. The detection limit of CNTs network for SIVs has been obtained as 10^3-fold dilution from multiple tests with about 10 % background signal. The specificity test also indicates 10^3-fold dilution of SIV can be detected with the specificity against FCV and TGEV, which showed 15 and 5 % of background signal on the all dilutions tested. The detection limit of 10^3-fold dilution of SIV amounts to 180 SIVs $TCID_{50}$/ml. The antibody-based assays can be utilized for the portable and clinical diagnosis of SIV H1N1.

5.3. Immunosensing performance

The performance of the developed immunosensors is evaluated in terms of detection range and detection limit as shown in Table 5-2. The INP/SNP IgG immunosensor exhibited a wider range of detection limit and 10-fold smaller detection limit than other reported CNT-based IgG sensors. Generally, CNT-based electrochemical sensors showed a pico molar detection limit, while the smallest detection limit was reported [174] due to the additional bioengineering skills to modify the molecules. The developed SWCNT swine influenza virus sensor showed the smallest detection limit, which is much smaller than other CNT-based sensors [175].

Table 5-2 Comparison of immunosensing performance with other reported results

Immunosensor type		Detection range[§§]	Detection limit[***]	Note
IgG sensors	INP/SNP ISFET	0.04-400 ng/ml	0.04 (0.26)	This work
	CNT-FET	0-10000 ng/ml	1250 (8000)	[176]
	CNT-FET	0.4-400 ng/ml	0.4 (2.6)	[82]
	CNT conductometric	1-0.1 ng/ml	0.001 (0.007)	[174]
	CNT polymer composite amperometric	0-100 ng/ml	3 (2.1)	[177]
Virus sensors	CNT SIVs	1.8×10^{2} - 1.8×10^{5}	180	This work
	Optical herpes simplex virus type 1	10^{3}-10^{7}	850	[178]
	SWCNT-FET hepatitis C virus	3×10^{8} - 1.5×10^{12}	3×10^{8}	[175]
	Microchip based electrophoretic assay	3×10^{3} – 45×10^{3}	610	[173]

[§§] Detection range and detection limit are in the unit of ng/ml and particles/ml for IgG and virus sensors, respectively

[***] pM unit in parenthesis

6. Conclusions and future directions

6.1. Conclusions

The nanomaterial devices are fabricated using the combination of top-down microfabrication and bottom-up layer-by-layer self-assembly. In order to take full advantages of extraordinary properties of nanomaterials, they should be assembled or incorporated into the existing matrix materials or structures. Layer-by-layer nano self-assembly is used to integrate nanomaterials into the microfabricated platform designed for the electrochemical sensing scheme. LbL thin film plays the role of solid-state electrochemical transducer and enzymatic and antibody-antigen complex layer acts as biorecepter.

Compared to the mechanical and electrical properties of nanomaterials, the electrochemical properties have not been studied well. In this work, pH-sensitive conductance shift of the nanomaterial devices are studied systematically and the sensing mechanisms are elucidated. The pH-sensitive conductance behavior is tunable in terms of materials and structures, and optimized to design and constructu a specific biosensor to yield a desirable sensing capability. Basically, the SWCNT device has the pH sensing mechanism that is controlled by protonation/deprotonation, which is evidenced by employing PMMA to decrease ion penetration. The proximal ion effect is characterized by using weak polyelectrolytes between SWCNT layers, leading to the fact that pH increase plays the role of negative shift in gate voltage, thereby yielding increased conductance in p-type SWCNTs. In addition, the role of SNP layer in SWCNT and INP devices is evaluated: the linear pH resonse is obtained in both SWCNT chemoresistor and ISFET in the presence of SNP without which exponential behavior is yielded due to the additional field-effect caused by abundant charge carriers on the SNP layer. However, the INP device shows higher sensitivity in basic and acidic region without and with SNPs, respectively depending on the dominant layer by protonation/deprotonation. The studied

pH-sensitive conductance behaviors are exploited to develop glucose sensors and immunosensors.

A variety of glucose sensors has been developed: conductometric SWCNT, flexible SWCNT ISFET, and INP/SNP conductormetric sensor array for the detection of physiological glucose. The exponential conductance response on the pH is utilized to obtain a linear response on the range of 0-10 mM glucose concentration. All three types of glucose sensors developed successfully detect glucose with a different sensitivity depending on the materials, structures, and testing schemes. The SWCNT thin film sensors demonstrate a higher sensitivity than the reported palanar devices and an appropriate detection range targeted for physiological blood glucose sensing. Though the response time of a few minutes is a bit longer than some devices, it is still on the reasonable range for the application of domestic glucose monitoring or rapid diagnosis. Furthermore, the activity of LbL assembled GOx is evalutated by extracting the Michaelis-Menton constants, which are less than that of free GOx enzyme, suggesting the retention of enzymatic activity.

The nanomaterial thin films have been successfully used for a facile electronic immunoassay for IgG and SIV detections. The electrochemical properties found in pH sensing are actively utilized to design and construct the immunosensors. The LbL assembled thin film transducer serves as a novel platform for elegant bioassay due to the enhanced biotic-abiotic interations between nanomaterials and biomolecules. The INP/SNP IgG sensor shows the detection range of 0.04-400 ng/ml and a resolution of 40 ng/ml. Furthermore, the SWCNT SIV sensor demonstrates the detection range of 180 to 1.8×10^5 virus particles/ml and the detection limit of 180 SIVs $TCID_{50}$/ml with specificity to non-SIVs. The developed immunosensors have a comparable sensing performance to conventional laboratory based assay techniques, but uses a facile detection scheme excluding the need of bench-top expensive equipment. The facile electronic detection of protein and pathogenic viruses via nanomaterials devices can be used as the point-of-care detection, handheld devices, and a component of lab-on-a-chip systems.

6.2. Future directions

Many possibilities exist for extensions to this research in terms of the practical application of nanomaterial biosensors, which include:

- incorporation of the reference electrode on the sensor surface for ISFET characterization scheme, which postulate the functional solid-state reference electrode
- integration of the nanomaterial thin film as a sensing component into microfluidic systems to minimize the effort to sample handling and delivery, and reduce reaction time
- construction of advanced nanostructures, e.g. suspended and/or aligned one dimensional nanomaterials, nanotube-nanoparticle complexes, CNT nanomembrane, etc for an advanced sensing technology
- realization of mutli-analyte sensors, which requires the deposition of multiple biorecepters
- expansion of sensing application to toxins, gas, other specific chemical and biological molecules
- design and implementation of micro-reacter optimized for the chain reactions
- realization of on-chip immunoassay enabling the sequential smaple handling and delivery automatically for the sample-to-answer system

Bibliography

[1] C. Hierold, A. Jungen, C. Stampfer, and T. Helbling, "Nano electromechanical sensors based on carbon nanotubes," *Sensors and Actuators A: Physical,* vol. 136, pp. 51-61, 2007.

[2] T. Durkop, S. A. Getty, E. Cobas, and M. S. Fuhrer, "Extraordinary Mobility in Semiconducting Carbon Nanotubes," *Nano Letters,* vol. 4, pp. 35-39, 2004.

[3] P. Kim, L. Shi, A. Majumdar, and P. L. McEuen, "Thermal Transport Measurements of Individual Multiwalled Nanotubes," *Physical Review Letters,* vol. 87, p. 215502, 2001.

[4] M. Bruchez, Jr., M. Moronne, P. Gin, S. Weiss, and A. P. Alivisatos, "Semiconductor Nanocrystals as Fluorescent Biological Labels," *Science,* vol. 281, pp. 2013-2016, September 25, 1998 1998.

[5] Z. L. Wang and J. Song, "Piezoelectric Nanogenerators Based on Zinc Oxide Nanowire Arrays," *Science,* vol. 312, pp. 242-246, April 14, 2006 2006.

[6] J. Wang, "Nanomaterial-based electrochemical biosensors," *The Analyst,* vol. 130, pp. 421-426, 2005.

[7] J. M. Thomas and R. Raja, "Nanopore and nanoparticle catalysts," *The Chemical Record,* vol. 1, pp. 448-466, 2001.

[8] C. Chen, S. Rosenblatt, K. I. Bolotin, W. Kalb, P. Kim, I. Kymissis, H. L. Stormer, T. F. Heinz, and J. Hone, "Performance of monolayer graphene nanomechanical resonators with electrical readout," *Nat Nano,* vol. 4, pp. 861-867, 2009.

[9] X. Michalet, F. F. Pinaud, L. A. Bentolila, J. M. Tsay, S. Doose, J. J. Li, G. Sundaresan, A. M. Wu, S. S. Gambhir, and S. Weiss, "Quantum Dots for Live Cells, in Vivo Imaging, and Diagnostics," *Science,* vol. 307, pp. 538-544, January 28, 2005 2005.

[10] D. Lee and T. Cui, "Layer-by-Layer Self-Assembled Single-Walled Carbon Nanotubes Based Ion-Sensitive Conductometric Glucose Biosensors," *IEEE Sensors Journal,* vol. 9, pp. 449-456, 2009.

[11] D. Lee and T. Cui, "pH-dependent conductance behaviors of layer-by-layer self-assembled carboxylated carbon nanotube multilayer thin-film sensors," *Journal of Vacuum Science and Technology B,* vol. 27, pp. 842-848, 2009.

[12] Y. Liu and T. Cui, "Ion-sensitive field-effect transistor based pH sensors using nano self-assembled polyelectrolyte/nanoparticle multilayer films," *Sensors and Actuators B: Chemical,* vol. 123, pp. 148-152, 2007.

[13] Y. Liu, A. G. Erdman, and T. Cui, "Acetylcholine biosensors based on layer-by-layer self-assembled polymer/nanoparticle ion-sensitive field-effect transistors," *Sensors and Actuators A: Physical,* vol. 136, pp. 540-545, 2007.

[14] X. Liu, D. Song, Q. Zhang, Y. Tian, and H. Zhang, "An optical surface plasmon resonance biosensor for determination of tetanus toxin," *Talanta,* vol. 62, pp. 773-779, 2004.

[15] J. B. Haun, T.-J. Yoon, H. Lee, and R. Weissleder, "Magnetic nanoparticle biosensors," *Wiley Interdisciplinary Reviews: Nanomedicine and Nanobiotechnology,* vol. 9999, p. n/a.

[16] I. Willner and E. Katz, "Bioelectronics: From Theory to Applications," New York: John Wiley & Sons, Ltd, 2005.

[17] J. H. Back and M. Shim, "pH-Dependent Electron-Transport Properties of Carbon Nanotubes," *The Journal of Physical Chemistry B,* vol. 110, pp. 23736-23741, 2006.

[18] J.-H. Kwon, K.-S. Lee, Y.-H. Lee, and B.-K. Ju, "Single-Wall Carbon Nanotube-Based pH Sensor Fabricated by the Spray Method," *Electrochemical and Solid-State Letters,* vol. 9, pp. H85-H87, 2006.

[19] S. Iijima, "Helical microtubules of graphitic carbon," *Nature,* vol. 354, pp. 56-58, 1991.

[20] S. Iijima and T. Ichihashi, "Single-shell carbon nanotubes of 1-nm diameter," *Nature,* vol. 363, pp. 603-605, 1993.

[21] M.-F. Yu, O. Lourie, M. J. Dyer, K. Moloni, T. F. Kelly, and R. S. Ruoff, "Strength and Breaking Mechanism of Multiwalled Carbon Nanotubes Under Tensile Load," *Science,* vol. 287, pp. 637-640, January 28, 2000 2000.

[22] E. W. Wong, P. E. Sheehan, and C. M. Lieber, "Nanobeam Mechanics: Elasticity, Strength, and Toughness of Nanorods and Nanotubes," *Science,* vol. 277, pp. 1971-1975, September 26, 1997 1997.

[23] M. M. J. Treacy, T. W. Ebbesen, and J. M. Gibson, "Exceptionally high Young's modulus observed for individual carbon nanotubes," *Nature,* vol. 381, pp. 678-680, 1996.

[24] J.-P. Salvetat, A. J. Kulik, J.-M. Bonard, G. A. D. Briggs, T. Stöckli, K. Metenier, S. Bonnamy, F. Beguin, N. A. Burnham, and L. Forró, "Elastic Modulus of Ordered and Disordered Multiwalled Carbon Nanotubes," *Advanced Materials,* vol. 11, pp. 161-165, 1999.

[25] J.-P. Salvetat, G. A. D. Briggs, J.-M. Bonard, R. R. Bacsa, A. J. Kulik, T. St?kli, N. A. Burnham, and L. z. Forr, "Elastic and Shear Moduli of Single-Walled Carbon Nanotube Ropes," *Physical Review Letters,* vol. 82, p. 944, 1999.

[26] M.-F. Yu, B. S. Files, S. Arepalli, and R. S. Ruoff, "Tensile Loading of Ropes of Single Wall Carbon Nanotubes and their Mechanical Properties," *Physical Review Letters,* vol. 84, p. 5552, 2000.

[27] A. Krishnan, E. Dujardin, T. W. Ebbesen, P. N. Yianilos, and M. M. J. Treacy, "Young's modulus of single-walled nanotubes," *Physical Review B,* vol. 58, p. 14013, 1998.

[28] P. Poncharal, Z. L. Wang, D. Ugarte, and W. A. de Heer, "Electrostatic Deflections and Electromechanical Resonances of Carbon Nanotubes," *Science,* vol. 283, pp. 1513-1516, March 5, 1999 1999.

[29] A. Javey, J. Guo, Q. Wang, M. Lundstrom, and H. Dai, "Ballistic carbon nanotube field-effect transistors," *Nature,* vol. 424, pp. 654-657, 2003.

[30] S. Berber, Y.-K. Kwon, and D. Tom?ek, "Unusually High Thermal Conductivity of Carbon Nanotubes," *Physical Review Letters,* vol. 84, p. 4613, 2000.
[31] Y. Ohno, S. Kishimoto, and T. Mizutani, "Photoluminescence of single-walled carbon nanotubes in field-effect transistors," *Nanotechnology,* p. 549, 2006.
[32] J. Sandler, M. S. P. Shaffer, T. Prasse, W. Bauhofer, K. Schulte, and A. H. Windle, "Development of a dispersion process for carbon nanotubes in an epoxy matrix and the resulting electrical properties," *Polymer,* vol. 40, pp. 5967-5971, 1999.
[33] M. J. Biercuk, M. C. Llaguno, M. Radosavljevic, J. K. Hyun, A. T. Johnson, and J. E. Fischer, "Carbon nanotube composites for thermal management," *Applied Physics Letters,* vol. 80, pp. 2767-2769, 2002.
[34] C. H. Liu, H. Huang, Y. Wu, and S. S. Fan, "Thermal conductivity improvement of silicone elastomer with carbon nanotube loading," *Applied Physics Letters,* vol. 84, pp. 4248-4250, 2004.
[35] V. Scardaci, A. G. Rozhin, F. Hennrich, W. I. Milne, and A. C. Ferrari, "Carbon nanotube-polymer composites for photonic devices," *Physica E: Low-dimensional Systems and Nanostructures,* vol. 37, pp. 115-118, 2007.
[36] J. P. Lu, "Elastic Properties of Carbon Nanotubes and Nanoropes," *Physical Review Letters,* vol. 79, pp. 1297-1300, 1997.
[37] N. Yao and V. Lordi, "Young's modulus of single-walled carbon nanotubes," *Journal of Applied Physics,* vol. 84, pp. 1939-1943, 1998.
[38] M. Cadek, J. N. Coleman, V. Barron, K. Hedicke, and W. J. Blau, "Morphological and mechanical properties of carbon-nanotube-reinforced semicrystalline and amorphous polymer composites," *Applied Physics Letters,* vol. 81, pp. 5123-5125, 2002.
[39] M. C. Paiva, B. Zhou, K. A. S. Fernando, Y. Lin, J. M. Kennedy, and Y. P. Sun, "Mechanical and morphological characterization of polymer-carbon nanocomposites from functionalized carbon nanotubes," *Carbon,* vol. 42, pp. 2849-2854, 2004.
[40] D. Qian, E. C. Dickey, R. Andrews, and T. Rantell, "Load transfer and deformation mechanisms in carbon nanotube-polystyrene composites," *Applied Physics Letters,* vol. 76, pp. 2868-2870, 2000.
[41] L. S. S. P. M. Ajayan, C. Giannaris, A. Rubio,, "Single-Walled Carbon Nanotube-Polymer Composites: Strength and Weakness," *Advanced Materials,* vol. 12, pp. 750-753, 2000.
[42] Y. Breton, G. D?armot, J. P. Salvetat, S. Delpeux, C. Sinturel, F. B?uin, and S. Bonnamy, "Mechanical properties of multiwall carbon nanotubes/epoxy composites: influence of network morphology," *Carbon,* vol. 42, pp. 1027-1030, 2004.
[43] L. S. Schadler, S. C. Giannaris, and P. M. Ajayan, "Load transfer in carbon nanotube epoxy composites," *Applied Physics Letters,* vol. 73, pp. 3842-3844, 1998.

[44] F. H. Gojny, M. H. G. Wichmann, U. K?ke, B. Fiedler, and K. Schulte, "Carbon nanotube-reinforced epoxy-composites: enhanced stiffness and fracture toughness at low nanotube content," *Composites Science and Technology,* vol. 64, pp. 2363-2371, 2004.

[45] E. T. Thostenson and T.-W. Chou, "Aligned multi-walled carbon nanotube-reinforced composites: processing and mechanical characterization," *Journal of Physics D: Applied Physics,* p. L77, 2002.

[46] R. Andrews, D. Jacques, D. Qian, and T. Rantell, "Multiwall Carbon Nanotubes: Synthesis and Application," *Accounts of Chemical Research,* vol. 35, pp. 1008-1017, 2002.

[47] C. A. Cooper, D. Ravich, D. Lips, J. Mayer, and H. D. Wagner, "Distribution and alignment of carbon nanotubes and nanofibrils in a polymer matrix," *Composites Science and Technology,* vol. 62, pp. 1105-1112, 2002.

[48] R. Haggenmueller, H. H. Gommans, A. G. Rinzler, J. E. Fischer, and K. I. Winey, "Aligned single-wall carbon nanotubes in composites by melt processing methods," *Chemical Physics Letters,* vol. 330, pp. 219-225, 2000.

[49] Z. Jin, K. P. Pramoda, G. Xu, and S. H. Goh, "Dynamic mechanical behavior of melt-processed multi-walled carbon nanotube/poly(methyl methacrylate) composites," *Chemical Physics Letters,* vol. 337, pp. 43-47, 2001.

[50] P. Potschke, A. R. Bhattacharyya, and A. Janke, "Melt mixing of polycarbonate with multiwalled carbon nanotubes: microscopic studies on the state of dispersion," *European Polymer Journal,* vol. 40, pp. 137-148, 2004.

[51] W. Tang, M. H. Santare, and S. G. Advani, "Melt processing and mechanical property characterization of multi-walled carbon nanotube/high density polyethylene (MWNT/HDPE) composite films," *Carbon,* vol. 41, pp. 2779-2785, 2003.

[52] M. Cochet, W. K. Maser, A. M. Benito, M. A. Callejas, M. T. Martinez, J.-M. Benoit, J. Schreiber, and O. Chauvet, "Synthesis of a new polyaniline/nanotube composite: "in-situ" polymerisation and charge transfer through site-selective interaction," *Chemical Communications,* pp. 1450-1451, 2001.

[53] H. J. Barraza, F. Pompeo, E. A. O'Rea, and D. E. Resasco, "SWNT-Filled Thermoplastic and Elastomeric Composites Prepared by Miniemulsion Polymerization," *Nano Letters,* vol. 2, pp. 797-802, 2002.

[54] F. Hua, T. Cui, and Y. M. Lvov, "Ultrathin Cantilevers Based on Polymer/ceramic Nanocomposite Assembled through Layer-by-Layer Adsorption," *Nano Letters,* vol. 4, pp. 823-825, 2004.

[55] A. A. Mamedov, N. A. Kotov, M. Prato, D. M. Guldi, J. P. Wicksted, and A. Hirsch, "Molecular design of strong single-wall carbon nanotube/polyelectrolyte multilayer composites," *Nat Mater,* vol. 1, pp. 190-194, 2002.

[56] W. Xue, Y. Liu, and T. Cui, "High-mobility transistors based on nanoassembled carbon nanotube semiconducting layer and SiO[sub 2] nanoparticle dielectric layer," *Applied Physics Letters,* vol. 89, p. 163512, 2006.

[57] W. Xue and T. Cui, "Characterization of layer-by-layer self-assembled carbon nanotube multilayer thin films," *Nanotechnology*, p. 145709, 2007.
[58] J. Han, "Structures and Properties of Carbon Nanoutubes," in *Carbon Nanotubes: Science and Application*, M. Meyyappan, Ed. New York: CRC Press, 2004, pp. 8-24.
[59] R. Krupke, F. Hennrich, H. v. Lohneysen, and M. M. Kappes, "Separation of Metallic from Semiconducting Single-Walled Carbon Nanotubes," *Science*, vol. 301, pp. 344-347, July 18, 2003 2003.
[60] R. Martel, T. Schmidt, H. R. Shea, T. Hertel, and P. Avouris, "Single- and multi-wall carbon nanotube field-effect transistors," *Applied Physics Letters*, vol. 73, pp. 2447-2449, 1998.
[61] T. Durkop, B. M. Kim, and M. S. Fuhrer, "Properties and applications of high-mobility semiconducting nanotubes," *Journal of Physics-Condensed Matter*, vol. 16, pp. R553-R580, May 2004.
[62] A. Javey, H. Kim, M. Brink, Q. Wang, A. Ural, J. Guo, P. McIntyre, P. McEuen, M. Lundstrom, and H. Dai, "High-k dielectrics for advanced carbon-nanotube transistors and logic gates," *Nat Mater*, vol. 1, pp. 241-246, 2002.
[63] K. Xiao, Y. Liu, P. a. Hu, G. Yu, X. Wang, and D. Zhu, "High-mobility thin-film transistors based on aligned carbon nanotubes," *Applied Physics Letters*, vol. 83, pp. 150-152, 2003.
[64] S.-H. Hur, M.-H. Yoon, A. Gaur, M. Shim, A. Facchetti, T. J. Marks, and J. A. Rogers, "Organic Nanodielectrics for Low Voltage Carbon Nanotube Thin Film Transistors and Complementary Logic Gates," *Journal of the American Chemical Society*, vol. 127, pp. 13808-13809, 2005.
[65] X.-Z. Bo, N. G. Tassi, C. Y. Lee, M. S. Strano, C. Nuckolls, and G. B. Blanchet, "Pentacene-carbon nanotubes: Semiconducting assemblies for thin-film transistor applications," *Applied Physics Letters*, vol. 87, p. 203510, 2005.
[66] E. Artukovic, M. Kaempgen, D. S. Hecht, S. Roth, and G. Gr 체 ner, "Transparent and Flexible Carbon Nanotube Transistors," *Nano Letters*, vol. 5, pp. 757-760, 2005.
[67] A. A. Mamedov, N. A. Kotov, M. Prato, D. M. Guldi, J. P. Wicksted, and A. Hirsch, "Molecular design of strong single-wall carbon nanotube/polyelectrolyte multilayer composites," *Nature Materials*, vol. 1, pp. 190-194, 2002.
[68] W. Xue and T. Cui, "A thin-film transistor based acetylcholine sensor using self-assembled carbon nanotubes and SiO2 nanoparticles," *Sensors and Actuators B: Chemical*, vol. 134, pp. 981-987, 2008.
[69] T. Zeng, R. Claus, F. Zhang, W. Du, and K. L. Cooper, "Ultrathin film actuators fabricated by layer-by-layer molecular self-assembly," *Smart Materials and Structures*, vol. 10, pp. 780-785, 2001.
[70] T. G. Shutava, D. S. Kommireddy, and Y. M. Lvov, "Layer-by-Layer Enzyme/Polyelectrolyte Films as a Functional Protective Barrier in Oxidizing

Media," *Journal of the American Chemical Society,* vol. 128, pp. 9926-9934, 2006.

[71] H. Yu, T. Cao, L. Zhou, E. Gu, D. Yu, and D. Jiang, "Layer-by-Layer assembly and humidity sensitive behavior of poly(ethyleneimine)/multiwall carbon nanotube composite films," *Sensors and Actuators B: Chemical,* vol. 119, pp. 512-515, 2006.

[72] K. J. Loh, J. Kim, J. P. Lynch, N. W. S. Kam, and N. A. Kotov, "Multifunctional layer-by-layer carbon nanotube–polyelectrolyte thin films for strain and corrosion sensing," *Smart Materials and Structures,* vol. 16, pp. 429-438, 2007.

[73] X. Yu, R. Rajamani, K. A. Stelson, and T. Cui, "Carbon nanotube-based transparent thin film acoustic actuators and sensors," *Sensors and Actuators A: Physical,* vol. 132, pp. 626-631, 2006.

[74] J. H. Rouse and P. T. Lillehei, "Electrostatic Assembly of Polymer/Single Walled Carbon Nanotube Multilayer Films," *Nano Letters,* vol. 3, pp. 59-62, 2003.

[75] Y. A. Tarakanov and J. M. Kinaret, "A Carbon Nanotube Field Effect Transistor with a Suspended Nanotube Gate," *Nano Letters,* vol. 7, pp. 2291-2294, 2007.

[76] Y. Lin, F. Lu, Y. Tu, and Z. Ren, "Glucose Biosensors Based on Carbon Nanotube Nanoelectrode Ensembles," *Nano Letters,* vol. 4, pp. 191-195, 2003.

[77] E. S. Snow, F. K. Perkins, E. J. Houser, S. C. Badescu, and T. L. Reinecke, "Chemical Detection with a Single-Walled Carbon Nanotube Capacitor," *Science,* vol. 307, pp. 1942-1945, March 25, 2005 2005.

[78] S. Sotiropoulou and N. Chaniotakis, "Carbon nanotube array-based biosensor," *Analytical and Bioanalytical Chemistry,* vol. 375, pp. 103-105, 2003.

[79] J. Kong, N. R. Franklin, C. Zhou, M. G. Chapline, S. Peng, K. Cho, and H. Dai, "Nanotube Molecular Wires as Chemical Sensors," *Science,* vol. 287, pp. 622-625, January 28, 2000 2000.

[80] A. Star, J.-C. P. Gabriel, K. Bradley, and G. Gruner, "Electronic Detection of Specific Protein Binding Using Nanotube FET Devices," *Nano Letters,* vol. 3, pp. 459-463, 2003.

[81] X. Tang, S. Bansaruntip, N. Nakayama, E. Yenilmez, Y.-l. Chang, and Q. Wang, "Carbon Nanotube DNA Sensor and Sensing Mechanism," *Nano Letters,* vol. 6, pp. 1632-1636, 2006.

[82] M. Lu, D. Lee, W. Xue, and T. Cui, "Flexible and disposable immunosensors based on layer-by-layer self-assembled carbon nanotubes and biomolecules," *Sensors and Actuators A: Physical,* vol. 150, pp. 280-285, 2009.

[83] H. Boo, R.-A. Jeong, S. Park, K. S. Kim, K. H. An, Y. H. Lee, J. H. Han, H. C. Kim, and T. D. Chung, "Electrochemical Nanoneedle Biosensor Based on Multiwall Carbon Nanotube," *Analytical Chemistry,* vol. 78, pp. 617-620, 2005.

[84] J. Wang, M. Li, Z. Shi, N. Li, and Z. Gu, "Direct Electrochemistry of Cytochrome c at a Glassy Carbon Electrode Modified with Single-Wall Carbon Nanotubes," *Analytical Chemistry,* vol. 74, pp. 1993-1997, 2002.

[85] X. Luo, A. Morrin, A. Killard, and M. Smyth, "Application of Nanoparticles in Electrochemical Sensors and Biosensors," *Electroanalysis,* vol. 18, pp. 319-326, 2006.

[86] F. Hua, J. Shi, Y. Lvov, and T. Cui, "Patterning of Layer-by-Layer Self-Assembled Multiple Types of Nanoparticle Thin Films by Lithographic Technique," *Nano Letters,* vol. 2, pp. 1219-1222, 2002.

[87] W. Xue and T. Cui, "Carbon nanotube micropatterns and cantilever arrays fabricated with layer-by-layer nano self-assembly," *Sensors and Actuators A: Physical,* vol. 136, pp. 510-517, 2007.

[88] G. Decher, J. D. Hong, and J. Schmitt, "Buildup of ultrathin multilayer films by a self-assembly process: III. Consecutively alternating adsorption of anionic and cationic polyelectrolytes on charged surfaces," *Thin Solid Films,* vol. 210-211, pp. 831-835, 1992.

[89] Y. Lvov, H. Haas, G. Decher, H. Moehwald, and A. Kalachev, "Assembly of polyelectrolyte molecular films onto plasma-treated glass," *The Journal of Physical Chemistry,* vol. 97, pp. 12835-12841, 1993.

[90] Y. Lvov, G. Decher, and H. Moehwald, "Assembly, structural characterization, and thermal behavior of layer-by-layer deposited ultrathin films of poly(vinyl sulfate) and poly(allylamine)," *Langmuir,* vol. 9, pp. 481-486, 1993.

[91] G. Decher, "Fuzzy Nanoassemblies: Toward Layered Polymeric Multicomposites," *Science,* vol. 277, pp. 1232-1237, August 29, 1997 1997.

[92] G. Decher, B. Lehr, K. Lowack, Y. Lvov, and J. Schmitt, "New nanocomposite films for biosensors: layer-by-layer adsorbed films of polyelectrolytes, proteins or DNA," *Biosensors and Bioelectronics,* vol. 9, pp. 677-684, 1994.

[93] N. A. Kotov, I. Dekany, and J. H. Fendler, "Layer-by-Layer Self-Assembly of Polyelectrolyte-Semiconductor Nanoparticle Composite Films," *The Journal of Physical Chemistry,* vol. 99, pp. 13065-13069, 1995.

[94] J. H. Rouse and P. T. Lillehei, "Electrostatic Assembly of Polymer/Single Walled Carbon Nanotube Multilayer Films," *Nano Letters,* vol. 3, pp. 59-62, 2002.

[95] F. Hua, J. Shi, Y. Lvov, and T. Cui, "Fabrication and characterization of metal-oxide-semiconductor capacitor based on layer-by-layer self-assembled thin films," *Nanotechnology,* vol. 14, p. 453, 2003.

[96] T. Cui, F. Hua, and Y. Lvov, "FET fabricated by layer-by-layer nanoassembly," *Electron Devices, IEEE Transactions on,* vol. 51, pp. 503-506, 2004.

[97] Y. Liu and T. Cui, "Glucose Biosensors Based on Layer-by-layer Nano Self-Assembled Ion-Sensitive Field-Effect Transistors," *Sensor Letters,* vol. 4, pp. 241-245, 2006.

[98] D. S. Bag, R. Dubey, N. Zhang, J. Xie, V. K. Varadan, D. Lal, and G. N. Mathur, "Chemical functionalization of carbon nanotubes with 3-methacryloxypropyltrimethoxysilane (3-MPTS)," *Smart Materials and Structures,* vol. 13, p. 1263, 2004.

[99] G. Gauglitz and T. Vo-Dinh, *Handbook of Spectroscopy* vol. 1. Weinheim: Wiley, 2002.

[100] J. Liu, A. G. Rinzler, H. Dai, J. H. Hafner, R. K. Bradley, P. J. Boul, A. Lu, T. Iverson, K. Shelimov, C. B. Huffman, F. Rodriguez-Macias, Y.-S. Shon, T. R. Lee, D. T. Colbert, and R. E. Smalley, "Fullerene Pipes," *Science,* vol. 280, pp. 1253-1256, May 22, 1998 1998.
[101] M. Kosmulski, "Pristine Points of Zero Charge of Gallium and Indium Oxides," *Journal of Colloid and Interface Science,* vol. 238, pp. 225-227, 2001.
[102] C. P. Whitby, A. M. Djerdjev, J. K. Beattie, and G. G. Warr, "In Situ Determination of the Size and Polydispersity of Concentrated Emulsions," *Langmuir,* vol. 23, pp. 1694-1700, 2006.
[103] M. Franke, T. Koplin, and U. Simon, "Metal and Metal Oxide Nanoparticles in Chemiresistors: Does the Nanoscale Matter?," *Small,* vol. 2, pp. 36-50, 2006.
[104] W. Xue and T. Cui, "Self-Assembled Carbon Nanotube Multilayer Resistors and Nanotube/Nanoparticle Thin-Film Transistors as pH Sensors," *Sensor Letters,* vol. 6, pp. 675-681, 2008.
[105] D. Lee and T. Cui, "Low-cost, transparent, and flexible single-walled carbon nanotube nanocomposite based ion-sensitive field-effect transistors for pH/glucose sensing," *Biosensors and Bioelectronics,* vol. inpress, 2010.
[106] K. Gong, Y. Yan, M. Zhang, L. Su, S. Xiong, and L. Mao, "Electrochemistry and Electroanalytical Applications of Carbon Nanotubes: A Review," *Analytical Sciences,* vol. 21, pp. 1383-1393, 2005.
[107] C.-F. Lin, G.-B. Lee, C.-H. Wang, H.-H. Lee, W.-Y. Liao, and T.-C. Chou, "Microfluidic pH-sensing chips integrated with pneumatic fluid-control devices," *Biosensors and Bioelectronics,* vol. 21, pp. 1468-1475, 2006.
[108] W. Zhao, C. Song, and P. E. Pehrsson, "Water-Soluble and Optically pH-Sensitive Single-Walled Carbon Nanotubes from Surface Modification," *Journal of the American Chemical Society,* vol. 124, pp. 12418-12419, 2002.
[109] T. W. G. Solomons, *Organic Chemistry*. New York: Wiley, 1984.
[110] S. R. Bhatia, S. F. Khattak, and S. C. Roberts, "Polyelectrolytes for cell encapsulation," *Current Opinion in Colloid & Interface Science,* vol. 10, pp. 45-51, 2005.
[111] M. Elzbieciak, M. Kolasinska, and P. Warszynski, "Characteristics of polyelectrolyte multilayers: The effect of polyion charge on thickness and wetting properties," *Colloids and Surfaces A: Physicochemical and Engineering Aspects,* vol. 321, pp. 258-261, 2008.
[112] Y.-H. Yoon, J.-W. Song, D. Kim, J. Kim, J.-K. Park, S.-K. Oh, and C.-S. Han, "Transparent Film Heater Using Single-Walled Carbon Nanotubes," *Advanced Materials,* vol. 19, pp. 4284-4287, 2007.
[113] R. Jackson and S. Graham, "Specific contact resistance at metal/carbon nanotube interfaces," *Applied Physics Letters,* vol. 94, p. 012109, 2009.
[114] Y. Zhou, L. Hu, and G. Gruner, "A method of printing carbon nanotube thin films," *Applied Physics Letters,* vol. 88, p. 123109, 2006.
[115] J. P. Icenhower and P. M. Dove, "Water Behavior at Silica Surfaces," in *Adsoprtion on Silica Suraces*, E. Papirer, Ed.: CRC press, 2000, pp. 277-295.

[116] A. L. Crumbliss, S. C. Perine, J. Stonehuerner, K. R. Tubergen, J. Zhao, R. W. Henkens, and J. P. O'Daly, "Colloidal gold as a biocompatible immobilization matrix suitable for the fabrication of enzyme electrodes by electrodeposition," *Biotechnology and Bioengineering*, vol. 40, pp. 483-490, 1992.
[117] L. M. Rossi, A. D. Quach, and Z. Rosenzweig, "Glucose oxidase–magnetite nanoparticle bioconjugate for glucose sensing," *Analytical and Bioanalytical Chemistry*, vol. 380, pp. 606-613, 2004.
[118] Z. J. Chen, X. M. Ou, F. Q. Tang, and L. Jiang, "Effect of nanometer particles on the adsorbability and enzymatic activity of glucose oxidase," *Colloids and Surfaces B: Biointerfaces*, vol. 7, pp. 173-179, 1996.
[119] M. Qhobosheane, S. Santra, P. Zhang, and W. Tan, "Biochemically functionalized silica nanoparticles," *The Analyst*, vol. 126, pp. 1274-1278, 2001.
[120] Y. Xiao, H.-X. Ju, and H.-Y. Chen, "Hydrogen peroxide sensor based on horseradish peroxidase-labeled Au colloids immobilized on gold electrode surface by cysteamine monolayer," *Analytica Chimica Acta*, vol. 391, pp. 73-82, 1999.
[121] X.-L. Luo, J.-J. Xu, W. Zhao, and H.-Y. Chen, "Glucose biosensor based on ENFET doped with SiO2 nanoparticles," *Sensors and Actuators B: Chemical*, vol. 97, pp. 249-255, 2004.
[122] X. Ren, X. Meng, and F. Tang, "Preparation of Ag-Au nanoparticle and its application to glucose biosensor," *Sensors and Actuators B: Chemical*, vol. 110, pp. 358-363, 2005.
[123] Y. Sun, F. Yan, W. Yang, and C. Sun, "Multilayered construction of glucose oxidase and silica nanoparticles on Au electrodes based on layer-by-layer covalent attachment," *Biomaterials*, vol. 27, pp. 4042-4049, 2006.
[124] T. Hoshi, N. Sagae, K. Daikuhara, K. Takahara, and J.-i. Anzai, "Multilayer membranes via layer-by-layer deposition of glucose oxidase and Au nanoparticles on a Pt electrode for glucose sensing," *Materials Science and Engineering: C*, vol. 27, pp. 890-894, 2007.
[125] K. Besteman, J.-O. Lee, F. G. M. Wiertz, H. A. Heering, and C. Dekker, "Enzyme-Coated Carbon Nanotubes as Single-Molecule Biosensors," *Nano Letters*, vol. 3, pp. 727-730, 2003.
[126] S. G. Wang, Q. Zhang, R. Wang, and S. F. Yoon, "A novel multi-walled carbon nanotube-based biosensor for glucose detection," *Biochemical and Biophysical Research Communications*, vol. 311, pp. 572-576, 2003.
[127] X. Chu, D. Duan, G. Shen, and R. Yu, "Amperometric glucose biosensor based on electrodeposition of platinum nanoparticles onto covalently immobilized carbon nanotube electrode," *Talanta*, vol. 71, pp. 2040-2047, 2007.
[128] Y.-C. Tsai, S.-C. Li, and S.-W. Liao, "Electrodeposition of polypyrrole-multiwalled carbon nanotube-glucose oxidase nanobiocomposite film for the detection of glucose," *Biosensors and Bioelectronics*, vol. 22, pp. 495-500, 2006.
[129] X. B. Yan, X. J. Chen, B. K. Tay, and K. A. Khor, "Transparent and flexible glucose biosensor via layer-by-layer assembly of multi-wall carbon nanotubes and glucose oxidase," *Electrochemistry Communications*, vol. 9, pp. 1269-1275, 2007.

[130] B.-Y. Wu, S.-H. Hou, F. Yin, Z.-X. Zhao, Y.-Y. Wang, X.-S. Wang, and Q. Chen, "Amperometric glucose biosensor based on multilayer films via layer-by-layer self-assembly of multi-wall carbon nanotubes, gold nanoparticles and glucose oxidase on the Pt electrode," *Biosensors and Bioelectronics,* vol. 22, pp. 2854-2860, 2007.
[131] Y. Zou, C. Xiang, L. Sun, and F. Xu, "Amperometric glucose biosensor prepared with biocompatible material and carbon nanotube by layer-by-layer self-assembly technique," *Electrochimica Acta,* vol. 53, pp. 4089-4095, 2008.
[132] X.-L. Luo, J.-J. Xu, W. Zhao, and H.-Y. Chen, "A novel glucose ENFET based on the special reactivity of MnO2 nanoparticles," *Biosensors and Bioelectronics,* vol. 19, pp. 1295-1300, 2004.
[133] F. Ricci, D. Moscone, C. S. Tuta, G. Palleschi, A. Amine, A. Poscia, F. Valgimigli, and D. Messeri, "Novel planar glucose biosensors for continuous monitoring use," *Biosensors and Bioelectronics,* vol. 20, pp. 1993-2000, 2005.
[134] M. Zhang, K. Gong, H. Zhang, and L. Mao, "Layer-by-layer assembled carbon nanotubes for selective determination of dopamine in the presence of ascorbic acid," *Biosensors and Bioelectronics,* vol. 20, pp. 1270-1276, 2005.
[135] Y. Lvov, K. Ariga, I. Ichinose, and T. Kunitake, "Assembly of Multicomponent Protein Films by Means of Electrostatic Layer-by-Layer Adsorption," *Journal of the American Chemical Society,* vol. 117, pp. 6117-6123, 1995.
[136] W. Liang and Y. Zhuobin, "Direct Electrochemistry of Glucose Oxidase at a Gold Electrode Modified with Single-Wall Carbon Nanotubes," *Sensors,* vol. 3, pp. 544-554, 2003.
[137] J. Grdadolnik, "Saturation effct in FTIR spectroscopy: Intensity of amide I and amide II bands in protein spectra," *Acta Chimica Slovenica,* vol. 50, pp. 777-788, 2003.
[138] T. Matsumoto, M. Furusawa, H. Fujiwara, Y. Matsumoto, and N. Ito, "A micro-planar amperometric glucose sensor unsusceptible to interference species," *Sensors and Actuators B: Chemical,* vol. 49, pp. 68-72, 1998.
[139] J. Zhu, Z. Zhu, Z. Lai, R. Wang, X. Guo, X. Wu, G. Zhang, and Z. Zhang, "Plana Amperometric Glucose Sensor Based on Glucose Oxidasee Immobilized by Chitosan Film on Prussian Blue Layer," *Sensors,* vol. 2, pp. 127-136, 2002.
[140] K. Bock, "Polymer Electronics Systems - Polytronics," *Proceedings of the IEEE,* vol. 93, pp. 1400-1406, 2005.
[141] W. Xue and T. Cui, "Electrical and electromechanical characteristics of self-assembled carbon nanotube thin films on flexible substrates," *Sensors and Actuators A: Physical,* vol. 145-146, pp. 330-335, 2008.
[142] E. D. Minot, A. M. Janssens, I. Heller, H. A. Heering, C. Dekker, and S. G. Lemay, "Carbon nanotube biosensors: The critical role of the reference electrode," *Applied Physics Letters,* vol. 91, p. 093507, 2007.
[143] M. A. d. Silva, C. G. Beddows, M. H. Gil, J. T. Guthrie, A. J. Guiomar, S. Kotov, and A. P. Piedade, "The application of radiation-induced processed copolymers to

biocatalysis immobilisation," *Radiation Physics and Chemistry*, vol. 35, pp. 98-101, 1990.

[144] X. Chen, J. Chen, C. Deng, C. Xiao, Y. Yang, Z. Nie, and S. Yao, "Amperometric glucose biosensor based on boron-doped carbon nanotubes modified electrode," *Talanta*, vol. 76, pp. 763-767, 2008.

[145] Y. Wang, X. Wang, B. Wu, Z. Zhao, F. Yin, S. Li, X. Qin, and Q. Chen, "Dispersion of single-walled carbon nanotubes in poly(diallyldimethylammonium chloride) for preparation of a glucose biosensor," *Sensors and Actuators B: Chemical*, vol. 130, pp. 809-815, 2008.

[146] F. Caruso, H. Lichtenfeld, M. Giersig, and H. Mohwald, "Electrostatic Self-Assembly of Silica Nanoparticleâˆ'Polyelectrolyte Multilayers on Polystyrene Latex Particles," *Journal of the American Chemical Society*, vol. 120, pp. 8523-8524, 1998.

[147] B. Raguse, E. Chow, C. S. Barton, and L. Wieczorek, "Gold Nanoparticle Chemiresistor Sensors:??Direct Sensing of Organics in Aqueous Electrolyte Solution," *Analytical Chemistry*, vol. 79, pp. 7333-7339, 2007.

[148] E. S. Forzani, H. Zhang, L. A. Nagahara, I. Amlani, R. Tsui, and N. Tao, "A Conducting Polymer Nanojunction Sensor for Glucose Detection," *Nano Letters*, vol. 4, pp. 1785-1788, 2004.

[149] R. D. Vaughan, C. K. O'Sullivan, and G. G. Guilbault, "Development of a quartz crystal microbalance (QCM) immunosensor for the detection of Listeria monocytogenes," *Enzyme and Microbial Technology*, vol. 29, pp. 635-638, 2001.

[150] V. B. Pizziconi and D. L. Page, "A cell-based immunobiosensor with engineered molecular recognition--Part I: design feasibility," *Biosensors and Bioelectronics*, vol. 12, pp. 287-299, 1997.

[151] P. Sklaal, "Advances in electrochemical immunosensors," *Electroanalysis*, vol. 9, pp. 737-745, 1997.

[152] O. A. Sadik and J. M. Van Emon, "Applications of electrochemical immunosensors to environmental monitoring," *Biosensors and Bioelectronics*, vol. 11, pp. i-x, 1996.

[153] Y. V. Plekhanova, A. N. Reshetilov, E. V. Yazynina, A. V. Zherdev, and B. B. Dzantiev, "A new assay format for electrochemical immunosensors: polyelectrolyte-based separation on membrane carriers combined with detection of peroxidase activity by pH-sensitive field-effect transistor," *Biosensors and Bioelectronics*, vol. 19, pp. 109-114, 2003.

[154] R. Marks, A. Margalit, A. Bychenko, E. Bassis, N. Porat, and R. Dagan, "Development of a chemiluminescent optical fiber immunosensor to detect Streptococcus pneumoniae antipolysaccharide antibodies," *Applied Biochemistry and Biotechnology*, vol. 89, pp. 117-126, 2000.

[155] S. Kubitschko, J. Spinke, T. Br?kner, S. Pohl, and N. Oranth, "Sensitivity Enhancement of Optical Immunosensors with Nanoparticles," *Analytical Biochemistry*, vol. 253, pp. 112-122, 1997.

[156] J. Duendorfer and R. E. Kunz, "Compact Integrated Optical Immunosensor using Replicated Chirped Grating Coupler Sensor Chips," *Appl. Opt.,* vol. 37, pp. 1890-1894, 1998.
[157] J. Okuno, K. Maehashi, K. Kerman, Y. Takamura, K. Matsumoto, and E. Tamiya, "Label-free immunosensor for prostate-specific antigen based on single-walled carbon nanotube array-modified microelectrodes," *Biosensors and Bioelectronics,* vol. 22, pp. 2377-2381, 2007.
[158] R. Malhotra, V. Patel, J. P. Vaque, J. S. Gutkind, and J. F. Rusling, "Ultrasensitive Electrochemical Immunosensor for Oral Cancer Biomarker IL-6 Using Carbon Nanotube Forest Electrodes and Multilabel Amplification," *Analytical Chemistry*.
[159] T. A. Sergeyeva, N. V. Lavrik, S. A. Piletsky, A. E. Rachkov, and A. V. El'skaya, "Polyaniline label-based conductometric sensor for IgG detection," *Sensors and Actuators B: Chemical,* vol. 34, pp. 283-288, 1996.
[160] G. Liu, Y.-Y. Lin, J. Wang, H. Wu, C. M. Wai, and Y. Lin, "Disposable Electrochemical Immunosensor Diagnosis Device Based on Nanoparticle Probe and Immunochromatographic Strip," *Analytical Chemistry,* vol. 79, pp. 7644-7653, 2007.
[161] J. Owino, O. Arotiba, N. Hendricks, E. Songa, N. Jahed, T. Waryo, R. Ngece, P. Baker, and E. Iwuoha, "Electrochemical Immunosensor Based on Polythionine/Gold Nanoparticles for the Determination of Aflatoxin B1," *Sensors,* vol. 8, pp. 8262-8274, 2008.
[162] G. Liu, J. Wang, R. Barry, C. Petersen, C. Timchalk, P. Gassman, and Y. Lin, "Nanoparticle-Based Electrochemical Immunosensor for the Detection of Phosphorylated Acetylcholinesterase: An Exposure Biomarker of Organophosphate Pesticides and Nerve Agents," *Chemistry - A European Journal,* vol. 14, pp. 9951-9959, 2008.
[163] V. K. Akimenko, S. M. Khomutov, A. Y. Obraztsova, S. A. Vishnivetskii, N. A. Chuvilskaya, K. S. Laurinavichus, and A. N. Reshetilov, "A rapid method for detection of Clostridium thermocellum by field-effect transistor-based immunodetection," *Journal of Microbiological Methods,* vol. 24, pp. 203-209, 1996.
[164] D. Janssen, R. De Palma, S. Verlaak, P. Heremans, and W. Dehaen, "Static solvent contact angle measurements, surface free energy and wettability determination of various self-assembled monolayers on silicon dioxide," *Thin Solid Films,* vol. 515, pp. 1433-1438, 2006.
[165] P. Kim, D. H. Kim, B. Kim, S. K. Choi, S. H. Lee, A. Khademhosseini, R. Langer, and K. Y. Suh, "Fabrication of nanostructures of polyethylene glycol for applications to protein adsorption and cell adhesion," *Nanotechnology,* vol. 16, p. 2420, 2005.
[166] H. Stadler, M. Mondon, and C. Ziegler, "Protein adsorption on surfaces: dynamic contact-angle (DCA) and quartz-crystal microbalance (QCM) measurements," *Analytical and Bioanalytical Chemistry,* vol. 375, pp. 53-61, 2003.

[167] S. I. Khan, S. M. F. Akbar, S. T. Hossain, and M. A. Mahtab, "Swine Influenza (H1N1) Pandemic: Developing Countries' Perspective," *Rural Remote Health,* vol. 9, p. 1262, 2009.
[168] Y. K. Choi, S. M. Goyal, S. W. Kang, M. W. Farnham, and H. S. Joo, "Detection and subtyping of swine influenza H1N1, H1N2 and H3N2 viruses in clinical samples using two multiplex RT-PCR assays," *Journal of Virological Methods,* vol. 102, pp. 53-59, 2002.
[169] B. Lee, R. Bey, M. Baarsch, and R. Simonson, "ELISA method for detection of influenza A infection in swine," *J Vet Diagn Invest,* vol. 5, pp. 510-515, October 1, 1993 1993.
[170] P. Lekcharoensuk, K. M. Lager, R. Vemulapalli, M. Woodruff, A. L. Vincent, and J. A. Richt, "Novel Swine Influenza Virus Subtype H3N1, United States," in *Emerging Infectious Diseases*. vol. 12: Centers for Disease Control & Prevention (CDC), 2006, pp. 787-794.
[171] R. d. l. Rica, E. Mendoza, L. M. Lechuga, and H. Matsui, "Label-Free Pathogen Detection with Sensor Chips Assembled from Peptide Nanotubes13," *Angewandte Chemie International Edition,* vol. 47, pp. 9752-9755, 2008.
[172] L. J. Reed and H. Muench, "A Simple method of estimating fifty percent endpoints," *Am. J. Epidemiol.*, vol. 27, pp. 493-497, May 1, 1938 1938.
[173] D. S. Reichmuth, S. K. Wang, L. M. Barrett, D. J. Throckmorton, W. Einfeld, and A. K. Singh, "Rapid microchip-based electrophoretic immunoassays for the detection of swine influenza virus," *Lab on a Chip,* vol. 8, pp. 1319-1324, 2008.
[174] J. P. Kim, B. Y. Lee, S. Hong, and S. J. Sim, "Ultrasensitive carbon nanotube-based biosensors using antibody-binding fragments," *Analytical Biochemistry,* vol. 381, pp. 193-198, 2008.
[175] T. Dastagir, E. S. Forzani, R. Zhang, I. Amlani, L. A. Nagahara, R. Tsui, and N. Tao, "Electrical detection of hepatitis C virus RNA on single wall carbon nanotube-field effect transistors," *The Analyst,* vol. 132, pp. 738-740, 2007.
[176] C. C. Cid, J. Riu, A. Maroto, and F. X. Rius, "Carbon nanotube field effect transistors for the fast and selective detection of human immunoglobulin G," *The Analyst,* vol. 133, pp. 1005-1008, 2008.
[177] C. Fermandez-Sanchez, E. Pellicer, J. Orozco, C. Jimenez-Jorquera, L. M. Lechuga, and E. Mendoza, "Plasma-activated multi-walled carbon nanotube-polystyrene composite substrates for biosensing," *Nanotechnology,* vol. 20, p. 335501, 2009.
[178] A. Ymeti, J. Greve, P. V. Lambeck, T. Wink, H. van, Beumer, R. R. Wijn, R. G. Heideman, V. Subramaniam, and J. S. Kanger, "Fast, Ultrasensitive Virus Detection Using a Young Interferometer Sensor," *Nano Letters,* vol. 7, pp. 394-397, 2006.